

Defects and Distortions in Hybrid Halide Perovskites

Lucy Dorothy Whalley

Department of Materials

Imperial College London

A thesis submitted for the degree of

Doctor of Philosophy

August 2019

Abstract

Hybrid halide perovskites are being developed for use as an absorber material in solar cells, alongside other optoelectronic applications such as the light-emitting diode or laser. Research interest in this material family has grown quickly over the decade, as photovoltaic efficiencies have increased from 10.9% in 2012 to the current record of 24.2%. In addition, the synthesis procedure is a low-temperature solution-deposition method which, when commercialised, may allow for a reduction in solar module production prices.

Materials theory and simulation has struggled to keep up with this rapid progress as many of the physical processes which determine solar cell performance are related to defects (e.g. carrier capture and recombination) and temperature (e.g. degradation and ion migration), which are challenging to model from first-principles. A typical Density Functional Theory (DFT) calculation for a crystalline material assumes that the material is perfectly periodic, with no point or extended defects. In addition, DFT is used to model ground-state properties; to account for temperature effects (e.g. atomic vibrations) it is necessary to combine DFT with other methods (e.g. lattice dynamics). The aim of this PhD project is to move away from the idealised picture of a perfect material at absolute zero and towards a more realistic picture, where the defects and distortions of hybrid halide perovskites are considered.

Contents

Copyright	6
Statement of Authorship	7
Publications	8
Acknowledgements	9
List of Figures	11
List of Tables	13
Abbreviations	14
Symbols	15
1 Introduction	17
1.1 Motivation	17
1.1.1 Energy use and global warming	17
1.1.2 The sun as an energy source	18
1.1.3 Beyond silicon: the need for new photovoltaic materials	19
1.2 Key concepts in photovoltaics	20
1.2.1 Operating principles	21
1.2.2 Carrier recombination	25
1.2.3 Design principles for absorber materials	26
1.3 Summary	30
1.4 Format of the thesis	30

2 Theory and simulation of hybrid halide perovskites	31
2.1 Introduction	31
2.2 Crystal structures and lattice dynamics	32
2.2.1 Phase diversity	32
2.2.2 Local and average crystal environment	33
2.2.3 Thermodynamic and kinetic stability	35
2.2.4 Anharmonic lattice vibrations and thermal conductivity	35
2.3 Electronic structure	37
2.3.1 Many-body and relativistic effects	37
2.3.2 Electron-phonon coupling	39
2.3.3 Charge carrier transport	40
2.4 Photophysics and solar cells	40
2.4.1 Ion migration	41
2.4.2 Electron-hole recombination	42
2.4.3 Defect levels in the band-gap	44
2.4.4 Beyond the bulk: surfaces, grain boundaries and interfaces	44
2.5 Summary	45
3 Theory and methodology	48
3.1 Introduction	48
3.2 Density Functional Theory	48
3.2.1 Basic concepts	49
3.2.2 DFT in practice	52
3.3 Defects in semiconductors	62
3.3.1 Classification of crystal defects	62
3.3.2 Energetics of defect formation	63
3.3.3 Supercell method	64
3.4 Lattice dynamics	66
3.4.1 Harmonic approximation	67
3.4.2 Anharmonicity	69
3.4.3 Finite displacement method	69
3.5 Summary	70

<i>Contents</i>	5
Closing Remarks	71
Appendices	
A DFT bandstructures	73
B Effective mass and k-point spacing	78
C effmass: An effective mass package	79
C.1 Summary	79
C.2 Related packages	80
C.3 Unique features of effmass	80
C.4 Acknowledgements	80
D Diffusion equation for a hot sphere	82
E Copyright permissions	84

Copyright

The copyright of this thesis rests with the author. Unless otherwise indicated, its contents are licensed under a Creative Commons Attribution-Non Commercial 4.0 International Licence (CC BY-NC). Under this licence, you may copy and redistribute the material in any medium or format. You may also create and distribute modified versions of the work. This is on the condition that: you credit the author and do not use it, or any derivative works, for a commercial purpose. When reusing or sharing this work, ensure you make the licence terms clear to others by naming the licence and linking to the licence text. Where a work has been adapted, you should indicate that the work has been changed and describe those changes. Please seek permission from the copyright holder for uses of this work that are not included in this licence or permitted under UK Copyright Law.

Statement of Authorship

I declare that this thesis and the work presented in it are my own and has been generated by me as the result of my own original research. Where work is not my own references are given. In addition, I list below the instances where work has been done in conjunction with others.

Chapter 2: Theory and simulation of hybrid halide perovskites

The central idea of this chapter (to review the theory and simulation of hybrid halide perovskites) was provided by Aron Walsh. The contents of the review were a product of discussions between myself, Aron Walsh and Jarvist Frost. Aron Walsh prepared figures 2.1, 2.2–2.4, and Young-Kwang Jung prepared figure 2.3.

Chapter 4: Electronic band non-parabolicity

The central idea of this chapter (to investigate, across a range of photovoltaic materials, the sensitivity of DFT calculated effective mass to fitting parameters) was provided by Aron Walsh and Benjamin Morgan. Jarvist Frost suggested weighting the fit to a Fermi-Dirac distribution.

Chapter 5: Electron-phonon and phonon-phonon coupling

Jarvist Frost suggested using a classical heat diffusion model for hot carrier cooling and calculated the temperature dependant bandgap shifts. Jonathan M. Skelton provided scripts to implement the frozen phonon method. Aron Walsh prepared figure 5.1.

Chapter 6: H-centre defects

The central idea of this chapter (to investigate hole capture at an iodine interstitial in $\text{CH}_3\text{NH}_3\text{PbI}_3$) was provided by Aron Walsh. Aron Walsh prepared figure X.

Publications

The following publications have arisen from this PhD work. Where copyright is retained by the publisher, text and figures are reprinted with permission, as detailed in Appendix E.

Chapter 2: Theory and simulation of hybrid halide perovskites

Text and figures 1–4 reprinted with permission from Whalley, L. D., Frost, J. M., Jung, Y. -K. and Walsh, A. (2017). Perspective: Theory and simulation of hybrid halide perovskites. *The Journal of Chemical Physics*, 146(22), p.220901. © 2017 CC-BY

Chapter 4: Results I: Electronic band non-parabolicity

Text and figures 1–11 reprinted with permission from Whalley, L. D., Frost, J., Morgan, B. and Walsh, A. (2019). Impact of nonparabolic electronic band structure on the optical and transport properties of photovoltaic materials. *Physical Review B*, 99(8). © 2019 American Physical Society

Chapter 5: Results II: Electron-phonon and phonon-phonon coupling

Excerpts and figures 2–4 reprinted with permission from Whalley, L. D., Skelton, J. M., Frost, J. M. and Walsh, A. (2016). Phonon anharmonicity, lifetimes, and thermal transport in $\text{CH}_3\text{NH}_3\text{PbI}_3$ from many-body perturbation theory. *Physical Review B*, 94(22). © 2016 American Physical Society

Excerpts and figures 1,5–6 reprinted with permission from Frost, J. M., Whalley, L. D and Walsh, A. (2017). Slow Cooling of Hot Polarons in Halide Perovskite Solar Cells. *ACS Energy Letters*, 2(12), pp.2647-2652. © 2017 CC-BY

Chapter 6: Results III: H-centre defects

Excerpts and figures reprinted with permission from Whalley, L. D., Crespo-Otero, R. and Walsh, A. (2017). H-Center and V-Center Defects in Hybrid Halide Perovskites. *ACS Energy Letters*, 2(12), pp.2713-2714. © 2017 American Chemical Society

Appendix 3: effmass: An effective mass package

Text reprinted with permission from Whalley, L. D. (2018). effmass: An effective mass package. *Journal of Open Source Software*, 3(28), p.797. © 2018 CC-BY

Acknowledgements

Leaving an enjoyable job and returning to study is not an easy decision, but starting a PhD in the Walsh group was one of the best I have made. A huge thanks must be given to Aron Walsh for creating and maintaining a supportive, friendly and productive working environment. I have gained a *huge amount* from working with Aron and other members of the group. Although I have learnt something from every member I will not list everyone here, but a special thanks must go to Jarvist Frost who led book group and helped clarify my sometimes muddled understanding of solid state physics. Another special thanks to the women I have worked with; we are still too few and far between in the physical sciences, but what we lack in quantity we make up for in quality! Thanks also to Benjamin Morgan, my second supervisor, who guided me through my first research project and has provided extensive feedback on my scientific writing.

During the third year of my PhD I became involved with the Research Software Engineering community at Imperial. I would like to thank Katerina Michalickova for organising the Software Carpentry workshops - it is no easy job co-ordinating a rabble of volunteers from across Imperial, but teaching software carpentry has greatly increased my confidence around programming. Thanks also to fellow members of the Imperial RSE community committee, especially Jeremy Cohen who is mentoring me as part of my Software Sustainability Institute fellowship.

The vast majority of the computational analysis in this thesis depends to some degree on the open-source community. Thousands of person-hours, often I suspect squeezed in at weekends or evenings, has produced well-tested, well-documented, easily accessible code. Without the magical Python ‘import’ statement and the generosity of strangers I would probably still be writing an integration routine for my first year project. Thanks also to the admin and technical staff who keep the supercomputers Archer, Thomas and Piz-Daint running. I rarely think about the infrastructure behind my calculations, and this is exactly why I need to say thanks.

Funding for my PhD came from the EPSRC, via the Centre for Doctoral Training in New and Sustainable Photovoltaics. It seems that running a CDT requires staff to go above and beyond - thanks to Ken Durose, Alison Walker, Rob Treharne and Asim Mumtaz for doing just this.

The biggest thanks must go to my family and friends. I met Richard (in a *romantic* way) towards the start of my PhD. It is now four years on, and we have bought a house, got married and created a very small human being (currently still residing in my tummy). I wouldn’t have expected that all this was compatible with doing a PhD, but being with Richard has made it seem like the most natural thing in the world. He has been with me, and supported me, throughout. It is through Richard’s parents, Andrew and Elspeth, that I was introduced to John and Karen. By gifting me use of a bedroom twice a week for three years, John and Karen

have enabled me to live in Birmingham and work in London. I don't think it would have been possible for me and Richard to 'settle down' otherwise and for this I am very grateful.

I'm lucky to have close, reliable and hilarious friends who are always suggesting things to take my mind off work. Thanks especially to Hetta and Blanche for Lipsync and our other little "projects" and Caz for her loyalty and warmth. Ruby, my sister, is equally hilarious and understands me (and sees through me!) in a way that no-one else can. The final thanks is reserved for my parents John and Alison, whose love and support instilled in me a self-confidence that I think is so important when doing science. All of my achievements are theirs, as none of this would have been possible without their investment into me.

List of Figures

1.1	Historic and predicted costs of solar energy generation	19
1.2	Typical solar cell architectures	22
1.3	Solar cell current-voltage curve	23
1.4	AM1.5 spectral intensity and Shockley-Queisser efficiency	24
1.5	Electron-hole recombination pathways	25
2.1	$\text{CH}_3\text{NH}_3\text{PbBr}_3$ powder neutron diffraction pattern and crystallographic unit cells	32
2.2	$\text{CH}_3\text{NH}_3\text{PbBr}_3$ phonon dispersion and double-well potential energy surface . . .	33
2.3	Electronic band structures of CsPbBr_3 and $\text{CH}_3\text{NH}_3\text{PbBr}_3$	36
2.4	Simple phase segregation model	41
3.1	Interacting and non-interacting particle systems	50
3.2	Dimensionality of variational objects	52
3.3	Jacob's ladder of exchange-correlation functionals	53
3.4	Translational symmetry and supercell construction	55
3.5	Bonding and anti-bonding states in an infinite 1D crystal	56
3.6	Nested iterative method for geometry optimisation	60
3.7	k -point convergence of CsSnI_3	61
3.8	Classification of crystal point-defects	63
3.9	Formation energies of the Te vacancy in CdTe	65
3.10	Crystal potential energy expanded with respect to atomic displacement	68
3.11	3-phonon processes and anharmonic potential energy surfaces	70
A.1	MAPI bandstructure, HSE06, no-SoC	74
A.2	MAPI bandstructure, HSE06, SoC	74
A.3	CZTS bandstructure, HSE06, no-SoC	75

A.4 CZTS bandstructure, HSE06, SoC	75
A.5 GaAs bandstructure, HSE06, no-SoC	76
A.6 GaAs bandstructure, HSE06, SoC	76
A.7 CdTe bandstructure, HSE06, no-SoC	77
A.8 CdTe bandstructure, HSE06, SoC	77

List of Tables

2.1	Donor defect levels in $\text{CH}_3\text{NH}_3\text{PbBr}_3$, Si and CdTe	44
2.2	Common issues that arise in the simulation of hybrid perovskites	46
B.1	Effective mass and k -point spacing	78

Abbreviations

AM	Air Mass
CBM	Conduction Band Minimum
CZTS	Copper zinc tin sulfide
DFT	Density Functional Theory
GGA	Generalised gradient approximation
HF	Hartree-Fock
HSE06	Heyd-Scuseria-Ernzerhof screened hybrid DFT functional
LDA	Local density approximation
PBE, PBESol	Perdew-Burke-Ernzerhof DFT functional; PBESol is recommended for solids
MAPI	Methylammonium lead iodide
PV	Photovoltaic
SRH	Shockley-Reed-Hall
SoC	Spin-orbit coupling
VBM	Valence Band Maximum

Symbols

∇	Vector differential operator
ϵ	Energy of a state
ϵ_0	Static dielectric constant
ϵ_{inf}	High frequency (optical) dielectric constant
η	Photovoltaic efficiency
μ	Chemical potential
ν	Phonon frequency
π	Pi constant ~ 3.14
ρ	Electron density
σ	Carrier capture cross section
τ	Carrier lifetime
ϕ	Kohn-Sham orbital
Ψ	Many-body Wavefunction
e	Exponential constant ~ 2.72
h	Planck constant $\sim 6.63 \times 10^{-34} \text{ Js}$
\hbar	Reduced Planck constant $\frac{h}{2\pi}$
k	Wavevector associated with periodic electronic structure
k_B	Boltzmann constant $\sim 1.38 \times 10^{-23} \text{ JK}^{-1}$
n	Carrier concentration
\mathbf{r}	position vector
t	Time
v	Group velocity
E	Total energy

E_0 Ground state energy

E_F Fermi energy

FF Fill factor

I Current

I_{SC} Short circuit current

N_t Trap density

P Power

R Resistance

T Temperature

V Voltage

V_{OC} Open circuit voltage

For generations, we have assumed that the efforts of mankind would leave the fundamental equilibrium of the world's systems and atmosphere stable. But it is possible that with all these enormous changes (population, agricultural, use of fossil fuels) concentrated into such a short period of time, we have unwittingly begun a massive experiment with the system of this planet itself.

— Margaret Thatcher

1

Introduction

1.1 Motivation

In this section I justify photovoltaic materials research. First, the challenge we face as a human race – global warming – is introduced, followed by why we should take advantage of the sun as an energy source. The section ends with a discussion about the three generation of solar cell materials, and the inherent limitations of silicon solar cells.

1.1.1 Energy use and global warming

Anthropogenic climate change is one of the greatest challenges we face as a human race and, as we have twelve years to limit climate change catastrophe, we are running against the clock. This viewpoint is not party political or the political hyperbole of the green left, as I have tried to allude to with the opening quote – this is the current scientific understanding as established by the International Panel on Climate Change.¹

The story begins in the 18th century when the industrial revolution enabled unprecedented population growth, from 0.8 billion in 1750 to 7.5 billion in 2017.² Industrial expansion combined with a growing population led to an exponential growth in the amount of coal and oil being burnt; between the years 1769 and 2006 there was an 800-fold increase in the world annual coal production.³ Atmospheric CO₂ concentrations increased as a result, leading to an increase in global temperatures, rising sea levels, and ocean acidification. The years 2014–2018 were the five hottest years on record⁴ and there has been a recent increase in extreme weather (heat waves, drought and floods) across the globe.⁵ Studies have shown that the probability of heat waves,⁶ wildfires⁷ and flooding^{8,9} have increased as a result climate change.

The threat of climate change seems not to have had a proportionate response from governments or many individuals. One reason for this is that changes in weather patterns are significant only

when looked at over long time periods, and so it is difficult to communicate the risk carried by climate change. Another is that this is an inherently international problem, and that we do not have the political mechanisms in place to coordinate a global response. Despite the dramatic consequences of inaction, there seems to be little public appetite for changes which require a reduction in energy use. Instead there is a push towards technological solutions which may be able to reduce the negative effects of climate change without impacting upon our perceived quality of life.

1.1.2 The sun as an energy source

One way to reduce the rate of climate change is to generate energy through processes that do not release net positive amounts of CO₂ into the atmosphere, and harnessing the vast amount of energy that is released from the sun is one way of doing this. This idea has been around for more than sixty years; in 1954 Bell Labs demonstrated that it was possible to convert sunlight into electricity by powering a small toy Ferris wheel and radio transmitter with a silicon solar cell. Reporting this event, The New York Times wrote:

“[the solar cell] may mark the beginning of a new era, leading eventually to the realization of one of mankind’s most cherished dreams—the harnessing of the almost limitless energy of the sun for the uses of civilization.”

A solar flux density of 1361 Wm⁻² reaches the earth’s atmosphere each second, which is almost 10⁴ times larger than any other external energy source.¹⁰ A quick back-of-the-envelope calculation shows that if we assume a sunlight to electricity conversion efficiency of 40% (achievable using concentrated solar power) and zero transmission loss, we could meet the world’s electricity demands (22PWh in 2015¹¹) by covering an area equivalent to Northumberland county (5000km²) with photovoltaic solar panels. However to harness this power we must be able to convert sunlight into electrical energy at a competitive price and at scale. Photovoltaic efficiency is key to price reduction as there are significant costs that scale with area,^{12,13} and a higher efficiency module can deliver the same energy for a smaller area.

The first photovoltaic devices could transform sunlight into electrical energy with an efficiency of around 6%. The computing boom of the 1980s encouraged large investment into silicon research and silicon cells with 20% efficiency were reported in 1986.¹⁴ Since 1980 costs have decreased at an average rate of 10% per year¹⁵ (Fig. 1.1) and the global market is growing, from a capacity of 1.9 GW in 2005 to 102 GW in 2016.¹⁶

In the UK the growth in renewable energy has led to a decreasing dependence on fossil fuels. The UK had its first day without coal in 2017¹⁷ and ran for three days without coal in 2018.¹⁸ There appears to be a growing political will to take advantage of renewable energy; the first UK National Infrastructure Assessment recommends halting the development of nuclear power stations and diverting investment into solar and wind energy generation instead.¹⁹ This switch away from nuclear energy is projected to be at no cost to the consumer.

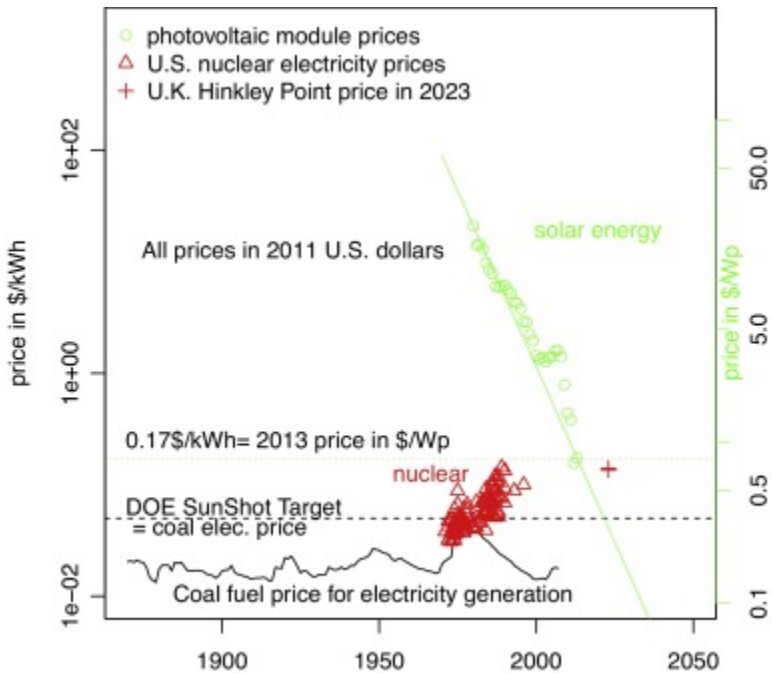


Figure 1.1: Historic and predicted costs of energy generation. The cost of solar energy (green) has been decreasing exponentially (at an average rate of 10% per year) and is now comparable with the cost of energy generated from nuclear power (red). The dashed line corresponds to a solar energy cost target from the US Department of Energy of 0.05 \$/kWh. Reproduced with permission from the work of Farmer et al.¹⁵

It is widely predicted that solar power will continue to grow – to what extent depends on the source: a recent study from Imperial College London estimates that solar power could supply 23% of global energy demand in 2040.²⁰ ExxonMobil, a company heavily invested in fossil fuels, predicts that all renewables combined will supply 20% of global power generation in 2040.²¹ Note that previous models have consistently underestimated the scale of photovoltaic deployment.²²

1.1.3 Beyond silicon: the need for new photovoltaic materials

Photovoltaic devices are commonly split into three generations. In this section I introduce each generation and discuss what is driving the development of new PV materials in a competitive market that is dominated by silicon.

First generation

The first generation devices are based upon mono- and poly-crystalline silicon wafers. They dominate the PV market; in 2016 90% of total PV module production used this technology.¹⁶ They are high efficiency (>20%), reliable (25 year lifetimes) and low cost (<0.5 \$/W). There has been a steady decrease in cost due to i) device engineering improvements (eg: textured surfaces); ii) the economies of scale as silicon industrial processes are driven by a demand for computer chips; and iii) improved industrial practices which allow thinner and thinner wafers to be fabricated with less waste. However there are technological and physical limits to how much

the cost of a crystalline silicon wafer can be reduced. First, the manufacturing process for silicon wafers is energy intensive and requires high temperatures. Second, silicon is an indirect bandgap material and as a result does not absorb sunlight efficiently; wafers have to be a minimum thickness ($\sim 60\mu\text{m}$) to compensate for this. It is difficult to reach this limit without snapping the material during fabrication as silicon is a hard and brittle material.

Second generation

Second generation devices are fabricated from the direct bandgap materials gallium arsenide (GaAs), cadmium telluride (CdTe), cadmium indium gallium diselenide (CIGS) and amorphous silicon (a-Si). These materials have higher absorption coefficients, so they can be built into lighter thin-film ($\sim 10\mu\text{m}$) architectures. A thin-film is not mechanically stable, it needs a substrate, but this opens up possibility of it being a flexible film.

CdTe was the first thin film to be commercialised and development has been led by the company First Solar, who have installed a total capacity of 17 GW. Lifecycle assessments indicate that the CdTe energy payback time (the time required to generate as much energy as is consumed during production and lifetime operation of the system) is shorter than that of Si.²³ However lower efficiencies are stifling the growth of this technology and there are also concerns about the elemental toxicity and scarcity. CIGS and a-Si each have a smaller market share than CdTe. High efficiency ($\sim 40\%$) GaAs devices have been developed for the high-value, low-volume space market.

Third generation

Third generation devices are emerging technologies which are not yet in the market. This includes organic and dye-sensitised materials, hybrid halide perovskites, and copper zinc tin sulfide (CZTS). These are abundant materials which can be fabricated through low-cost solution-deposition methods. Only the hybrid-halide perovskites have efficiencies high enough for commercialisation (currently 24.2%).

For the third generation materials commercial success may come from opening up new markets rather than trying to compete directly with well established silicon technologies. For example, organic and hybrid perovskite technologies have tunable bandgaps and are being developed for semi-transparent building integrated photovoltaics. There has also been recent research interest and commercial investment into silicon-perovskite single junction tandem cells.

1.2 Key concepts in photovoltaics

This section outlines the physical principles underlying solar cell operation, with a focus on carrier recombination. After introducing the key concepts and vocabulary, the design rules or “wish list” for a successful PV material are outlined.

1.2.1 Operating principles

A solar cell converts light into electricity through the following (simplified) process: i) a photon enters the device; ii) the photon is absorbed and creates an electron-hole pair in the absorber layer; iii) the electron and hole disassociate; iv) the electron and hole travel through the absorber layer to their respective contacts; v) the electron and hole are extracted to the external circuit to do electrical work.

Device architecture

The device architecture is determined by the properties of the absorber material. For example, in a hybrid halide perovskite material the photogenerated electron and hole are loosely bound to one another and thermal energy is enough to separate them. In this case, a planar *n-i-p* architecture can be used, where *n* is a n-type (electron-doped) material contacted to the cathode, *p* is a p-type (hole-doped) material contacted to the anode and *i* is the intrinsic (undoped) perovskite material (Figure 1.2). In contrast, the photogenerated electron-hole pair in an organic solar cell is strongly bound. In this case, the electron-hole pair disassociate only at an interface and a mesoscopic architecture is used to facilitate this (Figure 1.2). The conventional organic architecture is *p-i-n*, where the anode and p-type material are deposited onto the substrate first. The conventional architectures can be inverted to give *p-i-n* junctions (for inorganic / hybrid absorber layers) or *n-i-p* junctions (for organic absorber layers). In all cases, the n-type and p-type layers provide a built-in electric field that drives photogenerated electrons towards the cathode material and photogenerated holes towards the anode.

Various strategies exist to increase device efficiency via device architecture engineering. For example, the current world record single junction silicon cell ($\eta = 26.6\%$) has an additional wide bandgap material inserted between the absorption layer and contact material to reduce interfacial recombination, and interdigitated back contacts to reduce optical loss.²⁴ The most efficient solar cells ($\eta = 46.0\%$) combine a multiple pn-junction (tandem) architecture with a lens to concentrate the incoming sunlight.

Efficiency and reciprocity

For an external circuit with load R , a current I and voltage V is developed across the cell so that

$$V = IR. \quad (1.1)$$

I and V are related by a current-voltage curve (Figure 1.3). A solar module operates at the maximum power point P_m , which is where the product of the voltage and current is maximum:

$$P_m = I_m V_m. \quad (1.2)$$

The open-circuit voltage V_{oc} is the voltage produced when there is no contact to the external circuit (or, equivalently, the external circuit has an infinite load). The short-circuit current I_{SC}

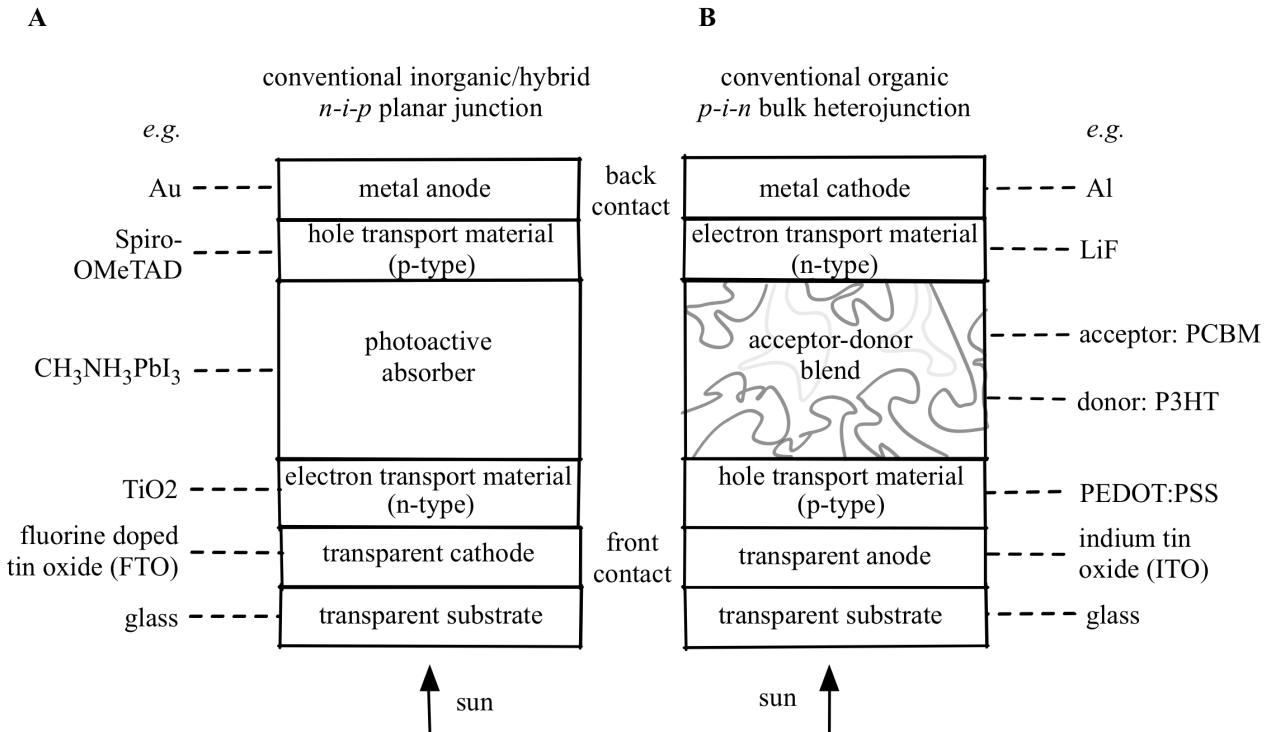


Figure 1.2: (A) Schematic of the typical planar junction solar cell architecture used for an inorganic or hybrid material absorber layer (B) Schematic of the typical bulk heterojunction solar cell architecture used for an organic absorber layer. The mesoscopic architecture provides many interfaces where the electron-hole pair can disassociate. In both cases there is a built-in electric field that drives photogenerated electrons towards the electron transport material and holes towards the hole transport material.

is the current that flows when there is no load on the external circuit. The fill factor FF is defined as:

$$\text{FF} = \frac{I_{\text{m}}V_{\text{m}}}{I_{\text{sc}}V_{\text{oc}}} \quad (1.3)$$

The higher the fill factor, the higher the maximum powerpoint for a given V_{oc} and I_{sc} .²⁵ A fill factor of one would correspond to a current-voltage curve which is not *actually* a curve, but a right angle.

The efficiency η of the solar cell under an incident light power of P_s is given by

$$\eta = \frac{P_{\text{m}}}{P_s} = \frac{I_{\text{m}}V_{\text{m}}}{P_s} = \frac{I_{\text{sc}}V_{\text{oc}}\text{FF}}{P_s} \quad (1.4)$$

Thus the three key figures of merit for a solar cell are the V_{oc} , I_{sc} and FF, and these combine to give the efficiency η . However in all absorber materials there is a trade off between current and voltage; as the bandgap of a material decreases, more photons can be absorbed (higher I_{sc}) but the photogenerated charge carriers have less energy (lower V_{oc}).

At open circuit, all electrons and holes must recombine in the solar cell. In an efficient PV material the recombination is radiative as this is a thermodynamically unavoidable process via

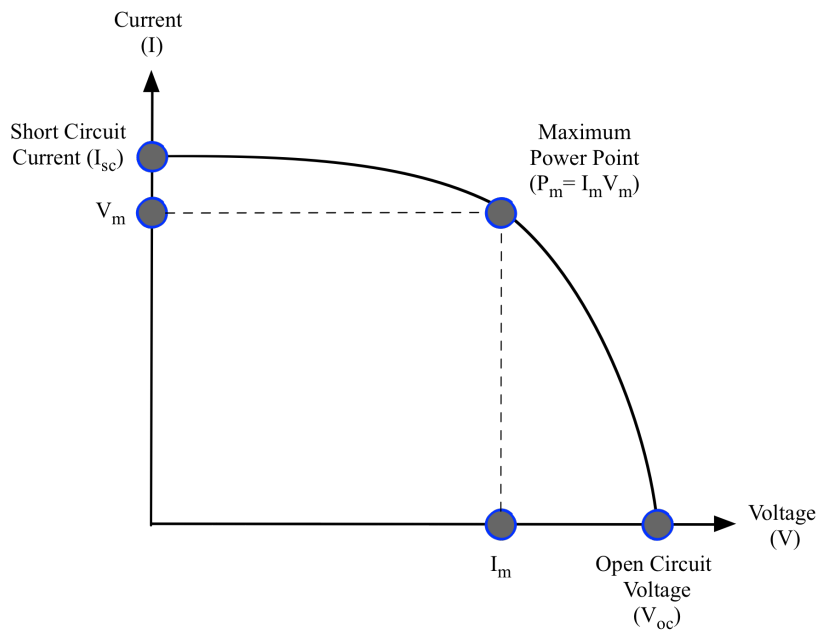


Figure 1.3: Schematic of a current-voltage curve for a typical solar cell.

the energy level transitions needed for absorption. Non-radiative recombination, where the energy is dissipated as heat and eventually lost, is avoidable and should be minimised. For a fixed carrier concentration, a higher rate of photon emission corresponds to reduced non-radiative recombination; high radiative efficiency (as measured through e.g. electroluminescence) translates to high open circuit voltage.²⁶ As a consequence of this reciprocity relation, we can predict the V_{oc} and I_{sc} from photoluminescence and photoconductivity studies respectively. This approach has been recently applied to hybrid halide perovskites.²⁷

The Shockley-Queisser limit

The principle of detailed balance states that at equilibrium each microscopic process is balanced by its reverse process: for a photovoltaic device operating at open-circuit this means that the rate of photon absorption equals the rate of photon emission. Shockley and Queisser used the principle of detailed balance to calculate the maximum possible efficiency of a photovoltaic device²⁸ (an alternative derivation is given in Ref. [25]). The PV efficiency is dependent upon the direct bandgap E_g of the absorber material and the spectrum of the incident light. Assuming illumination under a standard AM1.5 solar spectrum, the efficiency can be plotted as a function of bandgap. For a single junction solar cell the maximum possible efficiency across is 33%, which corresponds to an ideal bandgap of $\sim 1.4\text{eV}$ (Figure 1.4).

The model used to calculate the Shockley-Queisser limit is highly idealised. It assumes that all incident light is absorbed, that every absorbed photon creates an electron-hole pair, and that every electron is extracted to the external circuit. In real materials the absorption coefficient is not a step-function, and excited charge carriers can recombine through non-radiative processes

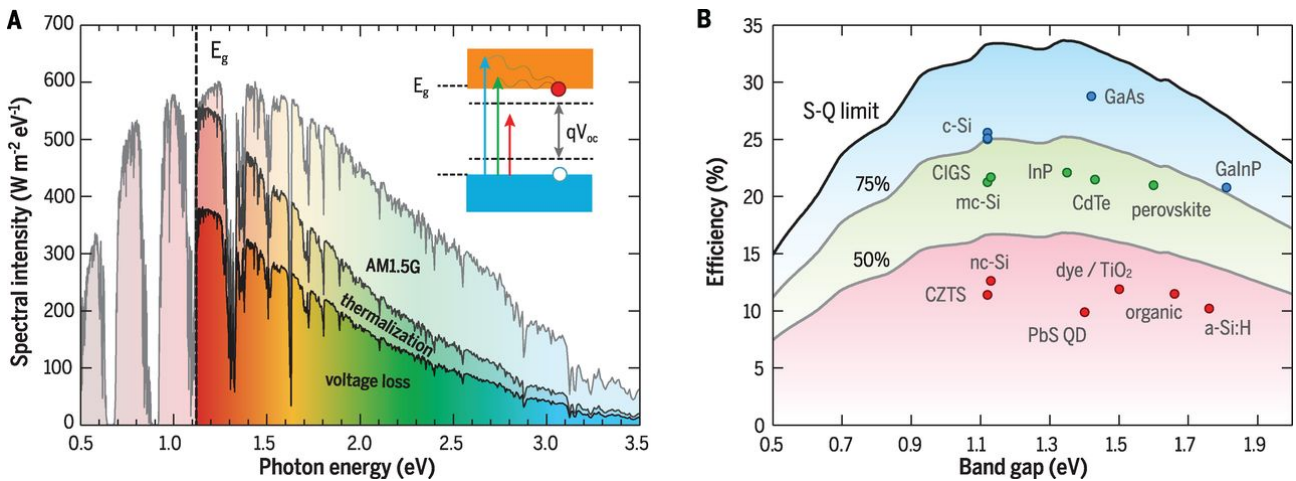


Figure 1.4: (A) The AM1.5 spectrum. Photons below the bandgap are not absorbed, whilst energy is lost from above bandgap photons via carrier thermalisation. (B) The Shockley-Queisser efficiency of a single bandgap solar cell under AM1.5 illumination (thick black line). Also included are the top cell efficiencies for various PV materials. Reprinted with permission from the work of Polman et al.²⁹

before reaching the circuit. Only three materials have an efficiency above 75% of the Shockley-Queisser limit: crystalline silicon (c-Si), GaAs and GaInP (Figure 1.4). Another metric, the spectroscopic limited maximum efficiency (SLME), accounts for absorption and emission characteristics and reduces the maximum theoretical efficiency.³⁰ For example, the candidate absorber material CuInS₂ has a Shockley-Queisser maximum efficiency of 33% and SLME of 29%.³¹ Non-radiative processes which contribute to the efficiency deficit will be discussed further in Section 1.2.2.

It is possible to exceed the Shockley-Queisser limit by challenging some of the assumptions built into the derivation. For example, the model assumes that once an electron is excited it will thermalise to the band edge, emitting the energy as phonons. This heat energy can no longer do useful work and results in a reduction of the V_{OC} . However ‘Hot carrier’ cells, which extract electrons before they are able to thermalise, were successfully fabricated in 2014 (although it should be noted that they are currently limited to cryogenic temperatures and an incoming spectrum which is intense and monochromatic).³²

Another approach is to use tandem solar cells, where several absorber materials are stacked on top of each other. The materials are chosen to have complementary bandgaps, so that more of the solar spectrum can be absorbed with minimal thermalisation losses. GaAs-based four-junction tandem cells have reached an efficiency of 33% and are used for space applications, though their uptake is limited by the costly wafer bonding method required for fabrication. The constraint of lattice matching – that the strain at the interfaces must be minimised for device stability – puts severe limitations on the material combinations which can be used for this approach.

1.2.2 Carrier recombination

Electron-hole recombination competes with charge extraction to the external circuit, and as such it is a well examined process. Three pathways for electron-hole recombination are outlined in Figure 1.5. During radiative recombination the electron directly recombines with a hole to produce a photon and, in the case of indirect recombination, phonons. This recombination channel is unavoidable in PV devices as the same channel is used for light absorption. The second pathway, Shockley-Reed-Hall (SRH) recombination, is a two step process mediated via a trap state. In PV devices this pathway should be minimised as the kinetic energy of the electron and hole is transformed to vibrational energy (phonons) and cannot be used for useful work. The third pathway, Auger recombination, is also a non-radiative process. Here the electron directly recombines with a hole, and the resulting energy and momentum is transferred to another conduction band electron.

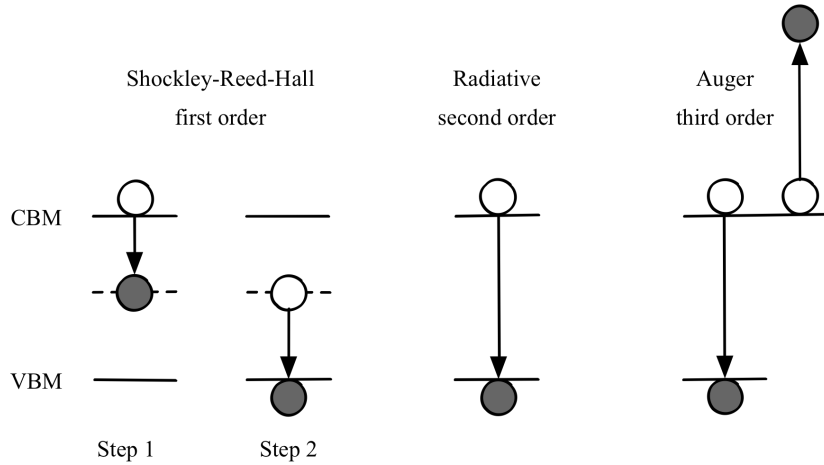


Figure 1.5: A schematic of the three possible electron-hole recombination pathways. In each case, an electron at the conduction band minimum combines with a hole at the valence band maximum. First-, second- and third-order processes correspond to one, two and three particle processes respectively.

Radiative recombination and Auger recombination are unavoidable processes intrinsic to the material, whereas SRH recombination is an avoidable process that can be controlled through defect engineering. The SRH recombination rate is given by

$$U_{\text{SRH}} = \frac{np - n_i^2}{\tau_{n,\text{SRH}}(p + p_t) + \tau_{p,\text{SRH}}(n + n_t)}, \quad (1.5)$$

where n (p) is the density of electrons (holes), n_i is the intrinsic carrier density and n_t (p_t) is the value of the electron (hole) density when the electron Fermi level is equal to the trap level E_t :

$$n_t = n_i e^{\frac{(E_t - E_c)}{k_B T}} \quad (1.6)$$

$$n_p = n_i e^{\frac{(E_v - E_t)}{k_B T}}, \quad (1.7)$$

where E_c and E_v are the energies of the CBM and VBM respectively. The recombination rate has a maximum when the rates of hole capture and electron capture are comparable. This happens when the trap level is in the middle of the bandgap, and $n_t = p_t$.

$\tau_{n,\text{SRH}}$ ($\tau_{p,\text{SRH}}$) is the electron (hole) lifetime. For a trap density N_t , mean thermal electron (hole) velocity v_n (v_p) and electron (hole) capture cross section σ_n (σ_p), the lifetimes can be approximated as

$$\tau_{n,\text{SRH}} = \frac{1}{v_n \sigma_n N_t} \quad (1.8)$$

$$\tau_{p,\text{SRH}} = \frac{1}{v_p \sigma_p N_t}. \quad (1.9)$$

The standard approach for calculating the trap density from first principles is give in Chapter 3, and a method for calculating the capture cross section is outlined in the results Chapter ??.

Experimental measurements of recombination rates

Carrier lifetimes and recombination rates are difficult to measure experimentally as ultra fast optical and electronic sensors are needed to capture transient behaviour, and this must be done in conditions relevant to photovoltaic performance. Time resolved photoluminescence (TRPL) and photoconductivity measurements are used to infer the recombination rates for each recombination pathway. Each pathway scales differently with carrier concentration, as specified by the following rate equation:

$$\frac{\delta n}{\delta t} = -k_1 n - k_2 n^2 - k_3 n^3 \quad (1.10)$$

where k_1 is the rate constant for SRH recombination, k_2 is the rate constant for radiative recombination and k_3 is the rate constant for Auger recombination. SRH recombination via a trap state is a one particle process that scales linearly with the carrier concentration. Radiative recombination is a two particle process that depends on the electron density (n_e) and hole density (n_h), so scales quadratically with carrier concentration. Auger recombination requires three particles and scales cubically. TRPL uses short laser pulses to excite excess electrons and holes which then decay via recombination or carrier extraction at an interface. Exponential curves are fitted to the TRPL signal at different laser fluences to extract carrier lifetimes. In general, for solar cells operating under 1.5AM illumination, second order SRH recombination is the dominant recombination mechanism.

1.2.3 Design principles for absorber materials

Solid state physics and computational chemistry can connect microscopic material processes to macroscopic observables. The tools of each field have been applied to a range of inorganic and organic materials, and have successfully explained the observed properties of existing materials. There is also a more recent approach to materials science called “inverse design”. This is where

the desired functionality of a new material is stated first, and computational tools are used to predict which materials will exhibit such features.³³ The hope is that this approach will improve upon discovery by trial and error, and accelerate the design of new materials.

High-throughput computational screening is a brute force approach to inverse design. Here, an automated procedure calculates a set of properties across a large number of atomic structures. This approach has been used to identify battery electrolytes,³⁴ organic photovoltaic materials³⁵ and materials for carbon capture and storage,³⁶ amongst others. Materials screening criteria must be defined so that successful materials are identified and selected for further study. Some criteria are easy to identify - for example the thermodynamic stability, which ensures that the material is synthesisable. This criteria can be expanded to include the features found in existing successful materials. For example, hybrid halide perovskites are defect tolerant - they contain a low concentration of defects which are detrimental to opto electronic performance. The electronic parameters which underpin the defect tolerance of hybrid halide perovskites have been identified so that they may be used to screen for new defect-tolerant materials.³⁷

With the concept of inverse design in mind, items for a successful PV material “shopping list” are listed below. The final three items (toughness, elemental abundance, elemental non-toxicity) are not necessary for successful devices in the lab, but would promote commercialisation of the technology.

Thermodynamic stability

The material should be thermodynamically stable with regard to competing phases so that it does not degrade over years of operation. The binary compound CdTe was the first thin film PV material to be commercialised and, similar to GaAs, it has no competing phases. Quaternary chalcogenide compounds such as CISSe and CZTS have many more competing phases to consider and the chemical potentials during synthesis must be very finely tuned for stability, which hinders their development.

Optimum bandgap

Ultimately, it is the spectrum of the sun and features of our atmosphere (light scattering and absorption) that dictates the design of solar cells; we must optimise our solar technology to take advantage of the spectrum that is particular to our planet. The Shockley-Queisser limit, discussed in subsection 1.2.1, gives an optimum bandgap of 1.4 eV.³⁸ Atomic disorder or point defects can reduce the material band gap. Quaternaries with elemental species of a comparable atomic radii are more likely to exhibit atomic disorder – for example in CZTS this leads to a bandgap reduction of 30 meV.³⁹

Strong light absorption

The absorption coefficient specifies how much light of a particular wavelength is absorbed by a material. Different semiconductor materials have different absorption coefficients; those with a higher absorption coefficient will more readily absorb light. Silicon is an indirect bandgap material that requires phonon-assisted absorption. As a result, crystalline silicon absorbs 92% of light in a thickness of 200 µm, whilst CdTe can absorb the same amount in a thickness of 1 µm.⁴⁰

Low exciton binding energy

After light absorption, a bound electron-hole pair (exciton) is created. The electron and hole must disassociate so that they can travel to their respective contacts. Here, the dielectric response is key, as this determines how readily a material will screen electrostatic perturbations. Organic solar cell materials are limited by low dielectric constants ($\epsilon_0 \approx 3 - 4$) that lead to large exciton binding strengths.⁴¹ In inorganic or hybrid materials the dielectric constants are higher ($\epsilon_0 = 10.4$ for CdTe,⁴² whilst values vary from $\epsilon_0 = 16.6$ to $\epsilon_0 = 28.5$ for MAPI⁴³).

High carrier mobility

Some materials may have suitable optical properties but are unable to transport the photo-generated charge efficiently to the contact layers. Carrier mobility quantifies how quickly an electron or hole can move through a material when pulled by an electric charge. Light carrier effective masses (high band dispersions) correspond to higher mobilities. However light effective masses are not sufficient in themselves as there are various scattering channels to consider: lattice scattering, carrier-carrier scattering and defect scattering. The most significant scattering mechanisms in a PV material are lattice scattering and ionized defect scattering. A high dielectric constant is beneficial to carrier mobility as the rate of ionized defect scattering is proportional to $\frac{1}{\epsilon^2}$. The composition of the material is also important – for example, vacancies in gallium nitride (Ga(3+)N(3-)) carry a larger charge and have a larger scattering cross section than vacancies in MAPI ($CH_3NH_3(1+)Pb(2+)I(1+)_3$).

Long carrier lifetime

Carrier lifetime has already been discussed in the context of electron-hole recombination in Section 1.2.2. Whereas the concentration of defects is important for carrier mobility, here it is the energy of defect states with respect to the valence and conduction band which is important. This is discussed in Chapter ???. In summary, the key is to minimise non-radiative recombination via deep level defect states (also known as “killer defects”). Carrier diffusion length, another important figure of merit with regard to carrier transport, is proportional to the product of carrier mobility and lifetime.

Compatibility

For efficient charge extraction, the PV absorber layer must be compatible with suitable contact and/or buffer layers. Firstly, the energy levels of the interfacing materials must align so that there is an electrical potential gradient to extract the charge, without significant loss of V_{OC} . For example, band mis-alignments are reported to be the source of poor photovoltaic efficiencies in the candidate absorber materials BiSI and BiSeI.⁴⁴ Secondly, lattice mismatch at the interface should be avoided as this can lead to deep point defects that provide sites for non-radiative recombination and, in the case of more severe strain, an incoherent interface with many defect sites and weak chemical bonding. Computational screening procedures can be used to identify potential electronically and structurally matched contact layers and this has been recently applied to the hybrid halide perovskites.⁴⁵

Toughness

Silicon is a brittle material; the majority of Si material in a solar cell is used as a mechanical carrier to prevent crack propagation, and glass must be used as a protective layer. The resulting cell is often too heavy to be installed on structures which are made from wood or sheet metal. In addition, the bulk of system costs are higher for heavier cells. Organic photovoltaics, and to some extent perovskites, are tougher and can be made using roll-to-roll print processes onto a flexible substrate.

Elemental abundance

The power generated from PV installations must exceed 1 TW to make a real impact on global carbon emissions.⁴⁶ To meet this demand, PV materials must be made from abundant elements that are in ready supply at reasonable cost. To quantify this criteria, the Herfindahl–Hirschman index (HHI), which is used in economics as a measure of market concentration, can be applied to elements. The HHI indicates that Si is abundant but that production is highly concentrated in a few countries. Elements common to the third generation of materials—Cu, Zn, S, Se, Sn—are less abundant but their production is more highly distributed across the globe.⁴⁷

Elemental non-toxicity

Finally, toxic elements may hinder the successful commercialisation of future PV technologies. The problem is not insurmountable; cadmium telluride is toxic if ingested but is a commercial solar cell material. Encapsulation and recycling can reduce any risk, but add another level of complexity to the development of new solar technologies.

1.3 Summary

To reduce the rate of climate change we must decrease our reliance on fossil fuels, and increasing the proportion of photovoltaic energy is one way to achieve this. This may only be politically feasible if the costs associated with PV energy can continue to exponentially decrease. As the well-established silicon technologies are limited by high capital expenditures, there is an incentive to develop new low-cost, high-efficiency and reliable technologies. Flexible thin-film architectures also allow for expansion into the new market of building integrated photovoltaics. Currently no material has met these requirements,⁴⁸ although promising performance from emerging technologies such as the hybrid halide perovskites motivates further research.

1.4 Format of the thesis

Organic-inorganic halide perovskites, the subject of this thesis, present a number of challenges for first-principles atomistic materials modelling. These ‘plastic crystals’ feature dynamic processes across multiple length-scales and time-scales, which include mixed ionic-electronic transport, highly anharmonic lattice dynamics and strong relativistic (spin-orbit coupling) effects on the electronic band structure. These issues, which affect the operation of solar cells, are outlined in the following chapter. This is followed with a brief introduction to the theory that underlies almost all of the work in this thesis - Density Functional Theory (DFT). To model an imperfect material (one with crystal defects), or temperature effects, a series of post-processing steps must follow the DFT calculation. These are also outlined in Chapter Three.

Chapters Four–Six contain the thesis results. Each results chapter also contains any additional theory where required and calculation steps. Bulk transport and optical properties of the perfect material are calculated using Effective Mass Theory (EMT) in Chapter Three. EMT often assumes a parabolic electronic band dispersion, in this chapter distortions away from parabolicity are considered. Temperature effects, described on a microscopic scale by phonon quasi-particles, are introduced in Chapter Four. At room temperature the inorganic octahedral PbI_3 units tilt back and forth, and the coupling strength between this tilting and the electronic sub-system is quantified. Point defects are introduced to our model in Chapter Six. Point defects can be benign or harmful to device performance, depending upon the properties of the defect. This chapter reports the properties of the iodine interstitial point defect.

I've learned that I still have a lot to learn.

— Maya Angelou

2

Theory and simulation of hybrid halide perovskites

2.1 Introduction

In this chapter, we address recent progress and current challenges in theory and simulation of hybrid perovskites. We pay particular attention to predicting properties that assess the photovoltaic potential of a material. Factors to consider include: light absorption, charge transport, absolute band energies, defect physics and chemical stability.

The perovskite mineral, CaTiO_3 , is the archetype for the structure of many functional materials.⁴⁹ Metal halide perovskites have been studied for their semiconducting properties since the 1950s⁵⁰; yet only recently have organic-inorganic perovskites such as $\text{CH}_3\text{NH}_3\text{PbI}_3$ (MAPI) been applied to solar energy conversion, showing remarkably strong photovoltaic action for a solution processed material.⁵¹ The field has progressed rapidly in the past eight years, with the increase in power conversion efficiency supported by over three thousand research publications.^{52–56} Other potential application areas of these materials include thermoelectrics,^{57,58} light-emitting diodes,^{52,59} and solid-state memory.^{60,61}

These materials combine a complex crystal structure, modulated by static and dynamic disorder, with a multifarious electronic structure requiring methods beyond density functional theory to treat many-body and relativistic effects. As such, the halide perovskites represent a challenge to predictive materials modelling, in a system of great experimental interest, and where there is considerable motivation to improve on the status quo.

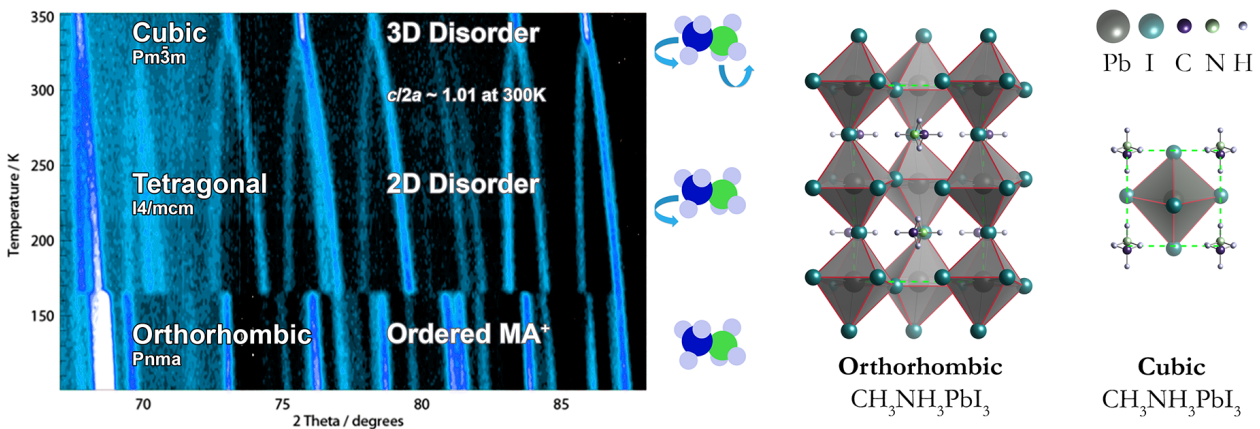


Figure 2.1: The high-resolution powder neutron diffraction pattern of the hybrid halide perovskite $\text{CH}_3\text{NH}_3\text{PbI}_3$ is shown in the left panel (adapted with permission from Ref.⁶² based on data in Ref.⁶³), which illustrates the low and high temperature phase transitions. While an ordered CH_3NH_3^+ sub-lattice is expected in the orthorhombic phase, orientation disorder increases with temperature. The crystallographic unit cells of the pseudo-cubic and orthorhombic perovskite phases are shown in the right panel (adapted with permission from Ref.⁶⁴). The associated structure files can be accessed from <https://github.com/WMD-group/hybrid-perovskites>. Figure prepared by Aron Walsh.

2.2 Crystal structures and lattice dynamics

2.2.1 Phase diversity

(Hybrid) perovskites of the type ABX_3 form a crystal structure with an (organic) A site cation contained within an inorganic framework BX_3 of corner sharing octahedra. Halide substitution on the X site ($\text{X} = \text{Cl}^-, \text{Br}^-, \text{I}^-$), metal substitutions on the B site ($\text{B} = \text{Pb}^{2+}, \text{Sn}^{2+}$), and cation substitution on the A site ($\text{A} = \text{CH}_3\text{NH}_3^+, \text{HC}(\text{NH}_2)_2^+, \text{Cs}^+, \text{Rb}^+$) lead to varied chemical and physical properties.^{65,66} In addition to isoelectronic substitutions (e.g. replacing Pb^{2+} by Sn^{2+}), it is possible to perform pairwise substitutions to form double perovskites (e.g. replacing 2Pb^{2+} by Bi^{3+} and Ag^+).^{67,68}

In the first report of $\text{CH}_3\text{NH}_3\text{PbI}_3$ by Weber in 1978, the crystal structure was assigned as cubic perovskite (space group $Pm\bar{3}m$).^{69,70} The anionic PbI_3^- network is charge balanced by the CH_3NH_3^+ molecular cation. The symmetry of CH_3NH_3^+ (C_{3v}) is incompatible with the space group symmetry (O_h) unless orientation disorder (static or dynamic) is present. The crystal structure solved from X-ray or neutron diffraction data usually spread the molecules over a number of orientations with partial occupancy of the associated lattice sites. A common feature of perovskites is the existence of phase changes during heating (typically from lower to higher symmetry) as shown in Figure 2.1. In hybrid halides containing methylammonium, these are orthorhombic ($Pnma$), tetragonal ($I4/mcm$) and cubic ($Pm\bar{3}m$) phases.⁶³ For $\text{CH}_3\text{NH}_3\text{PbI}_3$ the $Pnma$ to $I4/mcm$ phase transition is first-order with an associated discontinuity in physical properties, while the $I4/mcm$ to $Pm\bar{3}m$ phase transition is second-order with a continuous evolution of the structure and properties.^{63,71}

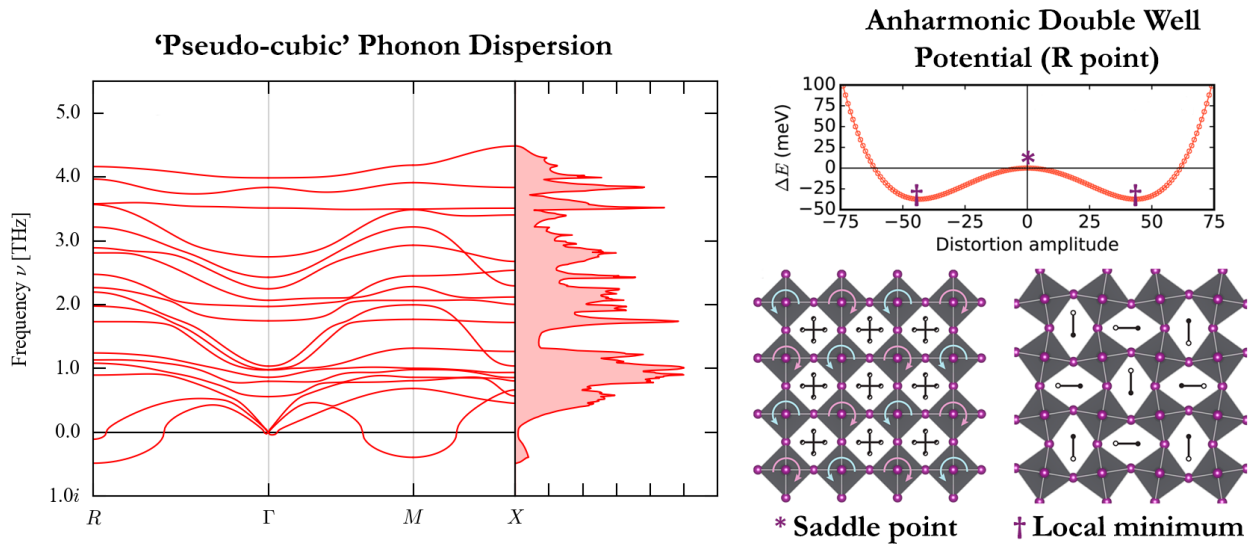


Figure 2.2: (Left) The harmonic phonon dispersion for $\text{CH}_3\text{NH}_3\text{PbI}_3$ from a ‘pseudo-cubic’ structure. The imaginary frequencies of acoustic modes at the M ($q = \frac{1}{2}, \frac{1}{2}, 0$) and R ($q = \frac{1}{2}, \frac{1}{2}, \frac{1}{2}$) Brillouin zone boundary correspond to an instability expressible in a supercell as alternate tilting of the octahedra. (Right) Following the imaginary acoustic mode at the R Brillouin zone boundary in a $2 \times 2 \times 2$ supercell expansion shows a double-well potential in the DFT internal energy. The saddle point corresponds to a $1 \times 1 \times 1$ cubic structure, whilst the two local minima correspond to a distorted structure of lower symmetry. The energy barrier is small enough to allow both minima can be accessed at room temperature, so the system is expected to exhibit dynamic rather than static disorder. Similar behaviour is found at the M point. Figure adapted by Aron Walsh with permission from Refs.⁷⁷ and⁷⁸. The underlying phonon data is available from <https://github.com/WMD-group/Phonons>.

The phase transitions are linked to a change in the tilting pattern of the inorganic octahedral cages, and order-disorder transitions of the molecular sub-lattice.^{71–73} X-ray diffraction (XRD) measurements upon cooling (heating) suggest the incursion of tetragonal in orthorhombic phases (and vice versa),⁷⁴ which is common for first-order solid-state phase transitions.

Similar phase behaviour tends to be seen for other compositions; however, the transition temperatures vary. In $\text{CH}_3\text{NH}_3\text{PbI}_3$ the orthorhombic to tetragonal transition temperature is 162 K, becoming cubic by around 328 K, while $\text{CH}_3\text{NH}_3\text{PbBr}_3$ is cubic above 237 K.⁷⁵ In addition, compounds such as $\text{HC}(\text{NH}_2)_2\text{PbI}_3$ (FAPI) and CsSnI_3 feature a phase competition between a corner-sharing perovskite octahedra (black in appearance) and an edge-sharing octahedra molecular crystal (yellow or white in appearance).⁷⁶ Only the corner-sharing perovskite phase is of interest for solar energy applications.

2.2.2 Local and average crystal environment

The first electronic structure calculation of hybrid halide perovskites was by Chang, Park and Matsuishi in 2004,⁷⁹ in the local density approximation (LDA) of density functional theory (DFT). They modelled a static structure where the CH_3NH_3^+ molecule was aligned along $\langle 100 \rangle$ (towards the face of the corner-sharing PbI_3^- framework), but found that the barrier for rotation

to $\langle 111 \rangle$ was less than 10 meV. This small barrier for cation rotation gave credence to a prior model that the molecular sub-lattice was dynamically disordered.⁷⁵ Similar barriers were later found within the generalised gradient approximation (GGA) of DFT.⁸⁰

Ab initio molecular dynamics (MD), neutron scattering^{81,82} and time-resolved infra-red⁸³ data all indicate a 1–10 picosecond reorientation process at room temperature. As a result of (by definition) anharmonic molecular rotation, and large-scale dynamic distortions along soft vibrational modes, the local structure can deviate considerably from that sampled by diffraction techniques, which do not probe local disorder that preserves long-range order on average. Knowledge of these locally broken symmetries is essential for meaningful electronic structure calculations, where the broken symmetry results in a lifting of degeneracy, and a potentially quite different solution.

In spite of the larger cation, FAPI appears to possess a similar timescale of rotation to MAPI⁷⁶. A lighter halide (and therefore smaller cage) results in faster rotation, in spite of the greater steric hindrance.⁸⁴ Together, these data suggest that the molecular rotation is a function of the local inorganic cage tilting, where the relatively insignificant mass of the organic cation follows the pocket distortion.

The spontaneous distortions can also be observed in the vibrational spectra. The calculated harmonic phonon dispersion for MAPI in the cubic phase is presented in Figure 2.2. The acoustic modes soften as they approach the M ($q = \frac{1}{2}, \frac{1}{2}, 0$) and R ($q = \frac{1}{2}, \frac{1}{2}, \frac{1}{2}$) Brillouin zone boundaries. This zone boundary instability can only be realised in an even supercell expansion, where it corresponds to anti-phase tilting between successive unit cells. This behaviour is characteristic of the perovskite structure, and can be described by the Glazer tilt notation.^{85,86}

Within the frozen-phonon approximation the potential energy surface can be traced along the soft acoustic M and R modes. In both cases this results in a double well with an energy barrier $\sim k_B T$ at the saddle point.⁷⁷ At room temperature the structure is dynamically disordered, with continuous tilting. The structure is locally non-cubic but only possesses cubic Bragg scattering peaks.⁸⁷ Indeed, MD simulations show continuous tilting of MAPI and FAPI at room temperature.^{76,88,89} As temperature decreases, the structural instability condenses via the R point (with an energy barrier of 37 meV) into the lower symmetry tetragonal phase. This is followed by condensation of the M point (with an energy barrier of 19 meV) to the orthorhombic phase.⁷⁷ Whilst the molecular cation continuously rotates with the inorganic tilts in the cubic phase, and is partly hindered in the tetragonal phase, it can only librate in the low temperature orthorhombic phase.

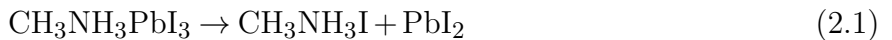
In the static picture—as in the case of an electronic band structure calculated for a single ionic snapshot—the organic cation plays no direct role in optoelectronic properties of the material as the molecular electronic levels lie below that of the inorganic framework. Once motion is considered, the electrostatic and steric interaction between the organic molecule and inorganic

framework couples tilting and distortion of the octahedra to the organic cation motion. These tilts and distortions vary the orbital overlap between states, perturbing the band-structure and band-gap.^{77,89–91} The electronic structure thus becomes sensitive to temperature, which will be discussed further in Section II.

2.2.3 Thermodynamic and kinetic stability

Ab initio thermodynamics has emerged as a powerful tool in materials modelling, with the ability to assess the stability of new materials and place them on equilibrium phase diagrams even before experimental data is available.^{92–94} The total energy from DFT calculations approximates the internal energy of the system. By including lattice vibration (phonon) and thermal expansion contributions, the Gibbs free energy and other thermodynamic derivatives can be evaluated.⁹⁵ In the context of photovoltaic materials, this has been applied to Cu₂ZnSnS₄ and used to identify the processing window where a single-phase compound can be grown in equilibrium.⁹⁶

An issue with hybrid perovskites and other metal-organic frameworks is that the calculated heat of formation is close to zero. The decomposition reaction



has been predicted to be exothermic. Subsequent calorimetric experiments have supported the prediction that hybrid lead halide perovskites are metastable.⁹⁷ It is likely that these materials are only formed due to entropic (configurational, vibrational and rotational) contributions to the free energy.

The concept of metastable materials is attracting significant interest.^{98–101} These are materials that do not appear on an equilibrium phase diagram but can be synthesised with a finite (useful) lifetime. For such materials, the chemical kinetics become critical. Though these can be calculated with first-principles techniques, this is a more cumbersome and costly process than equilibrium bulk thermodynamics, which requires only total energies of local minimum structures. To our knowledge, there have been no rigorous attempts to model the kinetics of decomposition pathways for hybrid perovskites over complete chemical reactions.

2.2.4 Anharmonic lattice vibrations and thermal conductivity

Kohn-Sham density functional theory is most often carried out in the Born-Oppenheimer approximation where the nuclei are static classical point charges. To consider thermal vibrations, expansion or heat flow the theoretical framework of lattice dynamics can be used.⁹⁵

The description of collective vibrational excitations in crystals can be simplified with second quantization to the creation and annihilation of phonons quasiparticles. In the harmonic approximation, the lattice dynamics are fully specified by second-order force-constants of individual atoms, which are then readily constructed into the dynamical matrix. The eigenstates of this

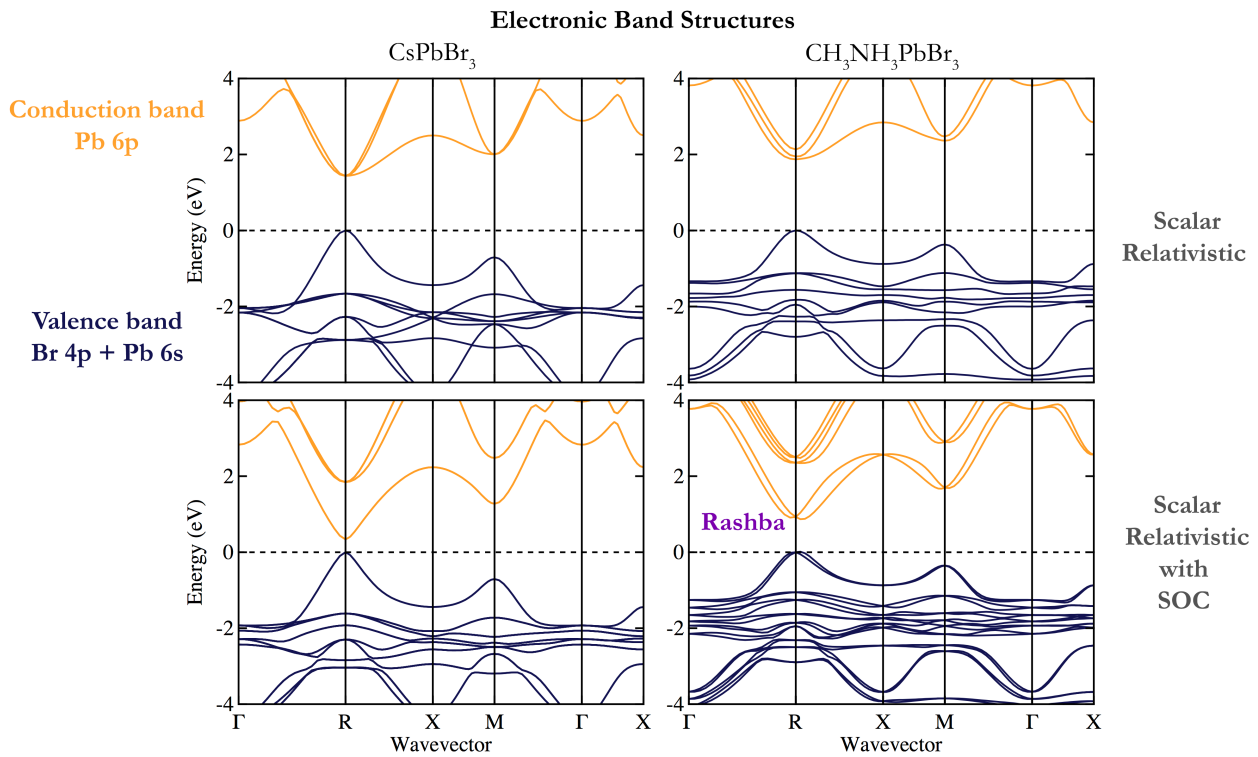


Figure 2.3: The electronic band structures of the inorganic perovskite CsPbBr_3 and hybrid perovskite $\text{CH}_3\text{NH}_3\text{PbBr}_3$ in the cubic phase. One effect of the organic cation is to widen the band-gap located at the R point due to the larger lattice constant. Spin-orbit coupling reduces the band-gap in both materials. The presence of CH_3NH_3^+ in the hybrid perovskite results in a non-centrosymmetric crystal, with an associated relativistic Rashba-Dresselhaus splitting of the lower conduction band. While labels of the special points are those of the cubic perovskite structure (space group $Pm\bar{3}m$), the static model of the hybrid perovskite formally has $P1$ symmetry. Points equivalent for a cubic crystal (e.g. $M = \frac{1}{2}, \frac{1}{2}, 0$; $M' = 0, \frac{1}{2}, \frac{1}{2}$; $M'' = \frac{1}{2}, 0, \frac{1}{2}$) are inequivalent here. Figure prepared by Young-Kwang Jung.

matrix are the normal modes of vibration with an associated phonon energy. Thermal expansion coefficients, system anharmonicity (e.g. modal Grüneisen parameters) and the temperature-dependence of other properties can be calculated in the quasi-harmonic approximation (QHA). Here the lattice dynamics is harmonic at a given temperature; however, the cell volume is scaled by thermal expansion to give the first-order contribution of finite temperature effects.

The thermal expansion coefficient of MAPI in the cubic phase has been calculated with the QHA. The value is sensitive to the density functional used. For example, a value of $3.0 \times 10^{-5}/K$ is calculated with the PBE functional with Tkatchenko-Scheffler dispersion corrections,⁹¹ while the PBEsol functional produces a value of $12.5 \times 10^{-5}/K$.⁶⁴ These compare to finite temperature scattering measures of $1.91 \times 10^{-5}/K$ by X-ray,¹⁰² and $13.2 \times 10^{-5}/K$ by neutron diffraction.⁶³ Even taking the smallest value above, the expansion coefficient is one order of magnitude greater than silicon,¹⁰³ highlighting the strong deviation from harmonic behaviour in halide perovskites.

In the harmonic approximation (and similarly the QHA), the dynamic matrix eigenmodes are orthogonal and the resulting phonons are non-interacting. Consequently phonon lifetimes are infinite as the phonons do not scatter; thermal conductivity is infinite. To calculate

phonon-phonon scattering, and so its contribution to finite thermal conductivity, anharmonic lattice dynamics need to be considered. A computational route is to use perturbative many-body expansion, e.g. as implemented in PHONO3PY,¹⁰⁴ which includes third-order force constants. For $\text{CH}_3\text{NH}_3\text{PbI}_3$, 41,544 force evaluations are required for these third-order force constants, compared to 72 for second-order (harmonic) force constants.⁷⁷ Consequently, these calculations are vastly more expensive. Using this approach phonon-phonon scattering rates are calculated to be three times larger in MAPI compared to standard covalent semiconductors CdTe and GaAs.⁷⁷ The phonons barely exist for a full oscillation before they split or combine into another state. Consequently, mean free paths are on the nanometer rather than more typical micrometer scale. Lattice thermal conductivity is extremely low, $0.05 \text{ Wm}^{-1}\text{K}^{-1}$ at 300 K.⁷⁷ This combination of high electrical and low thermal conductivity makes these compounds potential thermoelectrics.^{57,58}

In highly anharmonic systems third-order force constants and perturbation theory may not be sufficient to describe the true dynamics, but going further with lattice dynamics becomes prohibitive. Besides, it is not obvious whether the fundamental tenant of lattice dynamics, of expanding in small displacements around a minimum structure, is correct for these soft and highly anharmonic materials. In contrast, MD treats anharmonic contributions to all orders, but as it stochastically explores the phase space, long integration times are required to sample rare events. Finite size effects mean that only phonon modes commensurate with the supercell are sampled. The Green-Kubo relations express transport coefficients in terms of time correlation functions, which can be directly sampled from molecular dynamics.¹⁰⁵ Using this method the thermal conductivity of MAPI is calculated to be $0.31 \text{ Wm}^{-1}\text{K}^{-1}$ at 300 K.¹⁰⁶ Although still ultra-low, this is greater than that calculated by perturbation theory. The thermal conductivity of the tin and bromide analogues were found to be higher than lead iodide due to a higher elastic stiffness.¹⁰⁶

2.3 Electronic structure

Despite the dynamic disorder just discussed, in many respects halide perovskites display characteristics of traditional inorganic semiconductors, with a well-defined electronic band structure and electron/hole dispersion relations. However, subtleties emerge upon closer examination, when the electronic structure is correctly modelled.

2.3.1 Many-body and relativistic effects

Perhaps surprisingly, local and semi-local exchange-correlation functionals provide a reasonable estimate for the band-gaps of these heavy metal halide materials. This is due to a cancellation of errors. For Pb-based perovskites, the conduction band has mainly Pb 6p character. Due to the large nuclear charge, the electronic kinetic energy requires a relativistic treatment, and

spin-orbit coupling (SOC) becomes significant. The first-order effect is a reduction in band-gap by as much as 1 eV¹⁰⁷, as the degenerate 6p orbitals are split and moved apart. This is shown in Figure 2.3 for the bromide compounds. The typical band-gap underestimation of GGA functionals is offset by the absence of relativistic renormalisation.

SOC is not expected to have a large impact on the structural properties of the Pb-based compounds as the (empty) conduction band is mainly affected, and the force on atoms depends on the electron density (occupied orbitals). Accurate force-constants can be calculated without SOC considerations.¹⁰⁸

There have been a number of electronic structure calculations considering many-body interactions beyond DFT. Quasi-particle self-consistent *GW* theory shows that the band dispersion (and so density of states, optical character and effective mass) is considerably affected by both the *GW* electron correlation and spin-orbit coupling.¹⁰⁷ Some materials see only a rigid shift of band structure (retaining DFT dispersion relations)^{45,109} but this is not the case for hybrid perovskites. This point has not been fully appreciated, in part because DFT codes are more widespread and convenient to generate data.

A consequence of SOC when combined with a local electric field is the Rashba-Dresselhaus effect, a splitting of bands in momentum space.¹¹⁰ This can be understood as an electromagnetic effect, where the magnetic moment (spin) of the electron interacts with a local electric field, to give rise to a force which displaces it in momentum space. Up and down spins are displaced in opposite directions, and this displacement is a function (in both size and direction) of the local electric field, which will depend on the local dynamic order. For a static structure, this is demonstrated in Figure 2.3 for CH₃NH₃PbBr₃. Neglecting SOC, the cubic phase has band extrema at the *R* point (a direct band-gap). With SOC the valence and conduction band each split into valleys symmetrical around *R*. The splitting is much more pronounced in the Pb 6p conduction band (compared to the Br 4p valence band), as expected from the Z^4 dependence of spin-orbit coupling. This asymmetry in the band extrema results in direct-gap like absorption and indirect-gap like radiative recombination which we discuss later.

The relativistic spin-splitting can only occur in crystals that lack a centre of inversion symmetry, a prerequisite for generating a local electric field. The cubic representation of CsPbBr₃ has an inversion centre, so while SOC affects the band-gap through the separation of Pb 6p into p_{1/2} and p_{3/2} combinations, no splitting of the band extrema away from the high symmetry points is observed (see Figure 2.3). This is true only for a static cubic structure. As discussed earlier, hybrid halides will have continuous local symmetry breaking. Calculations based on such static high symmetric structures can be misleading, and not representative of the real system.

Point defect calculations will be particularly sensitive to the electronic structure method used. Neglect of SOC and self-interaction errors can result in an incorrect position of the valence or conduction band edges, thus introducing spurious errors in defect energy levels and predicted

defect concentrations. Du¹¹¹ showed how for the case of an iodine vacancy, a deep (0/+) donor level is predicted for GGA-noSOC, while a resonant donor level is predicted for GGA-SOC and HSE-SOC treatments of electron-exchange and correlation.

2.3.2 Electron-phonon coupling

Going beyond the Born-Oppenheimer approximation with perturbation theory, we can consider the interaction of the electronic structure with vibrations of the lattice. Electron-phonon coupling can perturb the electronic band energies (changing the band-gap), and couple electronic excitations (the hole and electron quasi-particles) into vibrational excitations (phonon quasi-particles). In a semiconductor, charge carrier scattering is often dominated by this electron-phonon interaction, and so the strength of these processes set a limiting value on the mobility. Electron-phonon coupling is often calculated in a second-order density functional perturbation theory calculated for a static (rigid ion) structure. In the normal limit, this term is expected to dominate over the first order contribution from the acoustic deformation potential as vibrations are typically small. These calculations are difficult to converge, as integration is over both electronic and vibrational reciprocal space, and the electron-phonon interaction is often found to be a non-smooth function.¹¹²

In recent work⁷⁷ we developed a method to calculate the electron-phonon interaction of soft modes, and applied this to the acoustic zone boundary tilting modes in hybrid halide perovskites described earlier. Here we solved a one-dimensional Schrödinger equation for the nuclear degree of freedom along the phonon mode, and then combine the resulting thermalised probability density function (which includes zero point fluctuations and quantum tunnelling) with a band-gap deformation potential along this mode. The method includes quantum nuclear motion, goes beyond the harmonic regime, but only contains the first-order contribution to the electron-phonon coupling of the band-gap deformation. A positive band-gap shift of 36 meV (R point phonon) and 28 meV (M point phonon) is predicted at $T = 300$ K. Saidi et al. sampled all non-soft harmonic phonons at the Γ point using a Monte Carlo technique,⁹¹ finding significant differences with the standard perturbation theory results. Electron-phonon interactions can be calculated with MD, but as with phonon-phonon scattering, achieving convergence with respect to electronic (k -point sampling and basis set) and vibrational (q -point sampling and supercell size), while maintaining sufficient integration time to capture rare processes, is costly.

Recently a ‘one shot’ method has been developed to calculate band-gap renormalization and phonon-assisted optical absorption, and applied to Si and GaAs.¹¹³ Nuclei positions are carefully chosen as a representative sample from the thermodynamic ensemble, and the electronic structure is needed for this static structure only—a significant increase in computational efficiency. Such techniques may provide a promising method to calculate the electron-phonon coupling of complex materials, but so-far are only valid in the harmonic phonon approximation. They have not yet been tested for the family of hybrid halide perovskites or other more complicated crystal structures.

2.3.3 Charge carrier transport

We now consider some aspects of charge carrier transport in hybrid halide perovskites. The minority-carrier diffusion length is the average length a photo-excited (or electronically-injected) carrier travels before recombining. In a photovoltaic device, the diffusion length must be sufficient to reach the contacts. The minority-carrier diffusion length is a product of the diffusivity D and lifetime τ of minority charge carriers, $L_d = \sqrt{D\tau}$.

Minority-carrier diffusion lengths in MAPI are reported to be considerably larger than other solution processed semiconductors.¹¹⁴ Long lifetimes (large τ) can be partly attributed to the ‘defect-tolerance’ of hybrid perovskites (discussed in Section 2.4.3), reducing the rate of ionised-impurity scattering and non-radiative recombination.

The effective mass of both electrons and holes in hybrid halide perovskites is small (though careful calculations including spin-orbit coupling indicate that the band extrema do not show a parabolic dispersion relation, and so the concept of effective mass is ill defined in these materials¹⁰⁷). Given the effective mass of $< 0.2m_e$, the carrier mobility of MAPI ($< 100 \text{ cm}^2\text{V}^{-1}\text{s}^{-1}$) is modest in comparison to conventional semiconductors such as Si or GaAs ($> 1000 \text{ cm}^2\text{V}^{-1}\text{s}^{-1}$).⁵² Carrier mobility must be limited by strong scattering.

Low temperature mobility in this material reduces as a function of temperature as $T^{-1.5}$, which provides circumstantial evidence for being limited by acoustic phonon scattering.^{115,116} However, if we only consider acoustic phonon scattering (which is elastic due to the population of acoustic modes), the calculated mobility is orders of magnitude larger than experiment. A key realisation is that the soft nature of these semiconductors results in optical phonon modes (see Figure 2.2) below thermal energy.^{64,108} Optical phonon scattering is inelastic and dominates once the charge carriers have sufficient energy to generate the phonon modes¹¹⁷. Through solving the Boltzmann transport equation parameterised by DFT calculations, at room temperature the scattering from longitudinal optical phonons is most relevant in limiting mobility.^{118,119}

Mobility will be further limited by scattering from point and extended lattice defects.¹²⁰ Fluctuations in electrostatic potential resulting from dynamic disorder provide a macroscopic structure from which carriers will also scatter.^{88,121}

2.4 Photophysics and solar cells

Recent research interest in hybrid halide perovskites is mainly due to their use as the active layer in efficient solar cells. There are areas of the underlying physics which are not yet developed, and which may be limiting progress in the field. Ion migration is poorly understood and has been correlated with hysteresis effects^{124,125} and device degradation. Defects which act as recombination centres have not been identified and characterised. Additionally, interfaces have not been optimised for optimal charge carrier extraction. We outline these issues—where theory and simulation have much to contribute—in the following section.

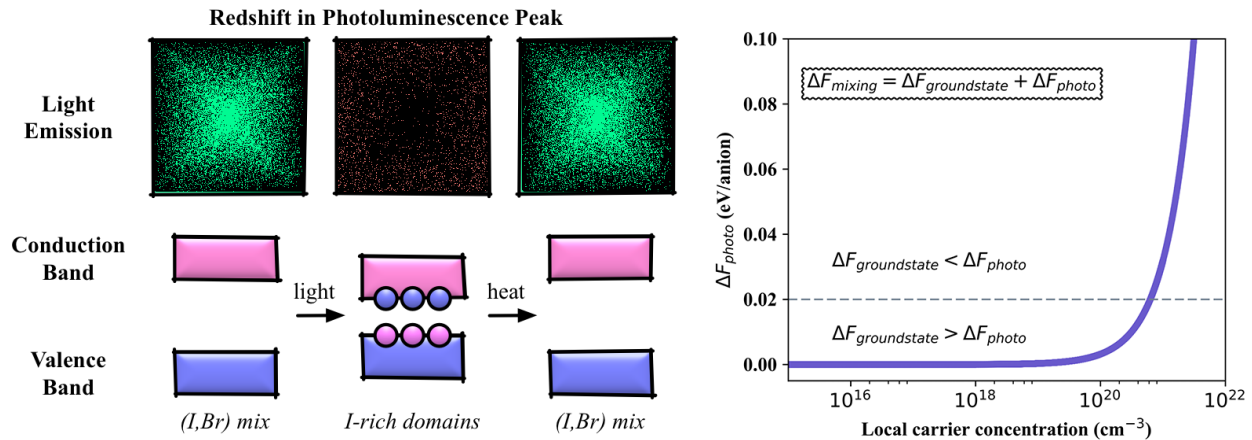


Figure 2.4: Ion transport occurs in halide perovskites: they are mixed ionic-electronic conductors. The vacancy-mediated diffusion of halide anions has been associated with both current-voltage hysteresis of solar cells and the rapid interchange between iodide, bromide and chloride materials. One point of controversy remains the reversible ion segregation observed in mixed (Br,I) systems. Alloyed materials have been found to phase separate upon illumination, but recover their initial state when the light source is removed. The phase separation is associated with a striking red-shift in photoluminescence spectra. A statistical mechanical analysis of ground-state DFT calculations suggested a large miscibility gap¹²², while the charge carriers generated upon illumination can provide an additional driving force for phase separation.¹²³ The results from a simple thermodynamic model are shown in the right panel, where the free energy of mixing contains contributions from the ground-state with an additional component due to the difference in band-gaps between the mixed (I,Br) and phase separated I-rich phases. The latter contribution requires local carrier concentrations approaching 10^{21} cm^{-3} to make a substantial contribution to the overall mixing energy. Figure prepared by Aron Walsh

2.4.1 Ion migration

Charged point defects in the bulk allow for mass transport of ions and can result in spatial fluctuations of electrostatic potential. For solid-state diffusion to be appreciable in magnitude, there needs to be a high concentration of defects and a low activation energy for diffusion.

The equilibrium concentration of charged vacancy defects is calculated as being in excess of 0.4% at room temperature in MAPI.¹²⁶ Low defect formation energies and free-carrier concentrations found across the halide hybrid perovskites indicate that Schottky defects are prevalent across this family of materials. While each point defect is charged, they are formed in neutral combinations so that a high concentration of lattice vacancies does not require a high concentrations of electrons or holes to provide charge compensation.

The ion migration rate is given by:

$$\Gamma = \nu \exp\left(\frac{-\Delta H^{diff}}{k_B T}\right) \quad (2.2)$$

where ΔH^{diff} is the activation energy for solid-state diffusion, and ν is the attempt frequency. In MAPI the diffusion of methylammonium cations, iodide anions and protons have been considered in the literature. Activation energies calculated from first principles show that the

predominant mechanism for ion migration is the vacancy assisted hopping of iodide ions.¹²⁴ This has been confirmed using string simulations¹²⁷ which, like the nudged elastic band method, calculate minimum energy paths and from this infer transition rates.

Based on a bulk activation energy of 0.58 eV¹²⁴, a rate of 733 hops per second would be expected at T = 300 K, with an associated diffusion coefficient of $10^{-12}\text{cm}^{-2}\text{s}^{-1}$. Effective activation energies as low as 0.1 eV have been reported experimentally,^{128,129} which likely correspond to diffusion along extended defects (dislocations, grain boundaries, surfaces)^{130,131}. The corresponding diffusion rate of $10^{-5}\text{cm}^{-2}\text{s}^{-1}$ is very fast, but comparable to surface diffusion of iodine observed in other compounds.¹³²

Modelling ion diffusion at device scales is not yet possible with *ab-initio* methods. Parametrised drift-diffusion modelling of ion and electron density indicate that slow moving ions can explain the slow device hysteresis.^{125,133} A vacancy diffusion coefficient of the order of $10^{-12}\text{cm}^2\text{s}^{-1}$ is consistent with both predictions and transient measurements.¹²⁴

It has been suggested that ion migration within mixed-halide compositions is the result of a non-equilibrium process induced by photo-excitation. X-ray diffraction measurements by Hoke et al.¹³⁴ show that under illumination the mixed halide perovskite $\text{MAPb}(\text{I}_{1-x}\text{Br}_x)_3$ segregates into two crystalline phases: one iodide-rich and the other bromide-rich. This segregation leads to reduced photovoltaic performance via charge carrier trapping at the iodide-rich regions. In some reports, after a few minutes in the dark the initial single phase XRD patterns are recovered. This reversible process is unusual and defies the common assumption made that ion and electron transport are decoupled.

A schematic outlining the phase segregation process is shown in Figure 2.4. A phase diagram constructed from first-principles thermodynamics found a miscibility gap for a range of stoichiometries at room temperature.¹²² This suggests that a mixed-halide material is metastable and will phase segregate after being excited by light, which follow a decreasing free energy gradient towards halide-rich areas formed prior to light excitation (such as grain boundaries). The accumulation of charge carriers increases lattice strain and drives further halide segregation. Our calculations indicate that the transition between mixing and segregation will occur at a local carrier concentration of 10^{21} cm^{-3} , which would require accumulation into small regions of the material.

2.4.2 Electron-hole recombination

The open-circuit voltage (V_{OC}) of a solar cell is determined by the rate of charge carrier recombination in the material, as no photogenerated charges are being extracted and so all are recombining. When operated to generate power, the rate of recombination competes with the rate of charge extraction, limiting the fill factor of the solar cell. Combined, rates of recombination specify the photovoltaic potential of a material.

Recombination is usually separated into three channels: non-radiative; radiative; and Auger. These respectively correspond to: one; two; and three electron processes. Assuming that the prefactors for the rates of these processes are constant, the carrier density in an intrinsic semiconductor can be modelled as a rate equation:

$$\frac{dn}{dt} = G - nA - n^2B - n^3C \quad (2.3)$$

where G is the rate of electron-hole generation.

While non-radiative recombination is limiting in many inorganic thin-film technologies, hybrid perovskites are not significantly affected. This is surprising for the high density of defects expected for a material processed from solution, leading to them being described as ‘defect tolerant’.¹³⁵

Radiative (bimolecular) recombination is slower than would be expected for a direct band-gap semiconductor. Recent calculations^{136,137} revealed how relativistic Rashba splitting can suppress radiative recombination at an illumination intensity relevant to an operating solar cell. After photoexcitation, electrons thermalise to Rashba pockets in the conduction band minima away from the high symmetry point in reciprocal space. This leads to an indirect charge recombination pathway as the overlap in k -space between occupied states near upper valence and lower conduction bands diminishes. It has also been suggested that direct recombination is suppressed due to the pockets of minima being spin-protected.¹³⁷ Direct gap radiative recombination is reduced by a factor of 350 at solar fluences, as electrons must thermally repopulate back to the direct gap.¹³⁶ This is in agreement with the temperature-dependence of the bimolecular rate measured experimentally⁷⁴ and calls into question the validity of models where a global radiative recombination rate independent of carrier concentration is used.

Auger recombination is only significant at fluences well above solar radiation, but is important for understanding laser photophysics.

Ferroelectric effects could contribute to electron-hole separation due to electrostatic potential fluctuations in real space. Although the molecular cation plays no direct role in charge generation or separation it could have a part to play in charge transport through the formation of polar domains.^{121,138} Macroscopic ferroelectric order is not necessary to explain device behaviour in a 3D drift-diffusion simulation.¹³⁹ A multiscale Monte Carlo code based on a model Hamiltonian parameterized for the inter-molecular dipole interaction in MAPI, explored the results of this dynamic polarisation.⁸⁸ This predicts the formation of antiferroelectric domains which minimise energy via dipole-dipole interaction, which work against a cage-strain term preferring ferroelectric alignment.⁸¹ This provides electrostatically preferred pathways for electrons and holes to conduct. Developing more accurate models and measurements of the nature and effects of lattice polarisation in these materials is the subject of on-going research efforts.

Table 2.1: The first shallow donor defect level in MAPI, Si and CdTe calculated from effective mass theory using Equation 2.4. The dielectric constant ϵ_0 can be considered an important descriptor for photovoltaic materials as several important properties (e.g. rate of impurity scattering) scale with its square.

Material	$\frac{m^*}{m_0}$	ϵ_0	$E_1(\text{meV})$
MAPI	0.15 ¹³⁸	25.7 ¹³⁸	3
Si	0.45 ¹⁴⁵	11.7 ¹⁴⁵	45
CdTe	0.11 ¹⁴⁶	10.2 ¹⁰³	14

2.4.3 Defect levels in the band-gap

To understand why the rate of non-radiative recombination is low we consider the known defect properties of hybrid perovskites. Defects appear to have a minimal impact upon charge carrier mobility and lifetime,¹⁴⁰ which can be attributed to a combination of large dielectric constants and weak heteropolar bonding.

Under the Shockley-Read-Hall model for semiconductor statistics non-radiative recombination is mediated through deep defect states in the gap.¹⁴¹ Shallow defect states can act as traps but the carriers are thermally released to the band before recombination can occur. Hybrid perovskites—with high dielectric constant and low effective mass—show a tendency towards benign shallow defects under the hydrogenic model:¹⁴²

$$E_n = -\frac{m^*}{m_0} \frac{1}{2n^2\epsilon_0^2} \quad (2.4)$$

where $\frac{m^*}{m_0}$ is the effective mass ratio, ϵ_0 is the static dielectric constant and n is an integer quantum number for given energy level. Atomic units are used and so energy is given in Hartrees.

In Table 2.1 we give the first hydrogenic defect level for MAPI, Si and CdTe, where the binding energy for MAPI is only 3 meV. For ionic materials, one would expect a large central cell correction that could result in much deeper levels, for example, as seen for the colour centres in alkali halides.¹⁴³ It was shown numerically that the on-site electrostatic potentials in the I-II-VII₃ perovskites are relatively weak owing to the small charge of the ions (e.g. Cs⁺Pb²⁺I₃⁻) compared to other perovskite types (e.g. Sr²⁺Ti⁴⁺O₃²⁻),¹⁴⁴ which would also support more shallow levels. In addition, arguments based on covalency have also been proposed.¹⁴⁰

2.4.4 Beyond the bulk: surfaces, grain boundaries and interfaces

As perovskite solar cells approach commercial viability,⁵⁴ there are considerations to be made beyond the bulk materials. Surfaces, grain boundaries and interfaces will influence device performance and long-term stability, and become increasingly important as the science is scaled up from lab to production line. Accurate interface modelling requires consideration of halide migration, ion accumulation, charge carrier transport and charge carrier recombination at the

defect states. There has been preliminary work, that provides insights, but real systems offer much deeper complexity.

Perovskite films fabricated through solution processing methods are multicrystalline and so the formation of grain boundaries is inevitable. The resulting microstructure provides pathways for ion conduction, electron-hole separation and recombination. The shallow traps introduced are evidenced through improved device performance with increasing grain size¹⁴⁷ and their thermal activation. Initial calculations suggest that grain boundaries do not introduce deep defects and consequently have negligible effect upon the rate of non-radiative recombination.¹⁴⁸ This is in conflict with spatially resolved photoluminescence¹⁴⁹ and cathodoluminescence¹⁵⁰ measurements which evidence greater non-radiative loss at grain boundaries.

Recent calculations using nonadiabatic MD and time-domain density DFT¹⁵¹ indicate that grain boundaries localize the electron and hole wavefunctions and provide additional phonon modes. This leads to increased electron-phonon coupling which in turn will give a higher rate of non-radiative recombination.

The typical device structure for a perovskite cell is the perovskite absorber layer sandwiched between an electron transport layer (e.g. TiO₂, SnO) and hole transport layer (e.g. spiro-OMeTAD, PEDOT-PSS). At the interface there are two key considerations. One is that the bands should be electronically matched so as to allow efficient charge extraction without large energy loss. The second is that the formation of defects should be minimised as these acts as sites for recombination, can lead to mechanical degradation of the device and have been linked to hysteresis.¹⁵²

The commonly used hole transporter spiro-OMeTAD is hygroscopic so that stability in humid air is a concern.¹⁵³ This has prompted the development of screening procedures^{154,155} to identify alternative contacts. The electronic-lattice-site (ELS) figure of merit considers band alignment, lattice match and chemical viability via the overlap of atomic positions.¹⁵⁴ Using this figure of merit Cu₂O and is identified as a possible earth abundant hole extractor, whilst oxide perovskites such as SrTiO₃ and NaNbO₃ have been identified as possible electron extractors. As with the majority of screening techniques, the candidate materials meet the necessary but perhaps not sufficient conditions. Further refinements may consider the change in electronic properties as lattice strain and chemical inhomogeneity at the interface is introduced.

2.5 Summary

We have outlined the physical properties that make hybrid perovskites unique semiconductors, but also challenging for contemporary theory and simulation. A number of practical points relating to issues we have encountered whilst running simulations of these materials are summarized in Table 2.2. The volume of work in this area has not allowed us to address all active areas of research, including that around perovskite-like structures with lower dimensionality (e.g.

Table 2.2: A collection of common issues that can arise in the simulation of hybrid perovskites.

Technique	Symptom	Solution
Crystal structure optimisation	Partial occupancy in structure files	Test different configurations and check total energy
Crystal structure optimisation	Missing H in structure files	Include H based on chemical knowledge and electron counting
Crystal structure optimisation	Slow ionic convergence	Try changing algorithm type and settings
Electronic structure	Bandgap is too large	Include spin-orbit coupling and consider excitonic effects
Electronic structure	Bandgap is too small	Use a more sophisticated exchange-correlation functional
Electronic structure	Bandgap is still too small	Try breaking symmetry, especially for cubic perovskites
Electronic structure	Workfunction is positive	Align to external vacuum level using a non-polar surface
Supercell convergence	Unusual convergence behaviour	Use only even cell expansions (e.g. $2 \times 2 \times 2$)
Ab initio thermodynamics	No stable chemical potential range	No easy fix (many hybrid materials are metastable)
Berry phase polarisation	Spontaneous polarisation is too large	Use appropriate reference structure and pathway
Point defects	Negative formation energies	Check for balanced chemical reaction and chemical potential limits
Point defects	Transition levels are deep in band-gap	Check supercell expansion and charged defect corrections
Alloyed systems	Many possible configurations	Use appropriate statistical mechanics
Lattice dynamics	Many imaginary phonon modes	Check supercell size and force convergence
Lattice dynamics	Imaginary modes at zone boundaries	Use mode-following to map out potential energy surface
Molecular dynamics	System melts or decomposes	Check k -points and basis set convergence
Molecular dynamics	Unphysical dynamics	Check equilibration and supercell expansion
Molecular dynamics	No tilting observed	Use an even supercell expansion
Electron-phonon coupling	Values far from experiment	Consider anharmonic terms beyond linear response theory
Drift-diffusion model	Current-voltage behaviour incorrect	Consider role of fluctuating ions and electrostatic potentials

Ruddleston-Popper phases)^{53,156,157} and double perovskites with pairwise substitutions on the B site,^{67,68,158,159} which are both attracting significant interest.

The properties of hybrid halide perovskites which provide difficulties for modelling are also those which make them successful solar energy materials. Strong electronic-ionic coupling means that the approximation of a single static lattice is poor when calculating ground state electronic properties. Harmonic approximations may also be invalid due to anharmonicity introduced by rotational disorder. However, it is this coupling which allows charge screening, producing a defect tolerant material. It also facilitates fast charge separation and suppression of excitonic states. The facile formation of Schottky-like charged vacancy defects mediates the transport of halide ions—dynamic behaviour which can be only fully captured using multi-scale modelling. However, it is these defects which ensure a low free carrier background concentration which is necessary for high efficiencies in a p-i-n architecture. Attempts are now being made to distill this understanding into descriptors for the large-scale screening of novel, earth-abundant, non-toxic semiconductors.^{44,140}

Acknowledgements

The primary research underpinning this chapter was performed by Jarvist M. Frost (molecular dynamic and Monte Carlo investigations), Federico Brivio (crystal and electronic structure), Jonathan M. Skelton (lattice dynamics and vibrational spectroscopy), and Lucy Whalley (band-gap deformations). This work was funded by the EPSRC (grant numbers EP/L01551X/1 and EP/K016288/1), the Royal Society, and the ERC (grant no. 277757).

It's simple mathematics.

— Mos Def, *Mathematics*

3

Theory and methodology

3.1 Introduction

In this chapter I present the theory and methodology that underlies the work in this thesis. The chapter starts with an introduction to Density Functional Theory - first I introduce the theoretical concepts, then I provide details about how DFT is implemented in practice. In the second part of the chapter I outline how we can use DFT energies combined with a number of post-processing steps to predict defect formation energies and charge transition levels. The chapter ends with an introduction to the theory of lattice dynamics and how this is used to calculate the vibrational properties of a material.

3.2 Density Functional Theory

Density Functional Theory is the most commonly used method of electronic structure calculation in condensed matter physics and quantum chemistry. Using DFT we are able to predict the ground state properties of a material including electron density, total energy, equilibrium structure, vibrational frequencies and properties relating to the difference in total energies, such as defect formation energies or surface energies. As DFT is a ground state theory, we are not able to calculate properties relating to excited states and, without further calculations (such as those outlined in Section 3.4), results do not incorporate the effects of temperature.

The theoretical basis for DFT was established in 1964 through the work of Walter Kohn and Pierre Hohenberg.¹⁶⁰ This was further developed by Walter Kohn and Lu Jeu Sham to produce Kohn-Sham DFT.¹⁶¹ However it was not until the late 1980's that work started on building approximations to the exchange-correlation functional so that DFT could be used in practice.

There are a growing number of codes that implement DFT, many of which include extensions to DFT so that excited state properties can be predicted. Although some codes aspire to a blackbox approach, with the user protected from the underlying mechanics of DFT, for most systems of interest an understanding of the underlying approximations and parameters used are required for reliable results.

3.2.1 Basic concepts

Firstly, a note on the name. A function accepts one or more numbers as input and produces a number as output. Likewise, a functional accepts one or more *functions* as inputs, and produces a number as output. In DFT the functional is the electron density which is a function of space and time.

Throughout this chapter, unless stated otherwise, we use the Born-Oppenheimer approximation: the heavy atomic nuclei are treated as fixed points, and we solve the ground state quantum mechanical problem for the electrons only. This reduces the number of degrees of freedom of the system, a tactic that will be used again later in the chapter.

Although no one single text is followed, concepts for the underlying theory have been taken from References [162], [163] and [164].

The Schrödinger equation

The Schrödinger equation describes the wavefunction Ψ of a quantum mechanical system. The wavefunction is a fundamental postulate of quantum mechanics and it contains all the information for a given system. Once the Schrödinger equation is solved, and a wavefunction is found, all the physical properties for that system follow. To take the simplest possible example, the time-independent non-relativistic Schrödinger equation for a single particle can be written as:

$$\left[\frac{-\hbar^2}{2m} \nabla^2 + V(\mathbf{r}) \right] \Psi(\mathbf{r}) = E\Psi(\mathbf{r}) \quad (3.1)$$

where the first term in the bracket corresponds to the kinetic energy and the second term corresponds to the potential energy. For a single particle in a simple potential, such as the “particle in a box” system or hydrogen atom, the Schrödinger equation can be solved exactly. Unfortunately it is not possible to solve the Schrödinger equation exactly for more complex systems, where there are multiple electrons interacting with each other (N-body or many-body systems). In this case, the Schrödinger equation takes the form:

$$\left[\frac{-\hbar^2}{2m} \sum_{i=1}^N \nabla_i^2 + \sum_{i=1}^N v_{\text{ext}}(\mathbf{r}_i) + \sum_{i < j}^N \frac{q_i q_j}{|\mathbf{r}_i - \mathbf{r}_j|} \right] \Psi(\mathbf{r}_i) = E\Psi(\mathbf{r}_i), \quad (3.2)$$

where the third term in the square bracket describes the electrostatic interaction between two particles of charges q_i and q_j , and couples the coordinates of the particles together.

The following methods (Hartree-Fock and Kohn-Sham DFT) give a way to obtain an approximate solution to the Schrödinger equation for systems of interest. They do this by mapping the interacting problem onto a non-interacting problem with an effective potential $V_s(\mathbf{r})$. In doing so, the dimensionality of the problem is greatly reduced. Instead of solving one N -dimensional probelem, which is computationally intractable, N one-dimensional problems are solved (Figure 3.3). These provide a compromise between accuracy and computational efficiency.

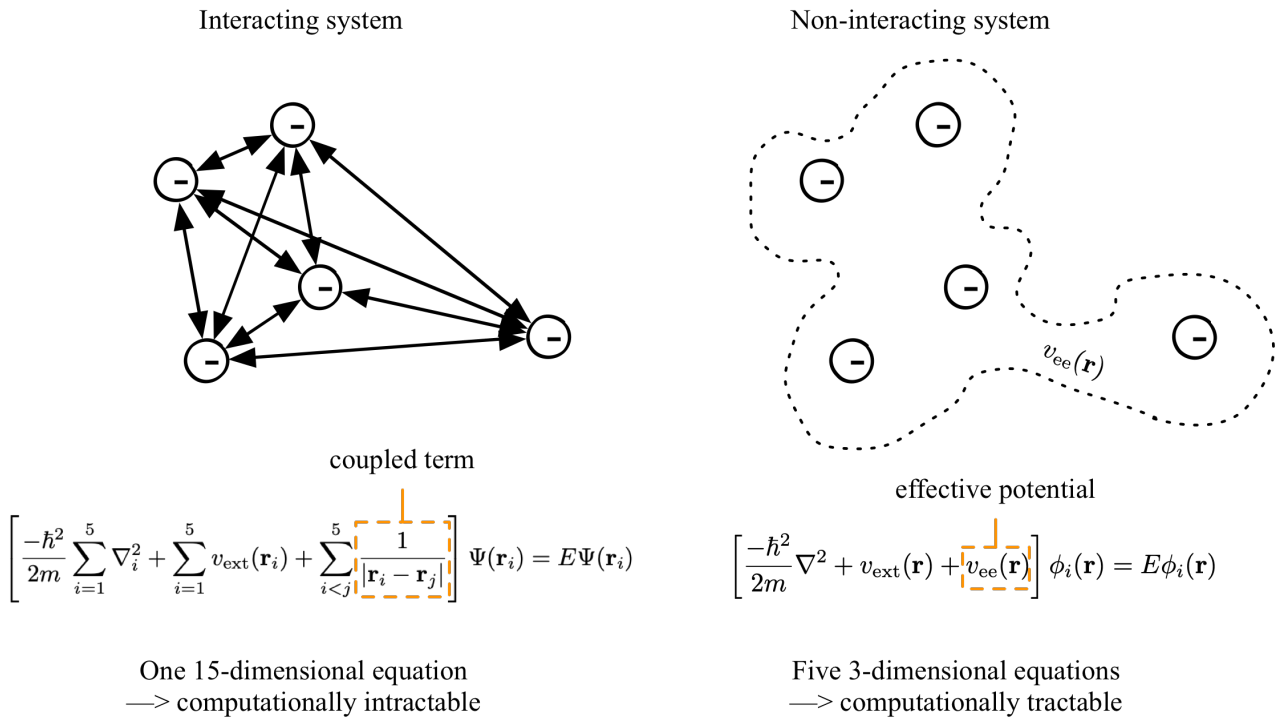


Figure 3.1: Schematic outlining the equivalence between a system of interacting particles and a system of non-interacting particles in an effective potential. The underlying idea is that an interaction can be replaced by the equivalent potential. This maps the interacting $3N$ -dimensional problem onto N 3-dimensional problems. A consequence of this mapping is that the effective potential depends on the electron density which is itself dependant on the effective potential - a self-consistent set of equations is formed.

Hartree-Fock methods

Hartree-Fock methods introduced the concept of fictitious one-electron orbitals ϕ that do not interact with each other as a way of solving the Schrödinger equation. The HF many-body wavefunction is a Slater determinant of the one-electron orbitals and is denoted with Φ .

The effective potential, introduced in Figure 3.3, is given by $V_{\text{ee}} = U + E_x$. U accounts for the electrostatic interaction between electrons. Hartree-Fock methods model the charge interaction as a coulomb potential for a system of fixed electrons; the electrons feel the average electrostatic field due to the other electrons.

The second way electrons interact with each other is via their spin:

Two MCs can't occupy the same space at the same time, it's against the laws of physics

—Lauryn Hill, *Zealots*

Electrons with the same spin are indistinguishable, and a consequence of this is that the many body wavefunction must be anti-symmetric. This leads to the Pauli Exclusion Principle, whereby two identical electrons (ie, electrons with the same spin and momentum) cannot occupy the same space at the same time. Hartree Fock methods account for electron exchange, the repulsion between electrons with parallel spins, exactly.

Hartree-Fock methods do not give an exact solution to the Schrödinger equation as they ignore electron correlation. This is the correlated motion of electrons with anti-parallel spins as a result of their mutual coulombic repulsion. It is a consequence of the fact that the true many body wavefunction is not formed from a simple Slater determinant.

The Hohenberg-Kohn theorems

The 1964 Hohenberg-Kohn paper contains two key results: (i) the ground state electron density uniquely determines the ground state electronic wave function and, following this, all properties of the system; (ii) the true density functional for the electronic energy assumes its minimum for the correct ground-state density.

In Hartree-Fock methods, the potentials (external, coulomb and exchange) determine the properties of a system. First, Hohenberg and Kohn demonstrate that the density can be used instead to uniquely characterise the system; rather than solving the Schrödinger equation for the wavefunction, we can solve it for the electron density. The energy can be expressed as

$$E[\rho] = \int v_{\text{ext}}(\mathbf{r})\rho(\mathbf{r})d\mathbf{r} + T[\rho] + J[\rho] + E_{\text{xc}}[\rho].$$

For a fixed number of electrons the functional $F[\rho] = T[\rho] + J[\rho] + E_{\text{xc}}[\rho]$ is universal, and the only thing that varies between systems is the external potential (determined by the electron-nuclei interaction).

Secondly, Hohenberg and Kohn show that the ground state energy can be found variationally; the density that minimises the total energy is the true ground state density.

This formalism has the advantage that the electron density has a lower dimensionality than the N-electron wavefunction (Figure ??). The problem is that although the Hohenberg-Kohn theorem tells us that the terms $T[\rho]$ and $E_{\text{xc}}[\rho]$ exist, they are unknown and must be approximated.

The Kohn-Sham theorem

The Kohn-Sham theorem shows the for any interacting system with ground state density $\rho(\mathbf{r})$ there exists a non-interacting system with the same ground-state $\rho(\mathbf{r})$. To find the ground state energy of the real interacting system, the occupation numbers of *fictitious*, non-interacting

Task: describe two electrons on a 2x2 mesh of points

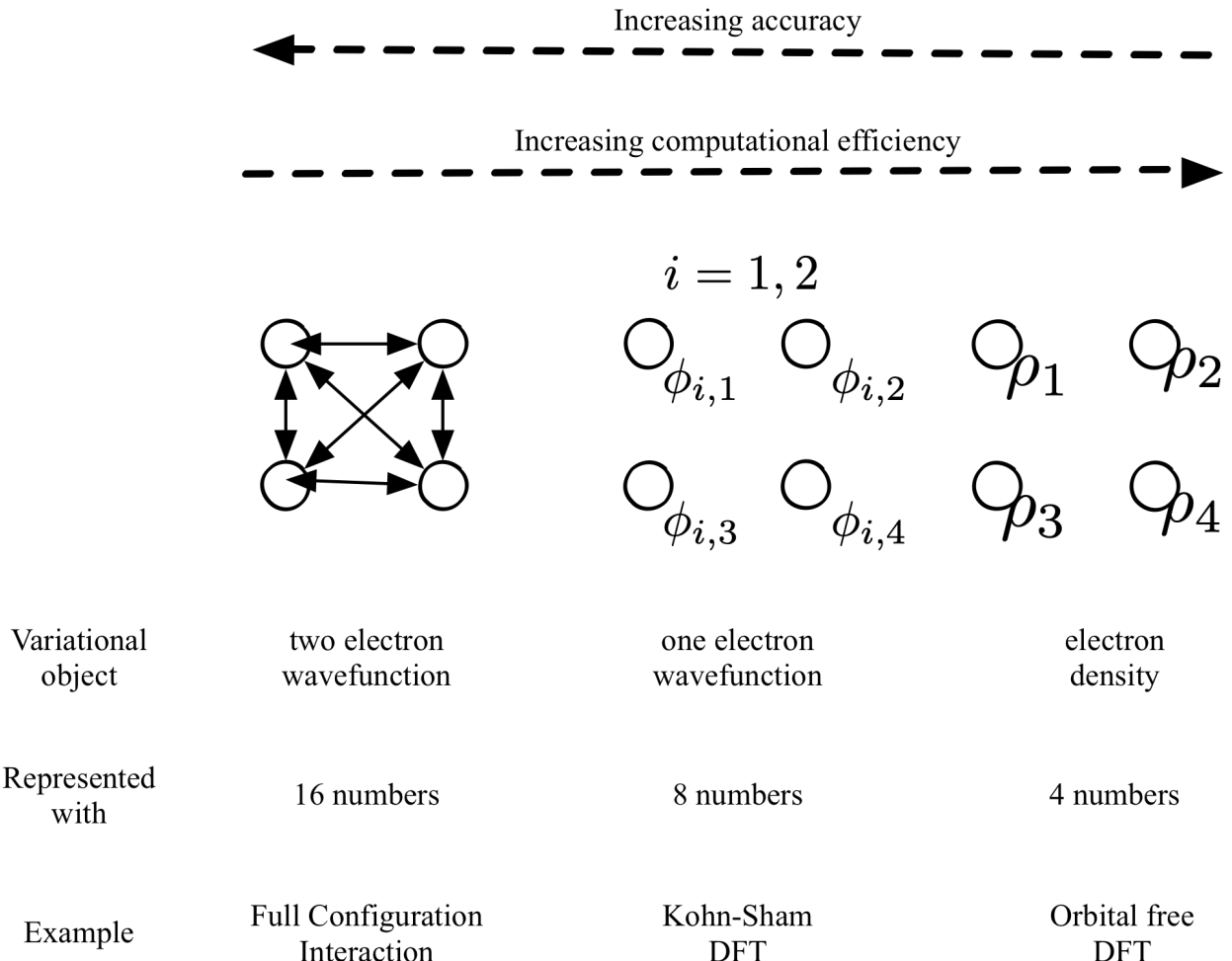


Figure 3.2: To solve the Schrödinger equation we can use a variational object with lower dimensionality and higher computational efficiency, although this will come at the cost of accuracy. This schematic is based on a discussion in Walter Kohn's Nobel Prize lecture.¹⁶⁵

one-electron orbitals can be optimised. For a non-interacting system we know how to calculate $T[\rho]$ and this provides a good approximation to the true kinetic energy, so the Kohn-Sham theorem provide a more practical way to apply DFT. However, the exchange-correlation density functional $E_{xc}[\rho]$ is still not known. Only approximations to this functional can be made, leading to approximations for the electronic density, total energy and other system properties.

3.2.2 DFT in practice

Exchange-correlation functionals

To use Kohn-Sham DFT we must approximate the exchange-correlation functional, and there is a growing list of functionals with varying levels of complexity. A useful way of categorising these

functionals, "Jacob's Ladder", has been proposed by John Perdew (Figure ??). As a general rule, more accurate functionals are constructed by adding more parameters and variables.

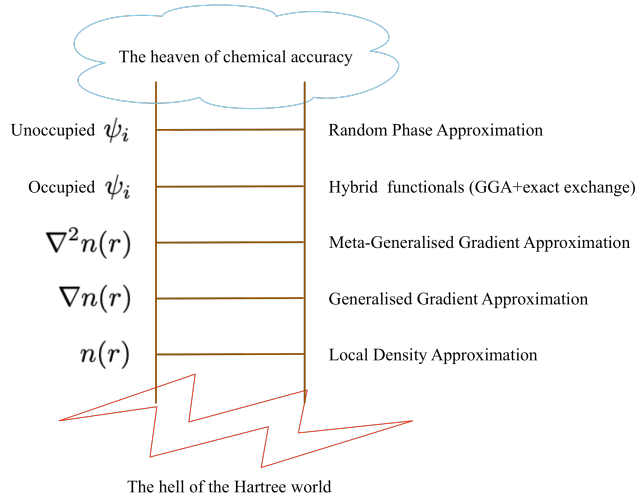


Figure 3.3: Jacob's ladder of exchange correlation functionals. On the right hand side are the various categories of exchange-correlation functionals and on the left hand side are the additional input variables included at each level of theory. As we move up the ladder the chemical accuracy increases, alongside computational expense.

Local Density Approximation

At the lowest rung of the ladder is the local density approximation. In this approximation, only one variable is used to calculate the exchange correlation energy. This is the charge density for an infinitesimal 3-dimensional volume element. The exchange energy is calculated exactly

$$E_{\text{LDA,x}}[n] = -\frac{3}{4} \left(\frac{3}{\pi}\right)^{\frac{1}{3}} n^{\frac{4}{3}}(\mathbf{r}) d\mathbf{r},$$

and the correlation energy is calculated numerically by fitting to many-body quantum monte carlo studies for an inhomogeneous electron gas. Strictly, the LDA should only be used for slowly varying densities, however it has performed surprisingly well for predicting the properties of a variety of atoms, solids and molecules. This is due to a cancellation of errors: LDA underestimates the exchange energy and overestimates the correlation energy. However there is a tendency for LDA to overestimate the binding energy and underestimate lattice parameters. This is a particularly pronounced problem in weakly bonded systems. Common LDA functionals include VWN and PW92.

Generalised Gradient Approximation

At the next level of theory, two variables are used to determine the exchange-correlation energy: charge density and the density gradient. GGAs are semi-local functions due to their dependence on the gradient. The parameters of GGA functionals can be derived from physical constraints (non-empirical, as in the widely used PBE functional), or obtained from fitting procedures (empirical, as in the case of B88). GGAs improve the over-binding of LDA, but tend to underestimate the band gap of the material.

Meta-GGA

Meta-GGAs extend the GGA functional to include the non-interacting kinetic energy density as an input to the functional. This is calculated from the laplacian of the occupied electron orbitals. A common meta-GGA functional is TPSS.

Hybrid functionals

On the fourth rung, hybrid functionals combine GGA functionals with a proportion of the exact HF exchange energy. The simplest hybrid functional takes the form

$$E_{\text{hybrid,xc}}[n] = \alpha E_{\text{exact,x}} + (1 - \alpha) E_{\text{GGA,xc}}$$

In some studies, the proportion of exact exchange is tuned to reproduce the property of interest correctly. For example, $\alpha = 0.25$ is commonly used to correctly reproduce the band gap of the hybrid halide perovskite MAPI. In DFT each electron interacts with itself as the potential derives from the total charge density of the system. This error is particularly pronounced for localised states, for example after the trapping of an electron or hole. By including a proportion of exact HF exchange hybrid functionals correct the self-interaction error and improve the accuracy of predictions.

Random Phase Approximation

Closest to heaven is the Random Phase Approximation (RPA), which uses all of the Kohn-Sham orbitals (occupied and unoccupied) as input. Previous approaches fail when there are significant long range effects, as they have no information about the electron density far from an electron. The RPA is able to correctly predict long-range interactions between non-overlapping electron orbitals, for example van der Waals interactions.

Exploiting symmetry

The material studied in this thesis, $\text{CH}_3\text{NH}_3\text{PbI}_3$, is a crystalline solid. Although we want to understand the properties of a finite piece of material, we use the standard approach which is to model the finite crystal as an infinite crystal. This is acceptable if the crystal piece is large enough so that its properties do not depend on size. We introduce Born-von Karman (periodic) boundary conditions so that the infinite crystal is built from a repeating array of unit cells. For a unit cell of length L , any physically significant function ψ of the crystal must have the same value at the origin and L , or in 3D:

$$\psi([000]) = \psi([L00]) = \psi([0L0]) = \psi([00L]) \quad (3.3)$$

where the square bracket denotes a vector on the basis of the three unit cell vectors (Figure 3.4). Note that there are an infinite number of unit cells of different shapes and sizes that can be used to build an infinite crystal.

It is often the case that translational symmetry is broken in the real material, for example when there are point defects (as in Results chapter ??). Furthermore, lattice vibrations have a periodicity larger than the unit cell (Results chapter ??). To model this phenomena a supercell is built from multiple unit cells and this is used as the basic repeating unit (Figure 3.4).

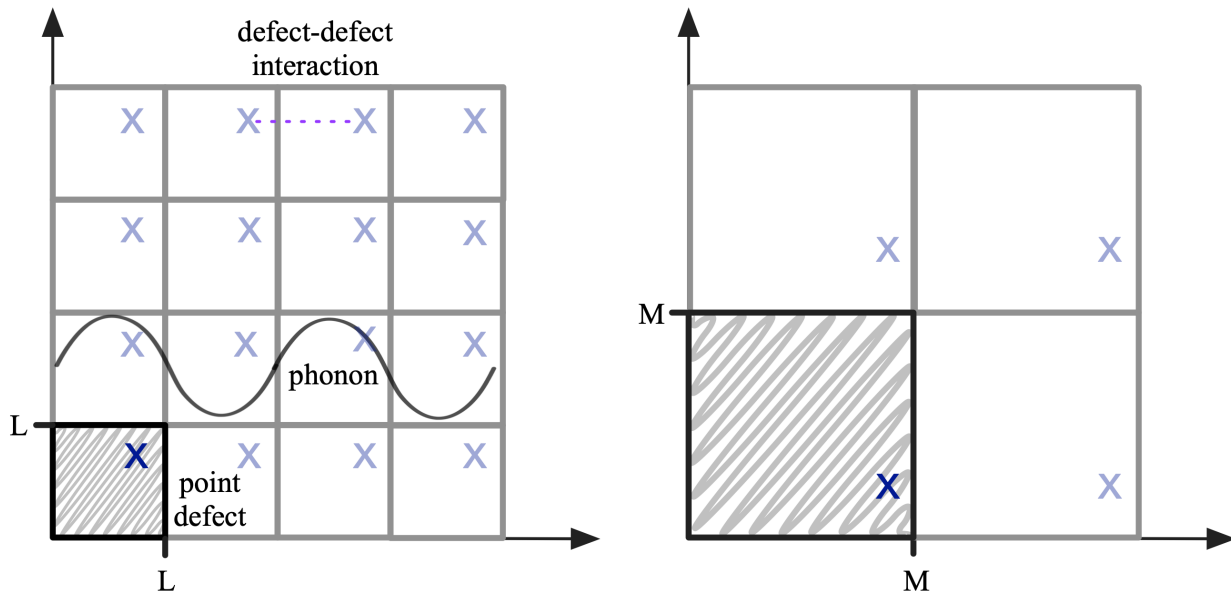


Figure 3.4: An infinite crystal is built from a repeating unit cell of length L (LHS). Point defects (marked with an ‘x’) break translational symmetry in real crystals and care must be taken when modelling these as neighbouring defects can interact with each other in an unphysical way. In addition, vibrational modes can have wavelengths $> L$ (sine wave). A supercell of length $M = 2L$ can be built to better model these effects (RHS).

When the Schrodinger equation is solved for a H atom the solution gives wavefunctions corresponding to the 1s, 2s, 2p, etc orbitals found in chemistry. For periodic systems, wavefunctions are formed by Bloch functions:^{Hoffman1987}

$$\psi_k = u_k e^{i\mathbf{k}\cdot\mathbf{r}} \quad (3.4)$$

where the Bloch function is formed from the product of a basis function u_k with the same periodicity as the crystal lattice, and a plane wave $e^{i\mathbf{k}\cdot\mathbf{r}}$. k is a crystal wave vector which forms a space known as reciprocal space; to understand the physical significance of k we consider an infinite 1D chain of hydrogen atoms separated at distance L (Figure 3.5). The electron states can be described a linear combination of H 1s orbitals u_n centred at each lattice point :

$$\psi_k = \sum_n u_n e^{iknL} \quad (3.5)$$

$k = 0$ corresponds to the low energy most bonding state, and $k = \frac{\pi}{L}$ corresponds to the high energy anti-bonding state

$$\psi_0 = \sum_n u_n e^0 = u_0 + u_1 + u_2 + u_3 \dots \quad (3.6)$$

$$\psi_{\frac{\pi}{L}} = \sum_n u_n e^{i\pi n} = u_0 - u_1 + u_2 - u_3 \dots \quad (3.7)$$

Between these two extremes there is a continuum of states forming an electronic band (Figure 3.5).

Substituting Equation 3.4 into Equation 3.1 gives

$$\left[\frac{1}{2m} \left(\frac{\hbar}{i} \nabla + \hbar k \right)^2 + V(\mathbf{r}) \right] u_k = E(k) u_k \quad (3.8)$$

For any k we can solve Equation 3.8 with periodic boundary conditions to find the bandstructure $E(k)$. The bandstructure is often modelled as being parabolic around the maxima and minima, and the curvature determines the carrier effective mass which is explored in Chapter ???. There are an infinite number of eigenvalues so the energy is labelled $E_n(k)$ where n labels the particular eigenvalue (band). As a result of crystal symmetry, $E_n(k)$ is periodic and only k -vectors within a region of space known as the Brillouin Zone ($|k| < \frac{\pi}{a}$) need to be considered.

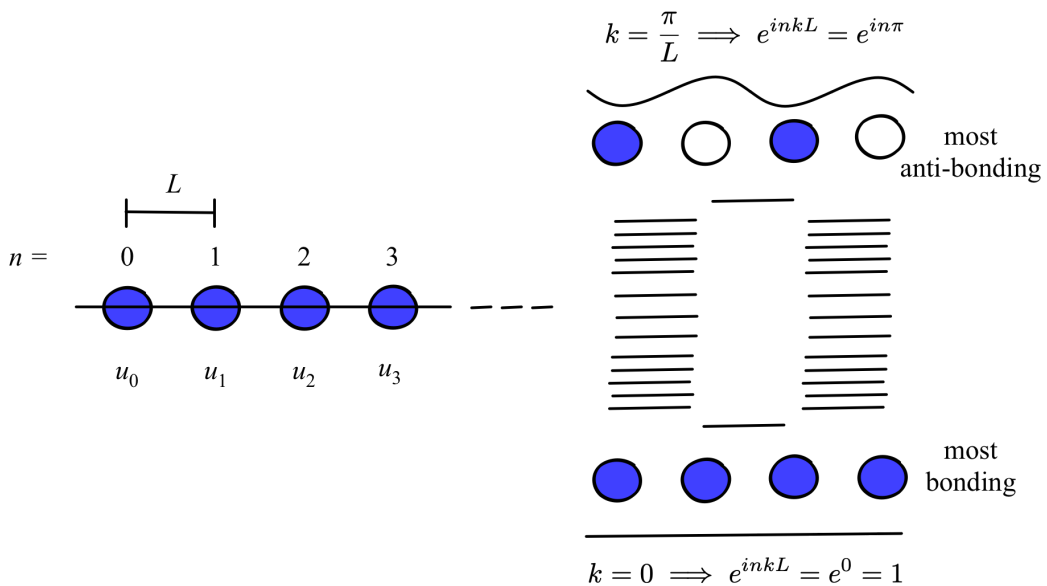


Figure 3.5: A one dimensional infinite lattice where the points are labelled $n = 1, 2, \dots$. The point spacing (unit cell length) is L , and there is a hydrogen 1s orbital (basis function) u_n centred at each point. The electron states for this system are formed from Bloch functions as given in Equation 3.5. $k = 0$ corresponds to a low energy bonding state and $k = \frac{\pi}{L}$ corresponds to a high energy anti-bonding states.

Basis Sets

In the previous example the lattice periodic part of a bloch function took the form of a H 1s orbital. For more complex systems, u_k can itself be expanded into a plane wave basis set whose wave vectors G are reciprocal lattice vectors

$$u_k = \sum_G c_{\mathbf{k},G} e^{i\mathbf{G}\cdot\mathbf{r}}. \quad (3.9)$$

The complete expanded Kohn-Sham wavefunction can be expressed as

$$\psi_k = \sum_G c_{\mathbf{k},G} e^{i(\mathbf{k}+\mathbf{G})\cdot\mathbf{r}} \quad (3.10)$$

A plane wave basis set is often used for extended systems as they are inherently peroidic. The software used for the DFT calculations in this thesis, VASP, uses a plane wave basis set. For DFT calculations applied to localised systems, such as molecules or nanoparticles, localised basis sets such as gaussian orbitals can be used. This is implements in software such as.

Sudden changes in electron density are hard to capture using a plane wave basis set (to take the extreme example, the fourier decomposition of a simple top hat in real space needs requires an infinite summation in reciprocal space). This can be problematic when describing the region around the nucleus where there are strong oscillations in the wavefunctions. However these oscillations are associated with the core electrons which are less important in chemical bonding, and so pseudopotentials - an effective potential without oscillations - can be used. It has been established that for certain systems pseudopotentials are as precise as all-electron calculations.¹⁶⁶

Optimising the atomic and electronic structure

In this section the process of optimising the atomic and electronic structure of a system towards the ground-state (minimum energy) configuration is outlined.

In Section 3.2 (Figure 3.3) we saw that the potential v_{ee} is dependant on electron density ρ , which is itself dependant on v_{ee} . Therefore an iterative approach, the Self Consistent Field method, is used to calculate the ground-state electronic structure (Figure 3.6, dashed section). The initial guess for the density $n(r)$ is given by a superimposition of the atomic charge densities. This is used to calculate the potential and solve the KS equations, which gives a new $n(r)$. This process continues until the convergence criteria is met (most often within an energy tolerance). Various optimisation routines are provided in DFT codes for finding the ground state configuration, including the conjugate gradient scheme, Davidson Scheme and RMM-DIIS.

DFT is also used to find the ground state atomic structure. Structures from X-ray Diffraction Data are used as a starting guess, so that finding the energetic minimum becomes a local optimisation problem. Ions in the systems are displaced (either the internal coordinates of the

unit cell or the unit cell parameters themselves are adjusted) and the electronic structure for that geometry is solved self-consistently. This repeats until the forces on each atom are zero (within a given tolerance, Figure 3.6).

The limits of DFT

Theoretical limitations

In Section 3.2 we outlined the approximations inherent to DFT calculations: the Born-Oppenheimer approximation and the unknown exchange-correlation functional. Higher levels of theory, which incorporate the effects of spin and relativity (e.g. spin-orbit coupling) are included in many DFT implementations. However DFT is still restricted to ground-state properties and higher levels of theory (GW or TDDFT) are required to describe optical excitations, for example. Another inherent limitation is that the KS eigenvalues are artificial; only the ground state electron density and derived properties are correct. In practice, the KS eigenvalues are used to calculate the band gap, although quantitative band gaps often require the use of hybrid functionals which are tuned to give the correct band gap.

Numerical limitations

There is also a different set of approximations that relate to numerical convergence rather than the underlying theory.

First, we have seen that the Kohn-sham wavefunctions are expanded in a basis set. In principle an infinite set may be needed to describe the Kohn-Sham wavefunction; in practice the basis set must be truncated. The kinetic energy operator is given by $-\frac{\hbar^2 \nabla^2}{2m}$. When this is applied to the plane wave Kohn-Sham eigenstates as given in Equation 3.10, we find that the kinetic energy is proportional to $|k + G|^2$; faster oscillations correspond to higher energy. A cutoff energy E_{cut} is defined so that

$$\frac{1}{2}|k + G|^2 < E_{\text{cut}}. \quad (3.11)$$

This cutoff energy must be tested to ensure that the property of interest, most often energy, is converged to within a certain range.

Second, to calculate many properties of interest we need to integrate over the Brillouin Zone. To calculate the total energy of an insulator for example, we use

$$E = \frac{\Omega}{(2\pi)^3} \sum_{\text{occ.}} \int_{\text{BZ}} E(\mathbf{k}) d^3 k \quad (3.12)$$

where Ω is the volume of the Brillouin zone and there is a sum over all occupied bands. In practice we do not know the continuous form for $E(\mathbf{k})$ and so we evaluate Equation 3.12 numerically as a weighted sum over special points in reciprocal space which form a k -point mesh. This is often an equally spaced mesh centred on the Γ -point ($k = (0, 0, 0)$) in reciprocal space. For any given system, the k -point density scales inversely with cell size; if the unit cell

in Figure 3.4 requires a 6×6 k -point grid, the 2×2 supercell requires a 3×3 k -point grid. As with plane waves, there is a balance between accuracy (the higher the number of k -points, the higher the accuracy) and computational expense. An example convergence study is given in Figure 3.7 where a $5 \times 5 \times 5$ k -point grid is required to converge pressure to within 1 kbar and energy to within 0.1 eV in CsSnI₃.

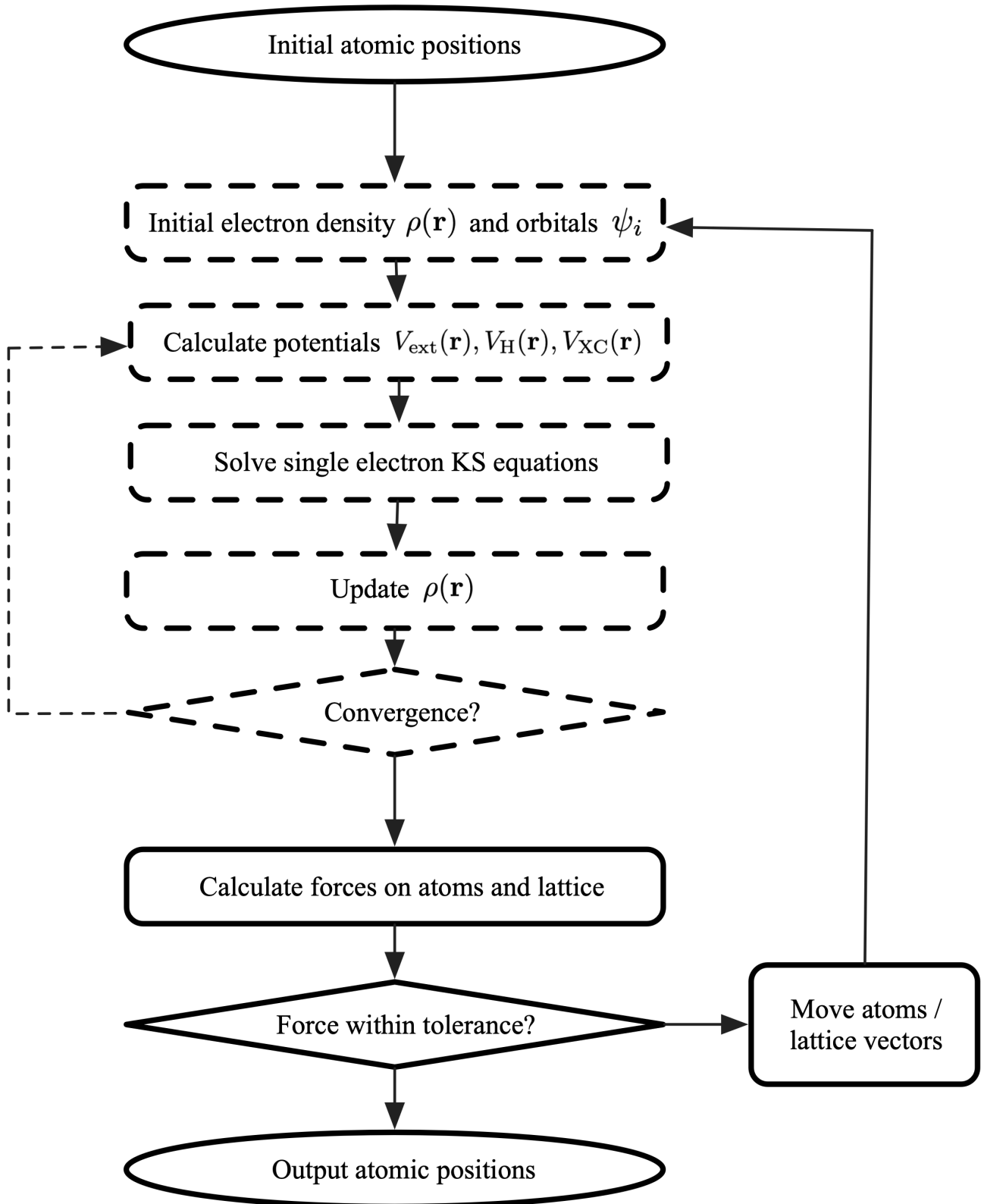


Figure 3.6: Nested iterative method for geometry optimisation. The electronic structure relaxation (dashed lines) is nested within the atomic structure relaxation (solid lines).

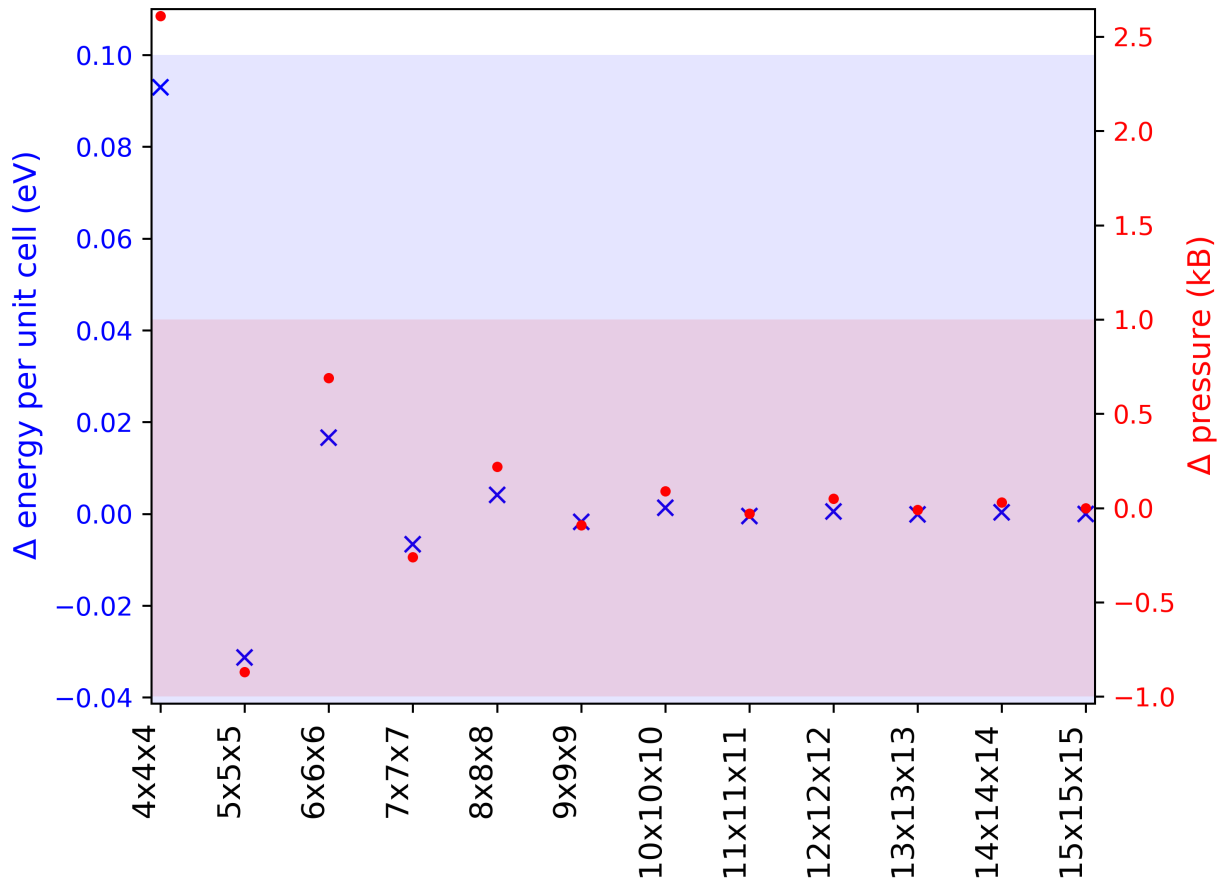


Figure 3.7: k -point convergence of CsSnI_3 . The k -point grid size is on the x -axis. Pressure is denoted with a red dot; the region which is within the 1 kbar convergence criteria for this study is shaded red. Energy is denoted with a blue cross; the region which is within the 0.1 eV convergence criteria is shaded in blue. Only odd grids sample the Γ -point and so there is an oscillation in energy and pressure as we move between odd and even grids.

3.3 Defects in semiconductors

The second law of thermodynamics states that "an isolated system tends towards an equilibrium macrostate with maximum entropy". A consequence of this is that all solids in equilibrium at finite temperature contain point defects, as the cost in lattice energy is balanced by the change in configurational entropy. Point defects are associated with a number of microscopic processes that can be beneficial or detrimental to material performance, including:

- optical: colour centres, up/down conversion
- electrical: conductivity, carrier trapping, ionic hopping
- mechanical: material hardening
- thermal: conductivity, decomposition

The wide ranging impact of point defects accounts for the continuing research activity that began in 1926 when Yakov Frenkel introduced the concept of defects in a crystalline structure. Theoretical methods are particularly useful in this field as, although it is relatively straight forward to estimate the quantity of defects in a material, it is much more challenging to identify the type of defect.

. In this section I first outline the different types of crystal defects, and then discuss the thermodynamics of (charged) defect formation. I end the section by outlining the supercell method for calculating defect properties. This method was used in Chapter ??, where I calculate electronic structure properties which lead to a description of the defects in $\text{CH}_3\text{NH}_3\text{PbI}_3$.

3.3.1 Classification of crystal defects

The first way to classify defects is via their dimension. 0-dimensional are localised around isolated sites in the crystal and are known as point defects. 1-dimensional are lines along which the crystal pattern is broken and are called dislocations. 2-dimensional defects are surfaces along which distinct crystallites are joined and are called grain boundaries or interfaces. 3-dimensional defects are changes to the crystal pattern in finite volumes, this includes precipitates and voids.

The remainder of this thesis concerns 0-dimensional point defects, which can be further split into extrinsic or intrinsic defects. Extrinsic point defects are impurity atoms, different from the host species. These defects may be added intentionally (for example, to increase electrical conductivity) or unintentionally (as a result of the fabrication method). Intrinsic point defects are associated with host species.

Point defects can also be classified as non-stoichiometric or stoichiometric. Non-stoichiometric defects include interstitials (where an additional atom occupies a site that is unoccupied in the perfect lattice), vacancies (missing atoms) and anti-sites (where atom occupies a site that is occupied by another species in the perfect lattice). Interstitials can have a "split" structure,

in which two atoms are split symmetrically around a single lattice site. Stochiometric defects include Frenkel pairs, Shottky pairs. The stoichiometric and non-stoichiometric defects are illustrated in Figure 3.8.

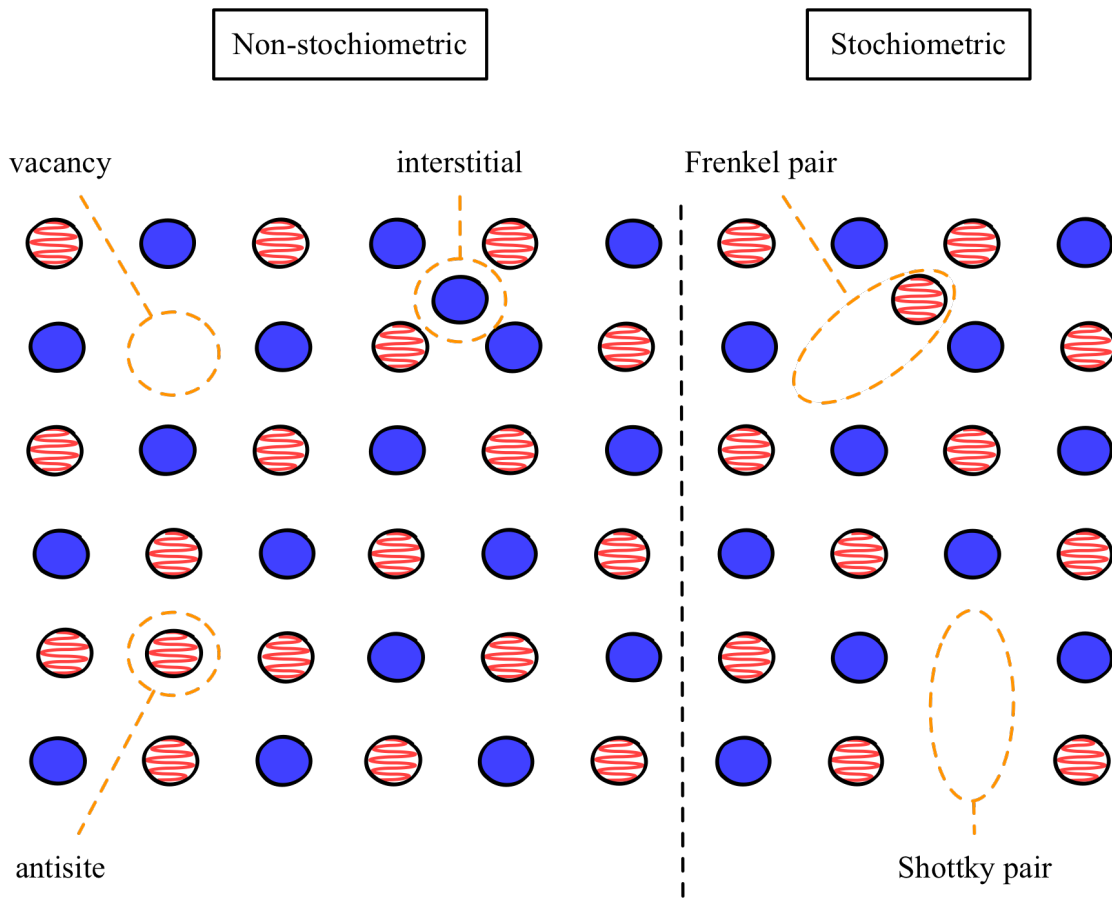


Figure 3.8: Non-stoichiometric defects include interstitials (additional atom), vacancies (missing atom) and anti-sites. Stoichiometric defects include a Frenkel pair (a vacancy close to an interstitial of the same species), and a Shottky pair (a vacancy on both the anion and cation sub-lattices).

The final classification is into electrically active and electrically benign defects. Whilst electrically benign defects exist only in one charge state, electrically active defects can take more than one charge state; for example, single acceptors exist in a neutral or negatively charged state and single donors exist in a neutral or positively charged states. Amphoteric defects can exist in a negatively charged or positively charged state.

3.3.2 Energetics of defect formation

The equilibrium concentration of defects (n) at a fixed temperature and pressure is given by the density that minimizes the free energy.

$$n = N_{sites} \exp\left(-\frac{\Delta G}{k_B T}\right), \quad (3.13)$$

where ΔG is the Gibbs free energy of defect formation. The Gibbs free energy is approximated as the formation energy of the defect ΔE_f as this dominates over entropic contributions. The formation energy is given by

$$E_f(q) = E_d(q) - E_b[-] \sum_i \mu_i n_i + q(\epsilon_{VBM} + E_F) + E_{corr} \quad (3.14)$$

where $E_d(q)$ is the total energy of the defect supercell and E_b is the total energy of the perfect bulk. E_{corr} is a correction energy that is only needed for charged defects, and is discussed further in the following section. The remaining terms describe the energy needed to add or remove atoms and electrons. μ_i is the chemical potential of the atom, and n_i is the number that is added or removed. The chemical potential can be adjusted to describe different growth conditions; if the growth conditions are rich for species i then μ_i will be low. E_F is the Fermi level, referenced to the valence band maximum (ϵ_{VBM}).

The total energies can be calculated using DFT. Convergence criteria for calculations must be tight as, due to the exponential dependence of defect concentration on formation energy, small errors in the energy difference can lead to large errors in defect concentration.

The Fermi level is treated as a parameter, of which the defect formation energy is a linear function with a gradient equal to defect charge. This allows us to plot a graph of formation energy against Fermi level, as shown in Figure ???. Charge transition levels mark the fermi energy at which two charge states have the same defect formation energy. Electrically active defects have at least one charge transition state in the band gap. The charge transition level is equivalent to thermal ionization energy, the energy needed to add or remove electron(s).

Defect levels deep in the band gap correspond to localised wavefunctions. Carrier capture to these defect states is often associated with a large lattice distortion. Shallow defect levels (within thermal energy kT of the valence or conduction band) correspond to delocalised, hydrogenic-like defect wavefunctions.

3.3.3 Supercell method

Defect concentrations as low as one part in one million can have an influence on device performance. One way to model point defects in the dilute limit, when defect-defect interactions are negligible, is to build a supercell from multiple unit cells (Figure ??). This supercell must be large enough so that there is no interaction between a defect and its periodic images. This is the approach used in this work. Although the supercell method captures localised defects well, it cannot capture the behaviour of delocalised (or band resonant) defects due to the enforced periodicity.

It is possible to remove the constraint of translational symmetry and use an embedded approach whereby a region around the defect is modelled using DFT and this is embedded in a region that is modelled classically.

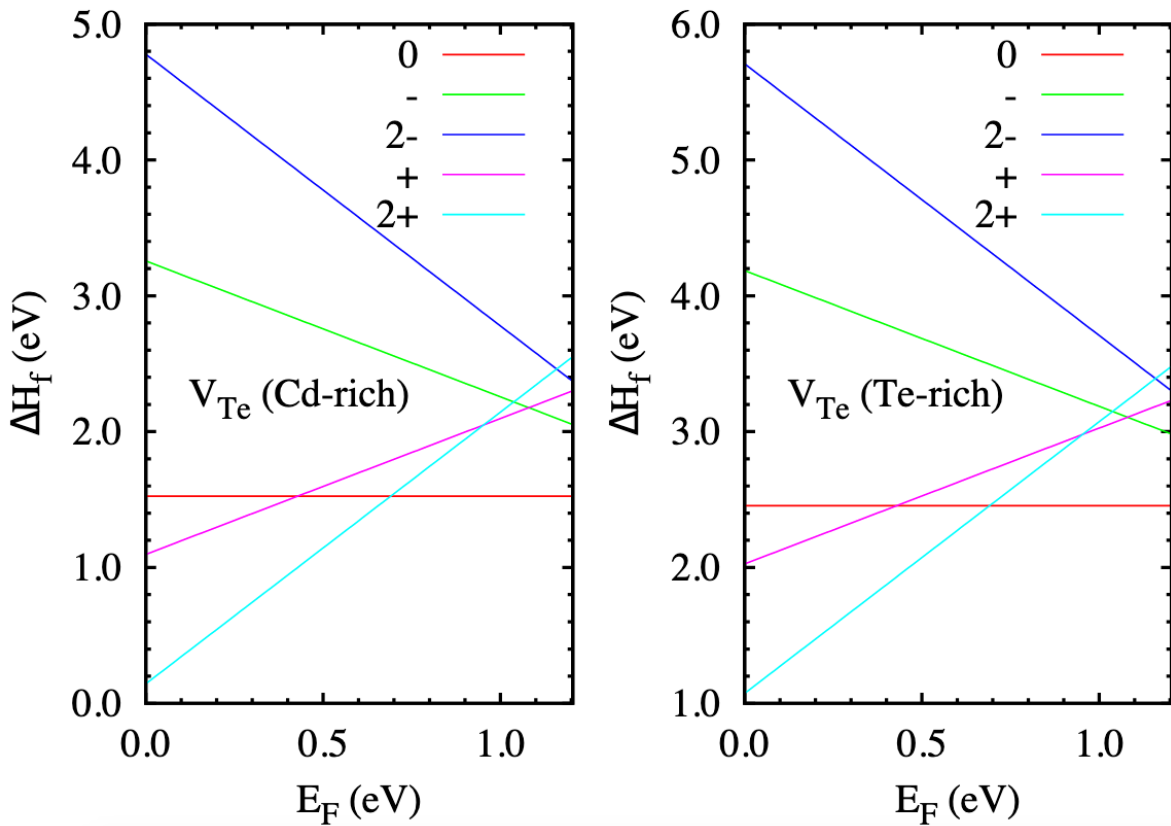


Figure 3.9: Formation energies ΔH_f as a function of the Fermi energy for the Te vacancy in CdTe. In a Te-rich environment it is more energetically unfavourable to form a Te-vacancy, as intuition would suggest. The slope of each line corresponds to the defect charge. Charge transition levels correspond to the energies at which the lines intersect.

Supercell corrections

Point defects can be electrically charged, and are able to change charge state through the trapping and de-trapping of electrons and holes. The charge state of a defect can affect a number of defect properties including the preferred lattice position, surrounding lattice distortion, and the rates for diffusion, carrier capture, and carrier recombination. However understanding the properties of charged defects is a challenge for DFT with periodic boundary conditions, due to the long range nature of the Coulomb interaction. There are two issues to resolve. Firstly, charged defects are able to interact with their periodic images; Secondly, a homogeneous "jellium" background charge is introduced to ensure overall charge neutrality. This results in an unknown shift to the average electrostatic potential. These are finite-size effects, that only a very large, almost infinite, supercell would overcome as the Coulomb potential decays very slowly. Such a supercell would certainly prove too costly, especially when higher levels of theory (for example, hybrid functionals) are required to calculate accurate total energies.

A number of correction schemes have been developed to deal with these issues; a brief historical overview is given below. These schemes are designed to be used as a post-processing step and

provide a value for the E_{corr} term in Eqn.3.14. For a more complete description of these issues we refer the reader to the existing literature.[167, 168]

The Leslie Gillan correction[169] models the defect charge q as a point charge interacting with its periodic images through an isotropic dielectric medium. This correction takes a simple analytic form that depends on the charge state q , static dielectric constant ϵ , separation between images L and the Madelung constant α_m , which is determined by the lattice geometry. The Markov-Payne correction extends the Leslie Gillan correction by including an additional term which accounts for the delocalised part of the defect charge.

$$E^{\text{MP}} = \frac{q^2 \alpha_m}{2\epsilon L} [+qQL^{-3}] \quad (3.15)$$

The challenge of this approach is in calculating the quadrupole moment Q . The Lany-Zunger correction[170] combines the Markov-Payne correction, including an approach for calculating Q , with a potential alignment procedure to correct for the shift in electrostatic potential. The Freysholdt, Neugebauer and van de Walle (FNV) method[171] models the defect charge as a localised gaussian distribution. The difference between the electrostatic potential of the charged defect supercell and the electrostatic potential of the perfect bulk supercell, calculated far from the defect, is aligned with the defect model potential. Kumagai and Oba have extended to FNV method by using atomic site potentials combined with a point charge model for an anisotropic medium.[172]

The schemes discussed were initially developed for use with three-dimensional materials. Recent work has extended these methods to two-dimensional[173, 174] and one-dimensional[175] materials. We note that there is still no standardised approach to defect charge corrections, which can lead to a spread in calculated defect formation energies in the literature, and predicted defect densities which differ by orders of magnitude. Two widely used approaches in the recent literature are the FNV method, and the extension to this provided by Kumagai and Oba. Both schemes are implemented in the `sxdefectalign`, as outlined in the following section. Developing an efficient scheme which can account for microscopic effects and anisotropy is an active area of research.[167, 168]

3.4 Lattice dynamics

Heisenberg's uncertainty principle, a central principle of quantum mechanics, states that we cannot know both the position and momentum of a particle exactly. Thus the static lattice model used so far is not true for real material; even at $T = 0\text{K}$ there is zero point motion. As temperature increases, this motion increases in amplitude.

Understanding the vibrations of crystals is key to understanding a range of physical phenomena. The motion of the atoms have an associated vibrational energy, and this determines crystal stability as a function of temperature via the Gibbs free energy:

$$G = E_0 + E_{\text{vib}} + PV - TS \quad (3.16)$$

where E_0 is the ground state energy as calculated using DFT and E_{vib} is the vibrational contribution to internal energy. Atomic motion also influences electrical and optical crystal properties; this can be seen experimentally in the homogeneous broadening of photoluminescence linewidths with temperature. Other material properties which are only accessible via lattice dynamics include: heat capacity, thermal conductivity, elasticity, thermal expansion coefficients, electron-phonon coupling strengths and static polarization.

For atomic motion at small amplitudes around the potential energy minimum it is common to use the harmonic approximation, where the atom moves as if it is connected by a spring to its neighbouring atoms (Figure 3.11). This is discussed in Section ???. At larger vibration amplitudes, and to understand processes related to the creation and annihilation of phonons, we must consider anharmonic motion, and this is considered in Section ??.

These motions are determined by the force on each atom. For simple systems, for example a one-dimensional diatomic chain, we can calculate atomic position as a function of time analytically. Otherwise methods such as DFT can be used to build a force constant matrix which, after some post-processing steps, gives the eigenvectors (direction) and frequencies of motion. This is discussed in Section ???. As in the previous sections of this chapter, we use the Born-Oppenheimer approximation and assume that the equilibrium positions in a crystal are the minima of the potential energy surface when the electron and nuclear motion are decoupled.

3.4.1 Harmonic approximation

??

If displacements from equilibrium are small, the total energy can be Taylor expanded in the form

$$E = \text{kinetic energy} + \text{potential energy} = \sum_i \frac{1}{2} Mx_i^2 + \sum_{ij} \frac{1}{2} \mathbf{x}_i \cdot \mathbf{A}_{ij} \cdot \mathbf{x}_j + \text{higher-order terms.} \quad (3.17)$$

The structure is relaxed and forces are equal to zero so that there is no term linear in \mathbf{x} . The harmonic approximation ignores the higher order terms in Equation 3.17. For these harmonic systems there exists a basis set so that \mathbf{A}_{ij} is diagonal and the oscillators are independent of one another:

$$= \sum_i \frac{1}{2} MQ_i^2 + \sum_i \frac{1}{2} \mathbf{A}_{ii} \cdot \mathbf{x}_i + \text{higher-order terms.} \quad (3.18)$$

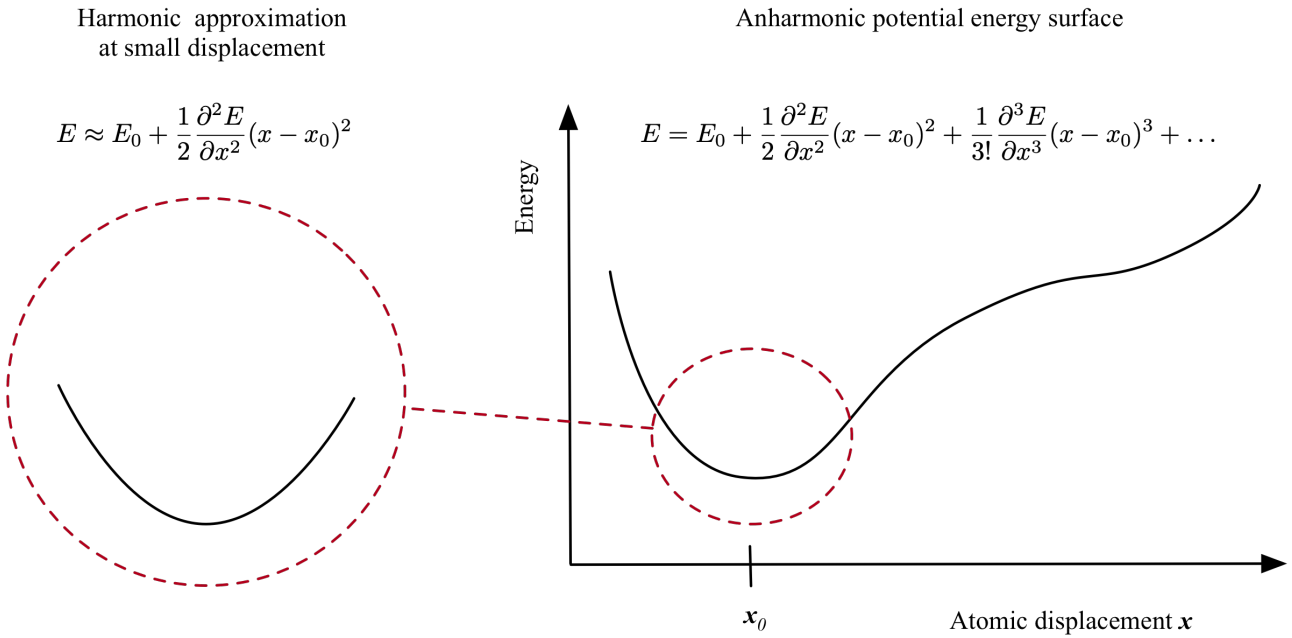


Figure 3.10: The crystal potential energy can be expanded with respect to atomic displacements x to simulate finite temperature behaviour of material. At small displacements, the anharmonic terms (third order and above) can be ignored, giving the harmonic approximation. The crystal lattice is relaxed so that all forces on the atoms are zero and there is no first order term.

The general solution to this system of equations for an N -atom unit cell in three dimensions is a superposition of $3N$ normal modes of vibration, each with its own frequency and eigenvector. To calculate the normal modes (phonons) we start Newton's second law, $F = ma$. For crystalline solids we take advantage of symmetry and seek normal modes that for a chosen wavevector k are a linear combination of a relative displacement within the unit cell $\mathbf{u}_0(i, \mathbf{k})$, a phase that depends on the unit cell $\exp(i\mathbf{k} \cdot \mathbf{R}_I)$, and an oscillation in time $\exp(i\omega(\mathbf{k})t)$

$$\mathbf{u}_0(i, \mathbf{k})\exp(i\mathbf{k} \cdot \mathbf{R}_I)\exp(i\omega(\mathbf{k})t) \quad (3.19)$$

If we seek displacements of this form, Newton's second law has consistent solutions only if the secular equation is satisfied:

$$\text{Det} \left| \sum_J A_{\alpha\beta}(iI, jJ) \exp(i\mathbf{k} \cdot \mathbf{R}_J) - M_i \delta_{ij} \omega^2(\mathbf{k}) \right| = 0 \quad (3.20)$$

where the first term in the determinant is called the dynamical matrix which is built from the force constant matrix $A_{\alpha\beta}$:

$$\mathbf{A} = \begin{pmatrix} \frac{\delta^2 E}{\delta x_1^2} & \frac{\delta^2 E}{\delta x_1 \delta x_2} & \cdots & \frac{\delta^2 E}{\delta x_1 \delta x_n} \\ \frac{\delta^2 E}{\delta x_2 \delta x_1} & \frac{\delta^2 E}{\delta x_2^2} & \cdots & \frac{\delta^2 E}{\delta x_2 \delta x_n} \\ \vdots & \vdots & \ddots & \vdots \\ \frac{\delta^2 E}{\delta x_n \delta x_1} & \frac{\delta^2 E}{\delta x_n \delta x_2} & \cdots & \frac{\delta^2 E}{\delta x_n^2} \end{pmatrix} \quad (3.21)$$

The normal mode frequencies are the roots of Equation 3.19 and can be found through matrix diagonalisation. Plotting the frequency ω against wavevector k gives a bandstructure plot with periodicity $\frac{2\pi}{a}$, similar to that in Section ??.

The discussion so far has only used classical mechanics. To introduce quantum effects we recognise that the harmonic lattice vibrations will be analogous to a quantum simple harmonic oscillator and so will be restricted to certain energy values $E_n = (n + \frac{1}{2}\hbar\omega)$. The phonon eigenvectors and frequencies can be used to calculate thermodynamic properties such as the Gibbs free energy and heat capacity.

3.4.2 Anharmonicity

??

Anharmonic atomic motion is considered when the higher order terms in Equation 3.17 are included. The third order term accounts for phonon-phonon scattering which, due to the conservation of energy and momentum, is a three particle process (Figure 3.22). The linear boltzmann transport equation (LBTE) describes a thermodynamic system out of equilibrium. Solving the LBTE under the single mode relaxation time approximation gives an expression for lattice thermal conductivity κ . The phonon-phonon scattering rate determines the phonon lifetime τ_λ which is a key quantity in the expression for κ :

$$\kappa = \frac{1}{NV_0} \sum_{\lambda} C_{\lambda} v_{\lambda} \times v_{\lambda} \tau_{\lambda} \quad (3.22)$$

where N is the number of unit cells in the crystal, V_0 is the unit cell volume, and C_{λ} , v_{λ} and τ_{λ} are the mode-dependent heat capacity, group velocity and lifetime respectively. C_{λ} and v_{λ} can be calculated using the harmonic approximation. To consider the anharmonic phonon interactions that determine τ_{λ} it is necessary to calculate a third-order force constant matrix. This is often at high computational cost; 41,544 DFT electronic optimisations were required to calculate the thermal conductivity of a 96-atom unit cell in Reference [77].

Lattice anharmonicity is also important in materials with dynamic disorder. In the halide and oxide perovskites this disorder is a result of a double well potential energy surface corresponding to octahedral tilting at finite temperature (Figure 3.22). Chapter ?? of this work calculates the coupling between the double well phonon modes and electronic states in MAPI.

3.4.3 Finite displacement method

??

There are a number of ways to calculate the second order force constant matrix in Equation 3.21: finite displacement, density functional perturbation theory, ab-initio molecular dynamics or compressed sensing lattice dynamics. In this work the finite displacement approach (also known

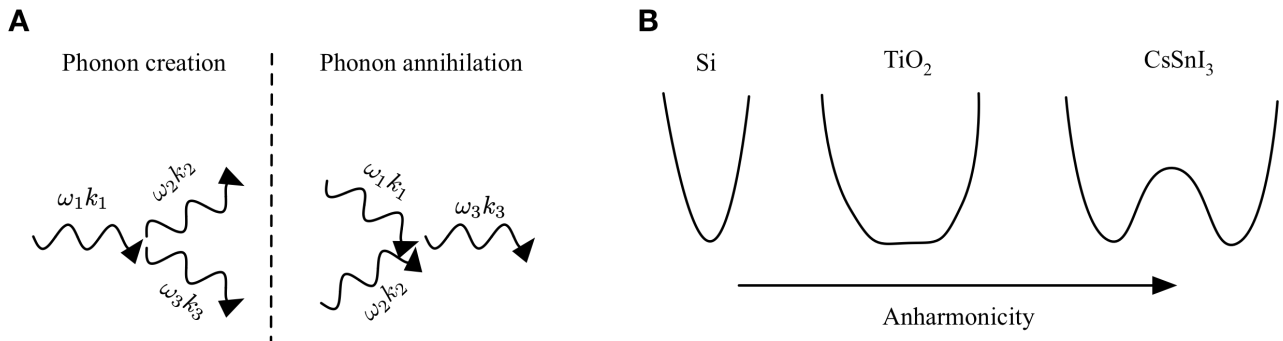


Figure 3.11: A) Energy and momentum are conserved during the creation or annihilation of phonons, so these are three-phonon processes (or higher); B) Some materials, such as silicon (Si) are well-described by a harmonic potential energy surface at typical solar cell operating temperatures. However other materials with dynamic disorder, such as the organic and inorganic perovskite halides, have highly anharmonic double well potentials.

as the direct or supercell method) is used as implemented in phonopy.?? In this approach, a single atom is displaced a small distance from its energetic minimum and there is a self-consistent electronic structure optimisation to calculate the resultant forces. The maximum number of displacements for a system with N atoms is $6N$ although this is reduced through symmetry (as implemented in spglib). A supercell is required to capture phonon wavelengths greater than the unit cell length (which corresponds to all k -points in the Brillouin Zone except γ) and forces must be well converged (typically to less than $0.01 \text{ eV} \text{\AA}^{-1}$).

3.5 Summary

“I don’t know where I’m going from here, but I promise it won’t be boring.”

— David Bowie

Closing Remarks

Many opportunities ahead as we pick apart.....(from end of review) include outstanding research questions from late stage review

For my own work: not touched on is toxicity and drive to replace lead. The lead is important for transport properties. The lead is in a 2+ charge state. This means it has the chemical structure 6s² 6p⁰. This means that the dispersive s-orbital is active in the valence band. So when charge electrons are excited to the conduction band the holes are in a dispersive valence band and so can provide ambi-polar transport. The iodine provides dispersive conduction band edge (from real-space structure can see there must be hybridization as there is no Pb overlap). Pb has the edge over Sn based compounds as the s electrons in Pb are deeper down and so harder to remove. In Sn based perovskites the Sn²⁺ wants to form Sn⁴⁺ which kills the transport (dispersion) and leads to breakdown of the material (formation of different phases) – the Sn wants to oxidise. concentrated on prototypical to understand fundamentals

Also ferroelectricity and Evidence for ferroelectric superhighways (predicted in atomistic simulations...): Tetragonal MAPI is ferroelectric from david cahen group. and starrynight.

Future of PV: - being combined with batteries for continuous power, is this the limiting? The other big thing is storage networks. This and BIPV listed as things for large scale PV deployment in Raugil nad Frankl 2009 - BIPV: This is what Dyesol company want to do. They are not going to compete with silicon on the arrays of solar farms. Going to look into market where silicon has not penetrated: where it cannot because of need to be solid single crystal. Aim is functionalisation of buildings with PV. Printing on steel.

It seems that there are technological solutions, but not the political will: what should the role of scientist be?

Modelling - baby in the bathtub. In a complex system with so much interconnected

Analysis software has been made open, testing, documentation - reproducibility in science / reusable

If our motivation is environment, need to think of as whole - battery / timescales

I motivation is for the understanding itself, there is a lot left to understand in hybrid perovskite materials.

Future - ML - <https://journals.aps.org/prl/pdf/10.1103/PhysRevLett.122.225701>

For the wider field:

Need to move to offline Reproducibility

Appendices

A

DFT bandstructures

The following pages contain the DFT calculated bandstructures which were analysed to give the effective mass values in Table ???. All DFT calculations use the HSE06 exchange correlation functional, and results are given with and without spin-orbit coupling. The output files for calculations using LDA and PBEsol functionals can be found in an online repository ??.

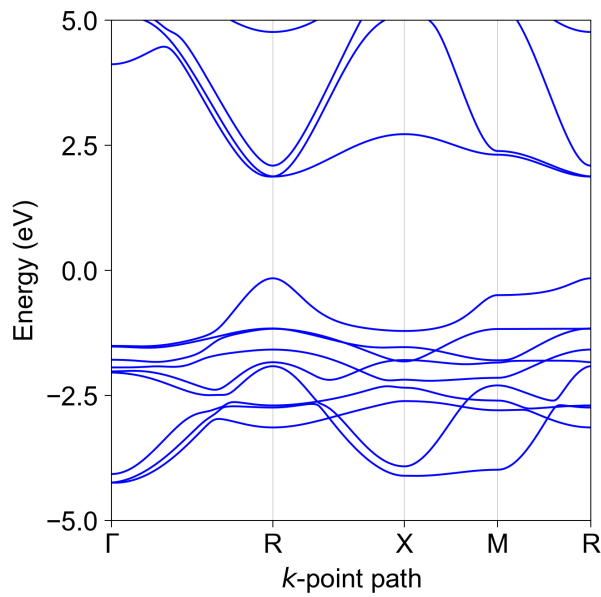


Figure A.1: MAPI bandstructure with the HSE06 functional, without spin-orbit coupling.

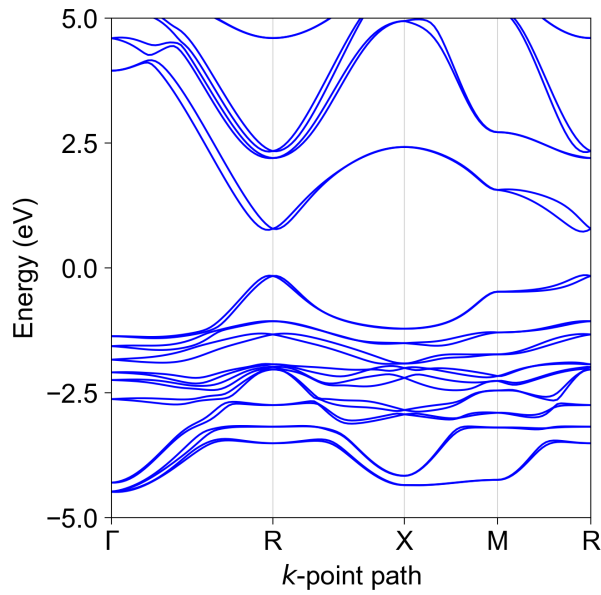


Figure A.2: MAPI bandstructure with the HSE06 functional, with spin-orbit coupling.

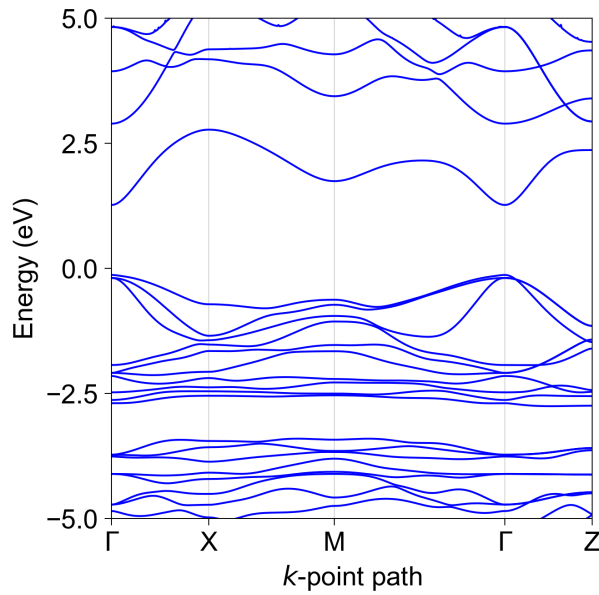


Figure A.3: CZTS bandstructure with the HSE06 functional, without spin-orbit coupling.

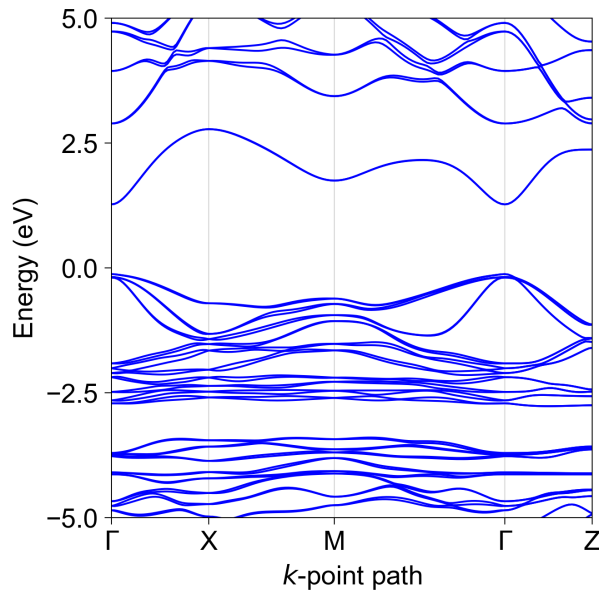


Figure A.4: CZTS bandstructure with the HSE06 functional, with spin-orbit coupling.

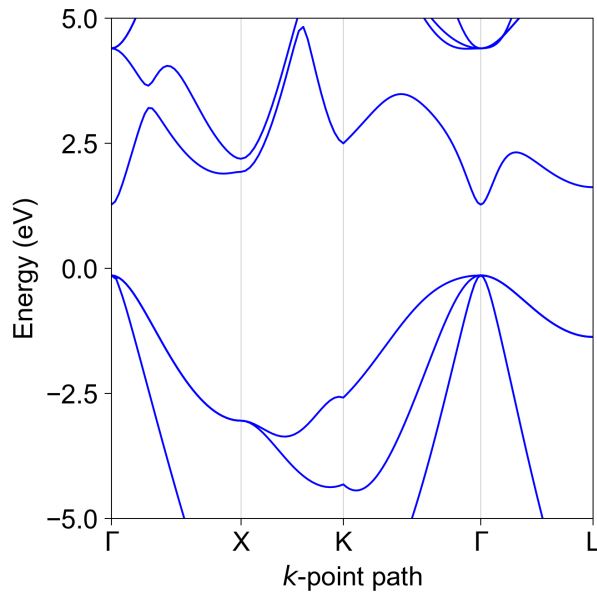


Figure A.5: GaAs bandstructure with the HSE06 functional, without spin-orbit coupling.

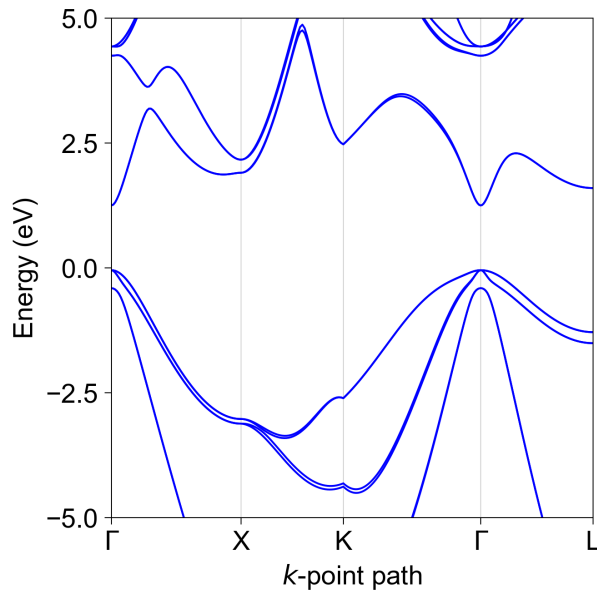


Figure A.6: GaAs bandstructure with the HSE06 functional, with spin-orbit coupling.

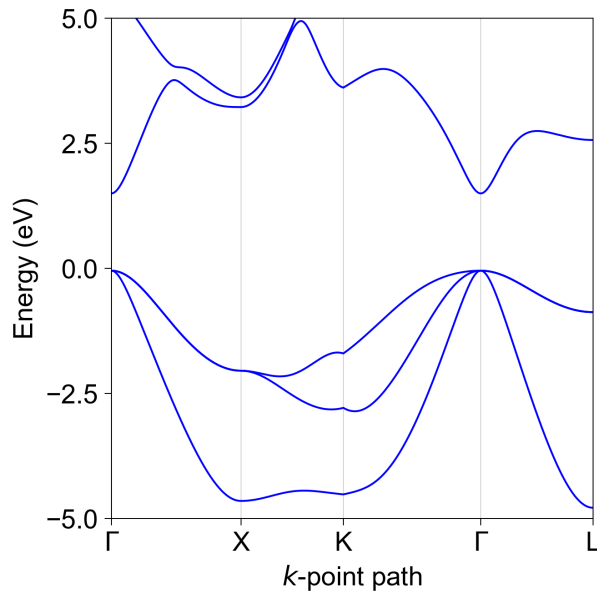


Figure A.7: CdTe bandstructure with the HSE06 functional, without spin-orbit coupling.

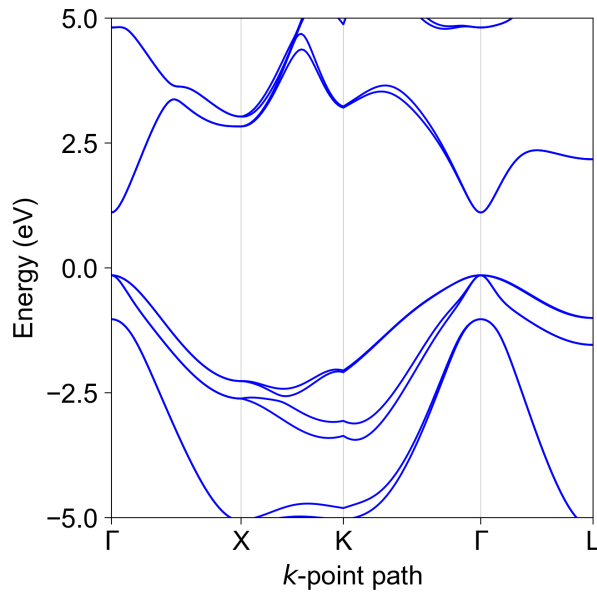


Figure A.8: CdTe bandstructure with the HSE06 functional, with spin-orbit coupling.

B

Effective mass and k -point spacing

Table B.1: The curvature effective mass (Equation ??, in units of electron rest mass) calculated for different k -point spacings in reciprocal space for an electron in the [100] direction of CZTS. The finite difference fit and unweighted least-squares fit are calculated using three points. The weighted least squares fit is calculated using points up to 0.25 eV in energy. Details of each method are included in the Methods section of Chapter 4 in the main text. Calculations use the PBEsol exchange-correlation functional with spin-orbit coupling.

k -poing spacing (\AA^{-1})	finite diff.	unweighted	weighted
0.005	0.06	0.05	0.07
0.010	0.07	0.06	0.07
0.015	0.08	0.06	0.07
0.020	0.10	0.07	0.07
0.025	0.12	0.08	0.07

C

effmass: An effective mass package

C.1 Summary

Many semiconductor properties depend on the response of electrons to an external perturbation. This perturbation could take the form of an electric field, change in temperature or an applied lattice stress. In a crystal, this response depends on the interaction of the electrons with a periodic potential. The effective mass approximation assumes that the response of an electron in a periodic potential is equivalent to that of a free electron with a renormalised mass (called the “effective mass”). This makes the effective mass a critical parameter in models for the optical and transport properties of a semiconductor.

The effective mass has a number of definitions, depending on the perturbation under consideration. The conventional definition of effective mass is inversely proportional to the second derivative of electron energy with respect to electron momentum¹⁷⁶. This allows the effective mass to be easily calculated from ab-initio band structures, and there are existing codes which have implemented this (see section “Related packages” below).

We must approximate the band structure with a parabola for the previous definition to be valid¹⁷⁷. However, this approximation breaks down when there is a high concentration of electrons in the material - when, for example, the material is doped or excited under a laser. Instead, we can then approximate the band structure with the Kane quasi-linear dispersion¹⁷⁸, and the definition of effective mass is adapted accordingly.

effmass¹⁷⁹ is a Python 3 package for calculating various definitions of effective mass from the electronic bandstructure of a semiconducting material. It contains a core class that calculates the effective mass and other associated properties of selected band structure segments. effmass also contains functions for locating band structure extrema, calculating the Kane quasi-linear

dispersion parameters and plotting approximations to the true dispersion. Parsing of electronic structure data is facilitated by the vasppy¹⁸⁰ package.

The effmass package is aimed towards theoretical solid state physicists and chemists who have a basic familiarity with Python. Depending on the functionality and level of approximation you are looking for, it may be that one of the packages listed below will suit your needs better.

C.2 Related packages

Effective mass calculations are implemented in a number of other packages:

- vasppy¹⁸⁰: This is installed as a dependency of effmass. Calculates the effective mass using a least-squares quadratic fit for parabolic dispersions.
- sumo¹⁸¹: Calculates the effective mass using a least-squares fit for parabolic and non-parabolic dispersions.
- emc¹⁸²: Calculates the effective mass tensor using a finite-difference method for parabolic dispersions.
- pymatgen¹⁸³: This is installed as a dependency of effmass. Calculates an average effective mass tensor for non-parabolic dispersions with multiple bands and extrema. Also calculates the Seebeck effective mass as defined here.

C.3 Unique features of effmass

To our knowledge, the following features are unique to this package:

- easily compare the values of curvature effective mass calculated using multiple numerical techniques (least-squares and polynomial fitting)
- tailor the polynomial fitting used to approximate the DFT calculated dispersion: by choosing the order of the polynomial and the energy range to fit over.
- visualise the dispersions used to approximate the DFT calculated dispersion
- quantify non-parabolicity through the Kane dispersion parameters: effective mass at band-edge and alpha
- calculate the optical effective mass assuming a Kane dispersion.

C.4 Acknowledgements

LW would like to thank Aron Walsh, Benjamin Morgan and Jarvist Moore Frost for their guidance during this project. This package was written during a PhD funded by the EPSRC through the Centre for Doctoral Training in New and Sustainable Photovoltaics (grant no.

EP/L01551X/1). The input data used for developing and testing this package was generated using the ARCHER UK National Supercomputing Service. We have access to Archer via our membership of the UK’s HEC Materials Chemistry Consortium, which is funded by EPSRC (EP/L000202).

D

Diffusion equation for a hot sphere

In the case of spherical symmetry

$$\nabla^2 T = \frac{1}{r} \frac{\partial^2 (rT)}{\partial r^2}. \quad (\text{D.1})$$

Substituting this into the fourier equation gives

$$\frac{\partial T}{\partial t} = \frac{D}{r} \frac{d^2(rT)}{dr^2}, \quad (\text{D.2})$$

and we set the boundary condition as $T = f(r)$ at $t = 0$. Substituting $u = rT$ into Equation D.2 gives

$$\frac{\partial u}{\partial t} = D \frac{d^2(u)}{dr^2} \quad (\text{D.3})$$

with the boundary conditions $u = rf(r)$ at $t = 0$, $u = 0$ at $r = 0$. This solution is equivalent to the case of linear flow with one face at zero. To solve, we follow reference [184] and consider a distribution on r which is equal to but the opposite sign of a distribution on $-r$. This initial distribution is convolved with a gaussian kernal to give temperature T as a function of time t and position r :

$$u = rT(r, t) = \frac{\eta}{\sqrt{\pi}} \left[\int_0^\infty \lambda f(\lambda) e^{-(\lambda-r)^2 \eta^2} \delta\lambda - \int_0^\infty \lambda f(\lambda) e^{-(\lambda+r)^2 \eta^2} \delta\lambda \right], \quad (\text{D.4})$$

where $\eta = \frac{1}{\sqrt{4Dt}}$ and λ is a variable of integration. Using the following definition for β and β'

$$\begin{aligned} \beta &= (\lambda - r)\eta, & \lambda &= \frac{\beta}{\eta} + r \\ \beta' &= (\lambda + r)\eta, & \lambda &= \frac{\beta'}{\eta} - r, \end{aligned} \quad (\text{D.5})$$

we recast Equation D.4 as:

$$T(r, t) = \frac{1}{r\sqrt{\pi}} \left[\int_{r\eta}^\infty \left(\frac{\beta}{\eta} + r \right) f \left(\frac{\beta}{\eta} + r \right) e^{-\beta^2} \delta\beta - \int_{r\eta}^\infty \left(\frac{\beta'}{\eta} - r \right) f \left(\frac{\beta'}{\eta} - r \right) e^{-\beta'^2} \delta\beta' \right]. \quad (\text{D.6})$$

For a sphere with radius R at temperature $T = T_0$, in a surrounding volume at zero temperature, the expression for $T(r, t)$ is given by:

$$T(r, t) = \frac{T_0}{r\sqrt{\pi}} \left[\int_{-r\eta}^{(R-r)\eta} \left(\frac{\beta}{\eta} + r \right) e^{-\beta^2} \delta\beta - \int_{r\eta}^{(R+r)\eta} \left(\frac{\beta}{\eta} - r \right) e^{-\beta^2} \delta\beta \right] \quad (\text{D.7})$$

Using the integral identity

$$\int \beta e^{\beta^2} = \frac{1}{2} e^{\beta^2}, \quad (\text{D.8})$$

and the error function

$$\operatorname{erf}(x) = \int_0^x e^{-\beta^2} \delta\beta, \quad (\text{D.9})$$

we reach the final analytical expression for temperature:

$$T(r, t) = \frac{T_0}{2} \left[\operatorname{erf}((R-r)\eta) + \operatorname{erf}((R+r)\eta) \right] - \frac{T_0 \sqrt{Dt}}{r\sqrt{\pi}} \left[e^{-\frac{(R-r)^2}{4Dt}} - e^{-\frac{(R+r)^2}{4Dt}} \right]. \quad (\text{D.10})$$

E

Copyright permissions

Rightslink® by Copyright Clearance Center

<https://s100.copyright.com/AppDispatchServlet>



Title: H-Center and V-Center Defects in Hybrid Halide Perovskites
Author: Lucy D. Whalley, Rachel Crespo-Otero, Aron Walsh
Publication: ACS Energy Letters
Publisher: American Chemical Society
Date: Dec 1, 2017
Copyright © 2017, American Chemical Society

Home

Create Account

Help



LOGIN

If you're a [copyright.com user](#), you can login to RightsLink using your copyright.com credentials. Already a [RightsLink user](#) or want to [learn more?](#)

PERMISSION/LICENSE IS GRANTED FOR YOUR ORDER AT NO CHARGE

This type of permission/license, instead of the standard Terms & Conditions, is sent to you because no fee is being charged for your order. Please note the following:

- Permission is granted for your request in both print and electronic formats, and translations.
- If figures and/or tables were requested, they may be adapted or used in part.
- Please print this page for your records and send a copy of it to your publisher/graduate school.
- Appropriate credit for the requested material should be given as follows: "Reprinted (adapted) with permission from (COMPLETE REFERENCE CITATION). Copyright (YEAR) American Chemical Society." Insert appropriate information in place of the capitalized words.
- One-time permission is granted only for the use specified in your request. No additional uses are granted (such as derivative works or other editions). For any other uses, please submit a new request.

BACK

CLOSE WINDOW

Copyright © 2019 [Copyright Clearance Center, Inc.](#). All Rights Reserved. [Privacy statement](#). [Terms and Conditions](#).
Comments? We would like to hear from you. E-mail us at customercare@copyright.com



26-Jun-2019

This license agreement between the American Physical Society ("APS") and Lucy Whalley ("You") consists of your license details and the terms and conditions provided by the American Physical Society and SciPris.

Licensed Content Information

License Number:	RNP/19/JUN/016080
License date:	26-Jun-2019
DOI:	10.1103/PhysRevB.99.085207
Title:	Impact of nonparabolic electronic band structure on the optical and transport properties of photovoltaic materials
Author:	Lucy D. Whalley et al.
Publication:	Physical Review B
Publisher:	American Physical Society
Cost:	USD \$ 0.00

Request Details

Does your reuse require significant modifications: Yes

Modification Details:

Yes - I am first author. I have included text and figures from the supplemental information in the main text and made other small edits to maintain consistency throughout the thesis.

Specify intended distribution locations:	Worldwide
Reuse Category:	Reuse in a thesis/dissertation
Requestor Type:	Author of requested content
Items for Reuse:	Whole Article
Format for Reuse:	Print and Electronic
Total number of print copies:	Up to 1000

Information about New Publication:

University/Publisher:	Imperial College London
Title of dissertation/thesis:	Defects and Distortions in hybrid halide perovskites
Author(s):	Lucy Whalley
Expected completion date:	Sep. 2019

License Requestor Information

Name:	Lucy Whalley
Affiliation:	Individual
Email Id:	lucywhalley@gmail.com
Country:	United Kingdom



TERMS AND CONDITIONS

The American Physical Society (APS) is pleased to grant the Requestor of this license a non-exclusive, non-transferable permission, limited to Print and Electronic format, provided all criteria outlined below are followed.

1. You must also obtain permission from at least one of the lead authors for each separate work, if you haven't done so already. The author's name and affiliation can be found on the first page of the published Article.
2. For electronic format permissions, Requestor agrees to provide a hyperlink from the reprinted APS material using the source material's DOI on the web page where the work appears. The hyperlink should use the standard DOI resolution URL, <http://dx.doi.org/{DOI}>. The hyperlink may be embedded in the copyright credit line.
3. For print format permissions, Requestor agrees to print the required copyright credit line on the first page where the material appears: "Reprinted (abstract/excerpt/figure) with permission from [(FULL REFERENCE CITATION) as follows: Author's Names, APS Journal Title, Volume Number, Page Number and Year of Publication.] Copyright (YEAR) by the American Physical Society."
4. Permission granted in this license is for a one-time use and does not include permission for any future editions, updates, databases, formats or other matters. Permission must be sought for any additional use.
5. Use of the material does not and must not imply any endorsement by APS.
6. APS does not imply, purport or intend to grant permission to reuse materials to which it does not hold copyright. It is the requestor's sole responsibility to ensure the licensed material is original to APS and does not contain the copyright of another entity, and that the copyright notice of the figure, photograph, cover or table does not indicate it was reprinted by APS with permission from another source.
7. The permission granted herein is personal to the Requestor for the use specified and is not transferable or assignable without express written permission of APS. This license may not be amended except in writing by APS.
8. You may not alter, edit or modify the material in any manner.
9. You may translate the materials only when translation rights have been granted.
10. APS is not responsible for any errors or omissions due to translation.
11. You may not use the material for promotional, sales, advertising or marketing purposes.
12. The foregoing license shall not take effect unless and until APS or its agent, Aptara, receives payment in full in accordance with Aptara Billing and Payment Terms and Conditions, which are incorporated herein by reference.
13. Should the terms of this license be violated at any time, APS or Aptara may revoke the license with no refund to you and seek relief to the fullest extent of the laws of the USA. Official written notice will be made using the contact information provided with the permission request. Failure to receive such notice will not nullify revocation of the permission.
14. APS reserves all rights not specifically granted herein.
15. This document, including the Aptara Billing and Payment Terms and Conditions, shall be the entire agreement between the parties relating to the subject matter hereof.



26-Jun-2019

This license agreement between the American Physical Society ("APS") and Lucy Whalley ("You") consists of your license details and the terms and conditions provided by the American Physical Society and SciPris.

Licensed Content Information

License Number:	RNP/19/JUN/016081
License date:	26-Jun-2019
DOI:	10.1103/PhysRevB.94.220301
Title:	Phonon anharmonicity, lifetimes, and thermal transport in \$ \mathrm{CH}_3\mathrm{NH}_3\mathrm{PbI}_3 \$ from many-body perturbation theory
Author:	Lucy D. Whalley et al.
Publication:	Physical Review B
Publisher:	American Physical Society
Cost:	USD \$ 0.00

Request Details

Does your reuse require significant modifications: Yes

Modification Details:

Yes - I am lead author I will use figures, tables and edited portions of text selected from the supplementary information and main text.

Specify intended distribution locations:	Worldwide
Reuse Category:	Reuse in a thesis/dissertation
Requestor Type:	Author of requested content
Items for Reuse:	Whole Article
Format for Reuse:	Print and Electronic
Total number of print copies:	Up to 1000

Information about New Publication:

University/Publisher:	Imperial College London
Title of dissertation/thesis:	Defects and Distortions in hybrid halide perovskites
Author(s):	Lucy Whalley
Expected completion date:	Sep. 2019

License Requestor Information

Name:	Lucy Whalley
Affiliation:	Individual
Email Id:	lucywhalley@gmail.com
Country:	United Kingdom



TERMS AND CONDITIONS

The American Physical Society (APS) is pleased to grant the Requestor of this license a non-exclusive, non-transferable permission, limited to Print and Electronic format, provided all criteria outlined below are followed.

1. You must also obtain permission from at least one of the lead authors for each separate work, if you haven't done so already. The author's name and affiliation can be found on the first page of the published Article.
2. For electronic format permissions, Requestor agrees to provide a hyperlink from the reprinted APS material using the source material's DOI on the web page where the work appears. The hyperlink should use the standard DOI resolution URL, <http://dx.doi.org/{DOI}>. The hyperlink may be embedded in the copyright credit line.
3. For print format permissions, Requestor agrees to print the required copyright credit line on the first page where the material appears: "Reprinted (abstract/excerpt/figure) with permission from [(FULL REFERENCE CITATION) as follows: Author's Names, APS Journal Title, Volume Number, Page Number and Year of Publication.] Copyright (YEAR) by the American Physical Society."
4. Permission granted in this license is for a one-time use and does not include permission for any future editions, updates, databases, formats or other matters. Permission must be sought for any additional use.
5. Use of the material does not and must not imply any endorsement by APS.
6. APS does not imply, purport or intend to grant permission to reuse materials to which it does not hold copyright. It is the requestor's sole responsibility to ensure the licensed material is original to APS and does not contain the copyright of another entity, and that the copyright notice of the figure, photograph, cover or table does not indicate it was reprinted by APS with permission from another source.
7. The permission granted herein is personal to the Requestor for the use specified and is not transferable or assignable without express written permission of APS. This license may not be amended except in writing by APS.
8. You may not alter, edit or modify the material in any manner.
9. You may translate the materials only when translation rights have been granted.
10. APS is not responsible for any errors or omissions due to translation.
11. You may not use the material for promotional, sales, advertising or marketing purposes.
12. The foregoing license shall not take effect unless and until APS or its agent, Aptara, receives payment in full in accordance with Aptara Billing and Payment Terms and Conditions, which are incorporated herein by reference.
13. Should the terms of this license be violated at any time, APS or Aptara may revoke the license with no refund to you and seek relief to the fullest extent of the laws of the USA. Official written notice will be made using the contact information provided with the permission request. Failure to receive such notice will not nullify revocation of the permission.
14. APS reserves all rights not specifically granted herein.
15. This document, including the Aptara Billing and Payment Terms and Conditions, shall be the entire agreement between the parties relating to the subject matter hereof.

References

1. Masson-Delmotte, V. *et al.* *Special Report: Global Warming of 1.5°C* tech. rep. (The Intergovernmental Panel on Climate Change, 2018).
2. Kaneda, T. & Dupuis, G. *2017 World Population data sheet* tech. rep. (Population Reference Bureau, 2017).
3. Mackay, D. J. *Sustainable energy - without the hot air* (UIT, 2009).
4. NASA Goddard Institute for Space Studies. *GISS Surface Temperature Analysis (GISTEMP)* <https://data.giss.nasa.gov/gistemp> (Sept. 14, 2018).
5. *Extreme weather events in europe* tech. rep. (European Academies Science Advisory Council, 2018).
6. Black, M. T. & Karoly, D. J. Southern Australia's warmest October on record. *Bull. Am. Meteorol. Soc.* **97** (12 2016).
7. Abatzoglou, J. & Williams, A. Impact of anthropogenic climate change on wildfire across western US Forest. *Proc. Natl. Acad. Sci. U.S.A.* **113** (43 2016).
8. Sweet, W. V. In Tide's way - Southwestern Florida's 2015 sunny-day flood. *Bull. Amer. Meteor. Soc.* **97** (12 2016).
9. Van der Wiel, K. *et al.* Rapid attribution of the August 2016 flood-inducing extreme precipitation in south Louisiana to climate change. *Hydrol. Earth Syst. Sci.* **21** (2017).
10. Kopp, G. & Lean, J. L. A new, lower value of total solar irradiance: Evidence and climate significance. *Geophys. Res. Lett.* **38** (2011).
11. *Key world energy statistics* tech. rep. (International Energy Agency, 2017).
12. Mayer, J., Philipps, S., Hussein, N. S., Schlegl, T. & Senkpiel, C. *Current and future cost of photovoltaics* tech. rep. (Fraunhofer ISE, 2015).
13. Green, M. A. & Bremner, S. P. Energy conversion approaches and materials for high-efficiency photovoltaics. *Nat. Mater.* **16**, 23.
<http://dx.doi.org/10.1038/nmat4676> <http://10.1038/nmat4676> (2016).
14. Blakers, A. W. & Green, M. A. 20% efficiency silicon solar cells. *Appl. Phys. Lett.* **48**, 215–217 (1986).
15. Farmer, J. D. & Lafond, F. How predictable is technological progress? *Research Policy* **45**, 647 –665. <http://www.sciencedirect.com/science/article/pii/S0048733315001699> (2016).
16. Jager-Waldau, A. *PV Status Report 2017* tech. rep. (European Commission, 2017).
17. Brown, G. British power generation achieves first ever coal-free day. *The Guardian*.
<https://www.theguardian.com/environment/2017/apr/21/britain-set-for-first-coal-free-day-since-the-industrial-revolution> (June 27, 2019).
18. Vaughan, A. UK runs without coal power for three days in a row. *The Guardian*.
<https://www.theguardian.com/business/2018/apr/24/uk-power-generation-coal-free-gas-renewables-nuclear> (June 27, 2019).

19. *National Infrastructure Assessment* tech. rep. (National Infrastructure Commission, 2018).
20. *Expect the unexpected: The Disruptive power of low-carbon technology* tech. rep. (Grantham Institute - Climate Change and the Environment, 2017).
21. *2018 Outlook for Energy: A View to 2040* tech. rep. (ExxonMobil, 2018).
22. Creutzig, F. *et al.* The underestimated potential of Sol. Energy to mitigate climate change. *Nature Energy* **2**, 17140. <http://dx.doi.org/10.1038/nenergy.2017.140><http://10.1038/nenergy.2017.140><https://www.nature.com/articles/nenergy2017140{\#}supplementary-information> (2017).
23. Koppelaar, R. Solar-PV energy payback and net energy: Meta-assessment of study quality, reproducibility, and results harmonization. *Renewable Sustainable Energy Rev.* **72**, 1241–1255. <http://www.sciencedirect.com/science/article/pii/S1364032116306906> (2017).
24. Yoshikawa, K. *et al.* Silicon heterojunction solar cell with interdigitated back contacts for a photoconversion efficiency over 26%. *Nature Energy* **2**, 17032. <https://doi.org/10.1038/nenergy.2017.32><http://10.1038/nenergy.2017.32> (2017).
25. Nelson, J. *The Physics of Solar Cells* (Imperial College Press, 2003).
26. Rau, U. Reciprocity relation between photovoltaic quantum efficiency and electroluminescent emission of solar cells. *Phys. Rev. B* **76**, 085303. <https://link.aps.org/doi/10.1103/PhysRevB.76.085303> (8 2007).
27. Braly, I. L., Stoddard, R. J., Rajagopal, A., Jen, A. K.-Y.-. & Hillhouse, H. W. Photoluminescence and Photoconductivity to Assess Maximum Open-Circuit Voltage and Carrier Transport in Hybrid Perovskites and Other Photovoltaic Materials. *The J. Phys. Chem. Lett.* **9**, 3779–3792. <https://doi.org/10.1021/acs.jpclett.8b01152> (2018).
28. Shockley, W. & Queisser, H. J. Detailed Balance Limit of Efficiency of p-n Junction Solar Cells. *J. Appl. Phys.* **32**, 510–519. <http://dx.doi.org/10.1063/1.1736034> (1961).
29. Polman, A., Knight, M., Garnett, E. C., Ehrler, B. & Sinke, W. C. Photovoltaic materials: Present efficiencies and future challenges. *Science* **352** (2016).
30. Yu, L. & Zunger, A. Identification of Potential Photovoltaic Absorbers Based on First-Principles Spectroscopic Screening of Materials. *Phys. Rev. Lett.* **108**, 068701. <https://link.aps.org/doi/10.1103/PhysRevLett.108.068701> (6 2012).
31. Bercx, M., Sarmadian, N., Saniz, R., Partoens, B. & Lamoen, D. First-principles analysis of the spectroscopic limited maximum efficiency of photovoltaic absorber layers for CuAu-like chalcogenides and silicon. *Phys. Chem. Chem. Phys.* **18**, 20542–20549. <http://dx.doi.org/10.1039/C6CP03468C> (30 2016).
32. Hirst, L. C., Walters, R. J., Führer, M. F. & Ekins-Daukes, N. J. Experimental demonstration of hot-carrier photo-current in an InGaAs quantum well solar cell. *Appl. Phys. Lett.* **104**, 231115 (2014).
33. Zunger, A. Inverse design in search of materials with target functionalities. *Nature Reviews Chemistry* **2**, 121. <https://doi.org/10.1038/s41570-018-0121><http://10.1038/s41570-018-0121> (2018).
34. Qu, X. *et al.* The Electrolyte Genome project: A big data approach in battery materials discovery. *Comp. Mat. Sci.* **103**, 56–67. <http://www.sciencedirect.com/science/article/pii/S0927025615001512> (2015).
35. Hachmann, J. *et al.* The Harvard Clean Energy Project: Large-Scale Computational Screening and Design of Organic Photovoltaics on the World Community Grid. *J. Phys. Chem. Lett.* **2**, 2241–2251 (2011).

36. Dunstan, M. T. *et al.* Large scale computational screening and experimental discovery of novel materials for high temperature CO₂ capture. *Energy Environ. Sci.* **9**, 1346–1360. <http://dx.doi.org/10.1039/C5EE03253A> (4 2016).
37. Brandt, R. E., Stevanović, V., Ginley, D. S. & Buonassisi, T. Identifying defect-tolerant semiconductors with high minority-carrier lifetimes: beyond hybrid lead halide perovskites. *MRS Commun.* **5**, 265–275 (2015).
38. Rühle, S. Tabulated values of the Shockley–Queisser limit for single junction solar cells. *Sol. Energy* **130**, 139 –147. <http://www.sciencedirect.com/science/article/pii/S0038092X16001110> (2016).
39. Rey, G. *et al.* On the origin of band-tails in kesterite. *Sol. Energy Mater. Sol. Cells* **179**, 142 –151. <http://www.sciencedirect.com/science/article/pii/S0927024817306062> (2018).
40. Poortmans, J. & Arkhipov, V. *Thin Film Solar Cells: Fabrication, Characterization and Applications* (John Wiley and Sons, 2006).
41. Brebels, J., Manca, J. V., Lutsen, L., Vanderzande, D. & Maes, W. High dielectric constant conjugated materials for organic photovoltaics. *J. Mater. Chem. A* **5**, 24037–24050. <http://dx.doi.org/10.1039/C7TA06808E> (46 2017).
42. Madelung, O. in *Semiconductors: Data Handbook* 173–244 (Springer Berlin Heidelberg, Berlin, Heidelberg, 2004).
43. Wilson, J. N., Frost, J. M., Wallace, S. K. & Walsh, A. Dielectric and ferroic properties of metal halide perovskites. *APL Mater.* **7**, 010901. <https://doi.org/10.1063/1.5079633> (2019).
44. Ganose, A. M., Butler, K. T., Walsh, A. & Scanlon, D. O. Relativistic electronic structure and band alignment of BiSI and BiSeI: candidate photovoltaic materials. *J. Mater. Chem. A* **4**, 2060–2068. <http://dx.doi.org/10.1039/C5TA09612J> (6 2016).
45. Butler, K. T., Kumagai, Y., Oba, F. & Walsh, A. Screening procedure for structurally and electronically matched contact layers for high-performance solar cells: hybrid perovskites. *J. Mater. Chem. C* **4**, 1149–1158. <http://dx.doi.org/10.1039/C5TC04091D> (6 2016).
46. Battersby, S. News Feature: The solar cell of the future. *Proceedings of the National Academy of Sciences* **116**, 7–10. <https://www.pnas.org/content/116/1/7> (2019).
47. Gaulois, M. W. *et al.* Data-Driven Review of Thermoelectric Materials: Performance and Resource Considerations. *Chem. Mater.* **25**, 2911–2920. <https://doi.org/10.1021/cm400893e> (2013).
48. Zakutayev, A. Brief review of emerging photovoltaic absorbers. *Current Opinion in Green Sustainable Chem.* **4**, 8 –15. <http://www.sciencedirect.com/science/article/pii/S245222361630092X> (2017).
49. Schaak, R. E. & Mallouk, T. E. Perovskites by Design: A Toolbox of Solid-State Reactions. *Chem. Mater.* **14**, 1455–1471. <http://pubs.acs.org/doi/abs/10.1021/cm010689m> (2002).
50. Møller, C. K. Crystal Structure and Photoconductivity of Caesium Plumbohalides. *Nature* **182**, 1436–1436. <http://www.nature.com/nature/journal/v182/n4647/abs/1821436a0.html> (1958).
51. Kojima, A., Teshima, K., Shirai, Y. & Miyasaka, T. Organometal halide perovskites as visible-light sensitizers for photovoltaic cells. *J. Am. Chem. Soc.* **131**, 6050–6051. <http://dx.doi.org/10.1021/ja809598r> (2009).
52. Stranks, S. D. & Snaith, H. J. Metal-halide perovskites for photovoltaic and light-emitting devices. *Nat. Nanotechnol.* **10**, 391–402. <http://dx.doi.org/10.1038/nnano.2015.90> (2015).

53. Saparov, B. & Mitzi, D. B. Organic–Inorganic Perovskites: Structural Versatility for Functional Materials Design. *Chem. Rev.* **116**, 4558–4596. <http://dx.doi.org/10.1021/acs.chemrev.5b00715> (2016).
54. Park, N.-G., Grätzel, M., Miyasaka, T., Zhu, K. & Emery, K. Towards stable and commercially available perovskite solar cells. *Nat. Energy* **1**, 16152. <http://www.nature.com/articles/nenergy2016152> (2016).
55. Walsh, A., Padure, N. P. & Il Seok, S. Physical chemistry of hybrid perovskite solar cells. *Phys. Chem. Chem. Phys.* **18**, 27024–27025. <http://xlink.rsc.org/?DOI=C6CP90212J> (2016).
56. Wallace, S. K., Mitzi, D. B. & Walsh, A. The Steady Rise of Kesterite Solar Cells. *ACS Energy Lett.* **2**, 776–779. <http://pubs.acs.org/articlesonrequest/AOR-DfQrdu9v4gxXNAJaDUMb{\%}OA> (2017).
57. He, Y. & Galli, G. Perovskites for Solar Thermoelectric Applications: a First Principle Study of $\text{CH}_3\text{NH}_3\text{AlI}_3$ (A=Pb and Sn). *Chem. Mater.* **26**, 5394–5400. <http://pubs.acs.org/doi/abs/10.1021/cm5026766> (2014).
58. Tuning of the Thermoelectric Figure of Merit of $\text{CH}_3\text{NH}_3\text{MI}_3$ (M=Pb,Sn) Photovoltaic Perovskites. *J. Phys. Chem. C* **119**, 11506–11510. <http://dx.doi.org/10.1021/acs.jpcc.5b03939> (2015).
59. Protesescu, L. *et al.* Nanocrystals of Cesium Lead Halide Perovskites (CsPbX_3 , X = Cl, Br, and I): Novel Optoelectronic Materials Showing Bright Emission with Wide Color Gamut. *Nano Lett.* **15**, 3692–3696. <http://dx.doi.org/10.1021/nl5048779> (2015).
60. Resistive Switching Behavior in Organic–Inorganic Hybrid $\text{CH}_3\text{NH}_3\text{PbI}_{3-x}\text{Cl}_x$ Perovskite for Resistive Random Access Memory Devices. *en. Adv. Mater.* **27**, 6170–6175. <http://onlinelibrary.wiley.com/doi/10.1002/adma.201502889/full> (2015).
61. Liu, D. *et al.* Flexible All-inorganic Perovskite CsPbBr_3 Non-volatile Memory Device. *ACS Appl. Mater. Interfaces* **9**, 6171–6176. <http://pubs.acs.org/doi/abs/10.1021/acsami.6b15149> (2017).
62. Frost, J. M. & Walsh, A. What Is Moving in Hybrid Halide Perovskite Solar Cells? *Acc. Chem. Res.* **49**, 528–535. <http://pubsdc3.acs.org/doi/abs/10.1021/acs.accounts.5b00431> (2016).
63. Weller, M. T., Weber, O. J., Henry, P. F., Di Pumbo, A. M. & Hansen, T. C. Complete structure and cation orientation in the perovskite photovoltaic methylammonium lead iodide between 100 and 352 K. *en. Chem. Commun.* **51**, 4180–4183. <http://pubs.rsc.org/en/content/articlehtml/2015/cc/c4cc09944c> (2015).
64. Brivio, F. *et al.* Lattice dynamics and vibrational spectra of the orthorhombic, tetragonal, and cubic phases of methylammonium lead iodide. *Phys. Rev. B* **92**, 144308. <http://journals.aps.org/prb/abstract/10.1103/PhysRevB.92.144308> (2015).
65. Mitzi, D. B. Templating and structural engineering in organic-inorganic perovskites. *J. Chem. Soc. Dalt. Trans.* **2001**, 1–12. <http://xlink.rsc.org/?DOI=b007070j> (2001).
66. Mitzi, D. B. Solution-processed inorganic semiconductors. *J. Mater. Chem.* **14**, 2355. <http://xlink.rsc.org/?DOI=b403482a> (2004).
67. Savory, C. N., Walsh, A. & Scanlon, D. O. Can Pb-free Halide Double Perovskites Support High-effciency Solar Cells? *ACS Energy Lett.* **1**, 949–955. <http://pubs.acs.org/doi/abs/10.1021/acsenergylett.6b00471> (2016).
68. Volonakis, G. *et al.* Lead-Free Halide Double Perovskites via Heterovalent Substitution of Noble Metals. *J. Phys. Chem. Lett.* **7**, 1254–1259. <http://dx.doi.org/10.1021/acs.jpclett.6b00376> (2016).

69. Weber, D. $\text{CH}_3\text{NH}_3\text{PbX}_3$, a Pb(II)-System with Cubic Perovskite Structure. *Zeitschrift für Naturforsch. B* **33b**, 1443–1445.
http://zfn.mpd1.mpg.de/xtf/data/Reihe{_}B/33/ZNB-1978-33b-1443.pdf (1978).
70. Weber, D. $\text{CH}_3\text{NH}_3\text{SnBr}_x\text{I}_{3-x}$ ($x=0\text{--}3$), a Sn(II)-system with the cubic perovskite structure. *Zeitschrift für Naturforsch. B* **33b**, 862–865.
http://zfn.mpd1.mpg.de/data/Reihe{_}B/33/ZNB-1978-33b-0862.pdf (1978).
71. Onoda-Yamamoto, N., Matsuo, T. & Suga, H. Calorimetric and IR spectroscopic studies of phase transitions in methylammonium trihalogenoplumbates (II). *J. Phys. Chem. Solids* **51**, 1383–1395. <http://linkinghub.elsevier.com/retrieve/pii/0022369790900217> (1990).
72. Yamamoto, O. *et al.* Neutron diffraction and calorimetric studies of methylammonium iodide. *Acta Crystallogr. Sect. B Struct. Sci.* **48**, 329–336.
<http://scripts.iucr.org/cgi-bin/paper?S0108768192000260> (1992).
73. Dielectric Study of $\text{CH}_3\text{NH}_3\text{PbX}_3$ ($X = \text{Cl}, \text{Br}, \text{I}$). *J. Phys. Chem. Solids* **53**, 935–939.
<http://www.sciencedirect.com/science/article/pii/002236979290121S> (1992).
74. Hutter, E. M. *et al.* Direct–indirect character of the bandgap in methylammonium lead iodide perovskite. *Nat. Mater.* **16**, 115–120.
<http://www.nature.com/doifinder/10.1038/nmat4765> (2017).
75. Poglitsch, A. & Weber, D. Dynamic disorder in methylammonium tri-halogenoplumbates (II) observed by millimeter-wave spectroscopy. *J. Chem. Phys.* **87**, 6373.
<http://scitation.aip.org/content/aip/journal/jcp/87/11/10.1063/1.453467> (1987).
76. The Cubic Perovskite Structure of Black Formamidinium Lead Iodide at 298 K. *J. Phys. Chem. Lett.* **6**, 3209–3212. <http://dx.doi.org/10.1021/acs.jpclett.5b01432> (2015).
77. Whalley, L. D., Skelton, J. M., Frost, J. M. & Walsh, A. Phonon anharmonicity, lifetimes, and thermal transport in $\text{CH}_3\text{NH}_3\text{PbI}_3$ from many-body perturbation theory. *Phys. Rev. B* **94** (22 2016).
78. Beecher, A. N. *et al.* Direct observation of dynamic symmetry breaking above room temperature in methylammonium lead iodide perovskite. *ACS Energy Lett.* **1**, 880–887.
<https://doi.org/10.1021/acsenergylett.6b00381> (2016).
79. Chang, Y. H., Park, C. H. & Matsuishi, K. First-principles study of the structural and the electronic properties of the lead-halide-based inorganic-organic perovskites $\text{CH}_3\text{NH}_3\text{PbX}_3$ and CsPbX_3 ($X = \text{Cl}, \text{Br}, \text{I}$). *J. Korean Phys. Soc.* **44**, 889–893.
http://www.kps.or.kr/jkps/abstract{_}view.asp?articleuid=948E1A56-BDC2-4366-9D21-F69A2245E8A5{\&}globalmenu=3{\&}localmenu=10 (2004).
80. Brivio, F., Walker, A. B. & Walsh, A. Structural and electronic properties of hybrid perovskites for high-efficiency thin-film photovoltaics from first-principles. *APL Mater.* **1**, 042111.
<http://scitation.aip.org/content/aip/journal/aplmater/1/4/10.1063/1.4824147> (2013).
81. Leguy, A. M. A. *et al.* The dynamics of methylammonium ions in hybrid organic-inorganic perovskite solar cells. en. *Nat. Commun.* **6**, 7124.
<http://www.nature.com/ncomms/2015/150529/ncomms8124/full/ncomms8124.html> (2015).
82. Chen, T. *et al.* Rotational dynamics of organic cations in $\text{CH}_3\text{NH}_3\text{PbI}_3$ perovskite. en. *Phys. Chem. Chem. Phys.* **17**, 31278–31286.
<http://pubs.rsc.org/en/content/articlehtml/2015/cp/c5cp05348j> (2015).
83. Bakulin, A. A. *et al.* Real-Time Observation of Organic Cation Reorientation in Methylammonium Lead Iodide Perovskites. *J. Phys. Chem. Lett.* **6**, 3663–3669.
<http://dx.doi.org/10.1021/acs.jpclett.5b01555> (2015).

84. Selig, O. *et al.* Organic Cation Rotation and Immobilisation in Pure and Mixed Methylammonium Lead-Halide Perovskites. *J. Am. Chem. Soc.* **139**, 4068 (2017).
85. Glazer, A. M. The classification of tilted octahedra in perovskites. *Acta Crystallogr. Sect. B* **28**, 3384–3392. <http://scripts.iucr.org/cgi-bin/paper?S0567740872007976> (1972).
86. Woodward, P. M. Octahedral Tilting in Perovskites. II. Structure Stabilizing Forces. *Acta Cryst. B* **53**, 44–66. <https://doi.org/10.1107/S0108768196012050> (1997).
87. Beecher, A. N. *et al.* Direct Observation of Dynamic Symmetry Breaking above Room Temperature in Methylammonium Lead Iodide Perovskite. *ACS Energy Lett.* **1**, 880–887. <http://pubs.acs.org/doi/abs/10.1021/acsenergylett.6b00381> (2016).
88. Frost, J. M., Butler, K. T. & Walsh, A. Molecular ferroelectric contributions to anomalous hysteresis in hybrid perovskite solar cells. *APL Mater.* **2**, 081506. <http://scitation.aip.org/content/aip/journal/aplmater/2/8/10.1063/1.4890246> (2014).
89. Quarti, C. *et al.* Structural and optical properties of methylammonium lead iodide across the tetragonal to cubic phase transition: implications for perovskite solar cells. en. *Energy Environ. Sci.* **16**, 155–163. <http://dx.doi.org/10.1039/C5EE02925B> (2016).
90. Mosconi, E., Quarti, C., Ivanovska, T., Ruani, G. & De Angelis, F. Structural and electronic properties of organo-halide lead perovskites: a combined IR-spectroscopy and ab initio molecular dynamics investigation. en. *Phys. Chem. Chem. Phys.* **16**, 16137–44. <http://www.ncbi.nlm.nih.gov/pubmed/24968243> (2014).
91. Saidi, W. A., Poncé, S. & Monserrat, B. Temperature Dependence of the Energy Levels of Methylammonium Lead Iodide Perovskite from First-Principles. *J. Phys. Chem. Lett.* **7**, 5247–5252 (2016).
92. Reuter, K. & Scheffler, M. First-Principles Atomistic Thermodynamics for Oxidation Catalysis: Surface Phase Diagrams and Catalytically Interesting Regions. *Phys. Rev. Lett.* **90**, 046103. <http://link.aps.org/doi/10.1103/PhysRevLett.90.046103> <http://prl.aps.org/abstract/PRL/v90/i4/e046103> <http://prl.aps.org/pdf/PRL/v90/i4/e046103> (2003).
93. Kim, Y. H., Kim, K. & Zhang, S. B. First-principles calculation of thermodynamic stability of acids and bases under pH environment: A microscopic pH theory. *J. Chem. Phys.* **136**, 134112–134114. <http://link.aip.org/link/?JCPA6/136/134112/1> (2012).
94. Jackson, A. J., Tiana, D. & Walsh, A. A universal chemical potential for sulfur vapours. *Chem. Sci.* **7**, 1082–1092. <http://pubs.rsc.org/en/Content/ArticleLanding/2015/SC/C5SC03088A> (2016).
95. Stoffel, R. P., Wessel, C., Lumey, M.-W. & Dronskowski, R. Ab initio thermochemistry of solid-state materials. *Angew. Chemie* **49**, 5242–66. <http://www.ncbi.nlm.nih.gov/pubmed/20572215> (2010).
96. Jackson, A. J. & Walsh, A. Ab initio thermodynamic model of Cu₂ZnSnS₄. *J. Mater. Chem. A* **2**, 7829–7836. <http://pubs.rsc.org/en/content/articlehtml/2014/ta/c4ta00892h> (2014).
97. Nagabhusana, G. P., Shivaramaiah, R. & Navrotsky, A. Direct calorimetric verification of thermodynamic instability of lead halide hybrid perovskites. *Proc. Natl. Acad. Sci.* **113**, 7717–7721. <http://www.pnas.org/lookup/doi/10.1073/pnas.1607850113> (2016).
98. Caskey, C. M., Richards, R. M., Ginley, D. S. & Zakutayev, A. Thin film synthesis and properties of copper nitride, a metastable semiconductor. *Mater. Horizons* **1**, 424. <http://xlink.rsc.org/?DOI=c4mh00049h> (2014).

99. Walsh, A. The quest for new functionality. *Nat. Chem.* **7**, 274–275. <http://dx.doi.org/10.1038/nchem.2213> (2015).
100. Sun, W. *et al.* The thermodynamic scale of inorganic crystalline metastability. *Science Adv.* **2**, e1600225 (2016).
101. Skelton, J. M., Burton, L. A., Oba, F. & Walsh, A. Metastable cubic tin sulfide: A novel phonon-stable chiral semiconductor. *APL Mater.* **5**, 036101. <http://aip.scitation.org/doi/10.1063/1.4977868> (2017).
102. Baikie, T. *et al.* Synthesis and crystal chemistry of the hybrid perovskite $\text{CH}_3\text{NH}_3\text{PbI}_3$ for solid-state sensitised solar cell applications. *J. Mater. Chem. A* **1**, 5628. <http://xlink.rsc.org/?DOI=c3ta10518k> (2013).
103. Madelung, O. M. *Semiconductors: Data Handbook* 3rd, 691 (Springer, Berlin, 2003).
104. Togo, A., Chaput, L. & Tanaka, I. Distribution of phonon lifetimes in Brillouin zones. *Phys. Rev. B* **91**, 094306. <http://journals.aps.org/prb/abstract/10.1103/PhysRevB.91.094306> (2015).
105. Volz, S. G. & Chen, G. Molecular-dynamics simulation of thermal conductivity of silicon crystals. *Phys. Rev. B* **61**, 2651 (2000).
106. Wang, M. & Lin, S. Anisotropic and Ultralow Phonon Thermal Transport in Organic-Inorganic Hybrid Perovskites: Atomistic Insights into Solar Cell Thermal Management and Thermoelectric Energy Conversion Efficiency. *Adv. Funct. Mater.* **26** (29 2016).
107. Brivio, F., Butler, K. T., Walsh, A. & van Schilfgaarde, M. Relativistic Quasiparticle Self-consistent Electronic Structure of Hybrid Halide Perovskite Photovoltaic Absorbers. *Phys. Rev. B* **89**, 155204. <http://link.aps.org/doi/10.1103/PhysRevB.89.155204> (2014).
108. Pérez-Osorio, M. A. *et al.* Vibrational Properties of the Organic-Inorganic Halide Perovskite $\text{CH}_3\text{NH}_3\text{PbI}_3$ from Theory and Experiment: Factor Group Analysis, First-Principles Calculations, and Low-Temperature Infrared Spectra. *EN. J. Phys. Chem. C* **119**, 25703–25718. <http://pubs.acs.org/doi/10.1021/acs.jpcc.5b07432> (2015).
109. Van Schilfgaarde, M., Kotani, T. & Faleev, S. Quasiparticle self-consistent GW theory. *Phys. Rev. Lett.* **96**, 1–4 (2006).
110. Kepenekian, M. *et al.* Rashba and Dresselhaus Effects in Hybrid Organic-Inorganic Perovskites: From Basics to Devices. *ACS Nano* **9**, 1557–11567. <http://dx.doi.org/10.1021/acsnano.5b04409> (2015).
111. Du, M.-H. Density Functional Calculations of Native Defects in $\text{CH}_3\text{NH}_3\text{PbI}_3$: Effects of Spin–Orbit Coupling and Self-Interaction Error. *J. Phys. Chem. Lett.* **6**, 1461–1466. <http://dx.doi.org/10.1021/acs.jpclett.5b00199> (2015).
112. Giustino, F. Electron-phonon interactions from first principles. *Rev. Mod. Phys.* **89**, 015003. <http://link.aps.org/doi/10.1103/RevModPhys.89.015003> (1 2017).
113. Zacharias, M. & Giustino, F. One-shot calculation of temperature-dependent optical spectra and phonon-induced band-gap renormalization. *Phys. Rev. B* **94**, 075125. <http://link.aps.org/doi/10.1103/PhysRevB.94.075125> (7 2016).
114. Li, Y. *et al.* Direct Observation of Long Electron-Hole Diffusion Distance in $\text{CH}_3\text{NH}_3\text{PbI}_3$ Perovskite Thin Film. *Sci. Rep.* **5**, 14485. <http://dx.doi.org/10.1038/srep14485> <http://10.1038/srep14485http://www.nature.com/articles/srep14485{\#}supplementary-information> (2015).
115. Karakus, M. *et al.* Phonon-electron-scattering limits free charge mobility in methylammonium lead iodide perovskites. *J. Phys. Chem. Lett.* **6**, 4991–4996. <http://dx.doi.org/10.1021/acs.jpclett.5b02485> (2015).

116. Yi, H. T., Wu, X., Zhu, X. & Podzorov, V. Intrinsic Charge Transport across Phase Transitions in Hybrid Organo-Inorganic Perovskites. *Adv. Mater.* **28**, 6509–6514. <http://doi.wiley.com/10.1002/adma.201600011> (2016).
117. Leguy, A. M. A. *et al.* Dynamic disorder, phonon lifetimes, and the assignment of modes to the vibrational spectra of methylammonium lead halide perovskites. *Phys. Chem. Chem. Phys.* **18**, 27051–27066. <http://pubs.rsc.org/en/content/articlelanding/2016/cp/c6cp03474h{\#}!divAbstract> (2016).
118. Wright, A. D. *et al.* Electron–phonon coupling in hybrid lead halide perovskites. en. *Nat. Commun.* **7**, 11755. <http://www.nature.com/ncomms/2016/160526/ncomms11755/full/ncomms11755.html> (2016).
119. Filippetti, A., Mattoni, A., Caddeo, C., Saba, M. I. & Delugas, P. Low electron-polar optical phonon scattering as a fundamental aspect of carrier mobility in methylammonium lead halide $\text{CH}_3\text{NH}_3\text{PbI}_3$ perovskites. *Phys. Chem. Chem. Phys.* **18**, 15352–15362. <http://pubs.rsc.org/en/content/articlelanding/2016/cp/c6cp01402j{\#}!divAbstract> (2016).
120. Ball, J. M. & Petrozza, A. Defects in perovskite-halides and their effects in solar cells. *Nat. Energy* **1**, 16149. <http://www.nature.com/articles/nenergy2016149> (2016).
121. Ma, J. & Wang, L.-W. Nanoscale charge localization induced by random orientations of organic molecules in hybrid perovskite $\text{CH}_3\text{NH}_3\text{PbI}_3$. *Nano Lett.* **15**, 248–253. <http://dx.doi.org/10.1021/nl503494y> (2014).
122. Brivio, F., Caetano, C. & Walsh, A. Thermodynamic Origin of Photoinstability in the $\text{CH}_3\text{NH}_3\text{Pb}(\text{I}_{1x}\text{Br}_x)_3$ Hybrid Halide Perovskite Alloy. *J. Phys. Chem. Lett.* 1083–1087.
123. Slotcavage, D. J., Karunadasa, H. I. & McGehee, M. D. Light-Induced Phase Segregation in Halide-Perovskite Absorbers. *ACS Energy Letters* **1**, 1199–1205. <http://dx.doi.org/10.1021/acsenergylett.6b00495> (2016).
124. Eames, C. *et al.* Ionic transport in hybrid lead iodide perovskite solar cells. en. *Nat. Commun.* **6**, 7497. <http://www.nature.com/ncomms/2015/150624/ncomms8497/full/ncomms8497.html> (2015).
125. Richardson, G. *et al.* Can slow-moving ions explain hysteresis in the current-voltage curves of perovskite solar cells? *Energy Environ. Sci.* **9**, 1476–1485. <http://dx.doi.org/10.1039/C5EE02740C> (4 2016).
126. Walsh, A. Principles of Chemical Bonding and Band Gap Engineering in Hybrid Organic-Inorganic Halide Perovskites. *J. Phys. Chem. C* **119**, 5755–5760. <http://pubs.acs.org/doi/abs/10.1021/jp512420b> (2015).
127. Meloni, S. *et al.* Ionic polarization-induced current-voltage hysteresis in $\text{CH}_3\text{NH}_3\text{PbX}_3$ perovskite solar cells. en. *Nat. Commun.* **7**, 10334. <http://www.nature.com/ncomms/2016/160208/ncomms10334/full/ncomms10334.html> (2016).
128. Bryant, D. *et al.* Observable hysteresis at low temperature in ‘hysteresis free’ lead halide perovskite solar cells. *J. Phys. Chem. Lett.* **6**, 3190–3194. <http://dx.doi.org/10.1021/acs.jpclett.5b01381> (2015).
129. Game, O. S., Buchsbaum, G. J., Zhou, Y., Padture, N. P. & Kingon, A. I. Ions Matter: Description of the Anomalous Electronic Behavior in Methylammonium Lead Halide Perovskite Devices. *Adv. Funct. Mater.* **27**. <http://doi.wiley.com/10.1002/adfm.201606584> (16 2017).

130. Shao, Y. *et al.* Grain boundary dominated ion migration in polycrystalline organic–inorganic halide perovskite films. *Energy Environ. Sci.* **9**, 1752–1759. <http://xlink.rsc.org/?DOI=C6EE00413J> (2016).
131. Critical Role of Grain Boundaries for Ion Migration in Formamidinium and Methylammonium Lead Halide Perovskite Solar Cells. *Adv. Energy Mater.* **6** (13 2016).
132. Chandra, S. & C. Agrawal, R. Surface Diffusion Coefficient of Iodine in Some Superionic Solid Films. *J. Phys. Soc. Japan* **48**, 2171–2172. <http://journals.jps.jp/doi/10.1143/JPSJ.48.2171> (1980).
133. Van Reenen, S., Kemerink, M. & Snaith, H. J. Modeling Anomalous Hysteresis in Perovskite Solar Cells. *J. Phys. Chem. Lett.* **6**, 3808–3814. <http://dx.doi.org/10.1021/acs.jpclett.5b01645> (2015).
134. Article, E. *et al.* Reversible photo-induced trap formation in mixed-halide hybrid perovskites for photovoltaics. en. *Chem. Sci.* **6**, 613–617. <http://dx.doi.org/10.1039/C4SC03141E> (2015).
135. Steirer, K. X. *et al.* Defect Tolerance in Methylammonium Lead Triiodide Perovskite. *ACS Energy Letters* **1**, 360–366 (2016).
136. Azarhoosh, P., McKechnie, S., Frost, J. M., Walsh, A. & van Schilfgaarde, M. Relativistic origin of slow electron-hole recombination in hybrid halide perovskite solar cells. *APL Mater.* **4**, 091501. <https://doi.org/10.1063/1.4955028> (2016).
137. Zheng, F., Tan, L. Z., Liu, S. & Rappe, A. M. Rashba spin-orbit coupling enhanced carrier lifetime in $\text{CH}_3\text{NH}_3\text{PbI}_3$. *Nano Lett.* **15**, 7794–7800. <http://pubs.acs.org/doi/10.1021/acs.nanolett.5b01854> (2015).
138. Frost, J. M. *et al.* Atomistic origins of high-performance in hybrid halide perovskite solar cells. *Nano Lett.* **14**, 2584–2590. <http://www.ncbi.nlm.nih.gov/pmc/articles/PMC4022647/> (2014).
139. Sherkar, T. & Koster, J. A. Can ferroelectric polarization explain the high-performance of hybrid-halide perovskite solar cells? en. *Phys. Chem. Chem. Phys.* **18**, 331–338. <http://pubs.rsc.org/en/content/articlehtml/2015/cp/c5cp07117h> (2016).
140. Brandt, R. E., Stevanović, V., Ginley, D. S. & Buonassisi, T. Identifying defect-tolerant semiconductors with high minority carrier lifetimes: Beyond hybrid lead halide perovskites. *MRS Commun.* **2**, 265–275. <http://arxiv.org/abs/1504.02144> (2015).
141. Shockley, W. & Read, W. T. Statistics of the Recombinations of Holes and Electrons. *Phys. Rev.* **87**, 835–842. <http://link.aps.org/doi/10.1103/PhysRev.87.835> (5 1952).
142. Yu, P. & Cardona, M. *Fundamentals of Semiconductors* (Springer, London, 1996).
143. Stoneham, A. M. *Theory of Defects in Solids* (OUP Oxford, Oxford, 1975).
144. Brivio, F., Butler, K. T., Walsh, A. & Van Schilfgaarde, M. Relativistic quasiparticle self-consistent electronic structure of hybrid halide perovskite photovoltaic absorbers. *Phys. Rev. B* **89**, 1–6 (2014).
145. Hava, S. & Auslender, M. in *Springer Handbook of Electronic and Photonic Materials* 441–480 (Springer US, 2007).
146. Wang, K. A., Lian, C., Su, N., Jena, D. & Timler, J. Conduction band offset at the InN/GaN heterojunction. *Appl. Phys. Lett.* **91**, 232117–3. <http://link.aip.org/link/?APL/91/232117/1> (2007).
147. Chen, J. *et al.* Origin of the high performance of perovskite solar cells with large grains. *App. Phys. Lett.* **108**, 053302 (2016).

148. Yin, W. J., Chen, H., Shi, T., Wei, S. H. & Yan, Y. Origin of High Electronic Quality in Structurally Disordered $\text{CH}_3\text{NH}_3\text{PbI}_3$ and the Passivation Effect of Cl and O at Grain Boundaries. *Adv. Electron. Mater.* **1**, 1500044.
<http://doi.wiley.com/10.1002/aelm.201500044> (2015).
149. De Quilettes, D. W. *et al.* Impact of microstructure on local carrier lifetime in perovskite solar cells. *Science* **348**, 683–686.
<http://www.sciencemag.org/cgi/doi/10.1126/science.aaa5333> (2015).
150. Bischak, C. G., Sanehira, E. M., Precht, J. T., Luther, J. M. & Ginsberg, N. S. Heterogeneous Charge Carrier Dynamics in Organic-Inorganic Hybrid Materials: Nanoscale Lateral and Depth-Dependent Variation of Recombination Rates in Methylammonium Lead Halide Perovskite Thin Films. *Nano Lett.* **15**, 4799.
<http://dx.doi.org/10.1021/acs.nanolett.5b01917> (2015).
151. Long, R., Liu, J. & Prezhdo, O. V. Unravelling the Effects of Grain Boundary and Chemical Doping on Electron-Hole Recombination in $\text{CH}_3\text{NH}_3\text{PbI}_3$ Perovskite by Time-Domain Atomistic Simulation. *J. Am. Chem. Soc.* **138**, 3884.
<http://dx.doi.org/10.1021/jacs.6b00645> (2016).
152. Almora, O., Aranda, C., Zarazúa, I., Guerrero, A. & Garcia-belmonte, G. Non-capacitive Hysteresis in Perovskite Solar Cells at Room Temperature Non-capacitive Hysteresis in Perovskite Solar Cells at Room Temperature. *ACS Energy Lett.* **1**, 209–215.
<http://pubs.acs.org/doi/abs/10.1021/acsenergylett.6b00116> (2016).
153. Tai, Q. *et al.* Efficient and stable perovskite solar cells prepared in ambient air irrespective of the humidity. en. *Nat. Commun.* **7**, 11105.
<http://www.nature.com/ncomms/2016/160401/ncomms11105/full/ncomms11105.html> (2016).
154. Butler, K. T., Frost, J. M., Skelton, J. M., Svane, K. L. & Walsh, A. Computational materials design of crystalline solids. *Chem. Soc. Rev.* **45**, 6138–6146.
<http://xlink.rsc.org/?DOI=C5CS00841G> (2016).
155. Murray, A. *et al.* Modular design of SPIRO-OMeTAD analogues as hole transport materials in solar cells. en. *Chem. Commun.* **51**, 8935–8938.
<http://pubs.rsc.org/en/content/articlehtml/2015/cc/c5cc02129d> (2015).
156. Tsai, H. *et al.* High-efficiency two-dimensional Ruddlesden–Popper perovskite solar cells. *Nature* **536**, 312–316. <http://www.nature.com/doifinder/10.1038/nature18306> (2016).
157. $(\text{CH}_3\text{NH}_3)_2\text{Pb}(\text{SCN})_2\text{I}_2$: A New More Stable Structural Motif for Hybrid Halide Photovoltaics? EN. *J. Phys. Chem. Lett.* **6**, 4594–4598.
<http://pubs.acs.org/doi/10.1021/acs.jpclett.5b02177> (2015).
158. McClure, E. T., Ball, M. R., Windl, W. & Woodward, P. M. $\text{Cs}_2\text{AgBiX}_6$ (X=Br,Cl) — New visible light absorbing, lead-free halide perovskite semiconductors. *Chem. Mater.* **6**, 2–4.
<http://dx.doi.org/10.1021/acs.chemmater.5b04231> (2016).
159. Wei, F. *et al.* The synthesis, structure and electronic properties of a lead-free hybrid inorganic–organic double perovskite $\text{MA}_2\text{KBiCl}_6$ (MA = methylammonium). *Mater. Horiz.* **3**, 328–332. <http://xlink.rsc.org/?DOI=C6MH00053C> (2016).
160. Hohenberg, P. & Kohn, W. Inhomogeneous Electron Gas. *Phys. Rev.* **136**, B864.
<http://link.aps.org/abstract/PR/v136/pB864>
http://prola.aps.org/abstract/PR/v136/i3B/pB864{_\}1
http://prola.aps.org/pdf/PR/v136/i3B/pB864{_\}1 (1964).

161. Kohn, W. & Sham, L. J. Self-Consistent Equations Including Exchange and Correlation Effects. *Phys. Rev.* **140**, A1133. <http://link.aps.org/abstract/PR/v140/pA1133> http://prola.aps.org/abstract/PR/v140/i4A/pA1133{_}1 http://prola.aps.org/pdf/PR/v140/i4A/pA1133{_}1 (1965).
162. Burke, K. & friends. *The ABC of DFT* <https://dft.uci.edu/doc/g1.pdf6> (June 27, 2019).
163. Scuseria, G. E. & Staroverov, V. N. *Progress in the development of exchange-correlation functionals* in *In Theory and Application of Computational Chemistry: The First 40 Years* (2005), 669.
164. Perdew, J. P. & Ruzsinszky, A. Fourteen easy lessons in density functional theory. *InterNatl. J. (Wash.) of Quantum Chemistry* **110**, 2801–2807. <https://onlinelibrary.wiley.com/doi/abs/10.1002/qua.22829>.
165. Kohn, W. Nobel Lecture: Electronic structure of matter—wave functions and density functionals. *Rev. Mod. Phys.* **71**, 1253–1266. <https://link.aps.org/doi/10.1103/RevModPhys.71.1253> (5 1999).
166. Lejaeghere, K. *et al.* Reproducibility in density functional theory calculations of solids. *Science* **351** (2016).
167. Durrant, T. R., Murphy, S. T., Watkins, M. B. & Shluger, A. L. Relation between image charge and potential alignment corrections for charged defects in periodic boundary conditions. *J. Chem. Phys.* **149**, 024103 (2018).
168. Vinichenko, D., Senoy, M. G., Friend, C. M. & Kaxiras, E. Accurate formation energies of charged defects in solids: A systematic approach. *Phys. Rev. B* **95**, 235310. <https://link.aps.org/doi/10.1103/PhysRevB.95.235310> (23 2017).
169. Leslie, M & Gillan, N. J. The energy and elastic dipole tensor of defects in ionic crystals calculated by the supercell method. *J. Phys. C: Solid State Phys.* **18**, 973–982. <https://doi.org/10.1088%2F0022-3719%2F18%2F5%2F005> (1985).
170. Lany, S. & Zunger, A. Accurate prediction of defect properties in density functional supercell calculations. *Modell. Simul. Mater. Eng.* **17**, 084002. <https://doi.org/10.1088%2F0965-0393%2F17%2F8%2F084002> (2009).
171. Freysoldt, C., Neugebauer, J. & Van de Walle, C. G. Fully Ab Initio Finite-Size Corrections for Charged-Defect Supercell Calculations. *Phys. Rev. Lett.* **102**, 016402. <https://link.aps.org/doi/10.1103/PhysRevLett.102.016402> (1 2009).
172. Kumagai, Y. & Oba, F. Electrostatics-based finite-size corrections for first-principles point defect calculations. *Phys. Rev. B* **89**, 195205. <https://link.aps.org/doi/10.1103/PhysRevB.89.195205> (19 2014).
173. Freysoldt, C. & Neugebauer, J. First-principles calculations for charged defects at surfaces, interfaces, and two-dimensional materials in the presence of electric fields. *Phys. Rev. B* **97**, 205425. <https://link.aps.org/doi/10.1103/PhysRevB.97.205425> (20 2018).
174. Komsa, H.-P. & Pasquarello, A. Finite-Size Supercell Correction for Charged Defects at Surfaces and Interfaces. *Phys. Rev. Lett.* **110**, 095505. <https://link.aps.org/doi/10.1103/PhysRevLett.110.095505> (9 2013).
175. Kim, S., Chang, K. J. & Park, J.-S. Finite-size supercell correction scheme for charged defects in one-dimensional systems. *Phys. Rev. B* **90**, 085435. <https://link.aps.org/doi/10.1103/PhysRevB.90.085435> (8 2014).
176. Ashcroft, N. W. & Mermin, N. D. *Solid State Physics* (Saunders College, 1976).
177. Ariel, V. & Natan, A. *Effective mass and the Energy-Mass relationship* <https://arxiv.org/abs/1205.3995> (Apr. 1, 2019).

178. E. O. Kane. Band structure of indium antimonide. *J. Phys. Chem. Solids* **1**, 249–261. [https://doi.org/10.1016/0022-3697\(57\)90013-6](https://doi.org/10.1016/0022-3697(57)90013-6) (1957).
179. L. D. Whalley. effmass: An effective mass calculator. <https://doi.org/10.5281/zenodo.1285137> (2018).
180. B. Morgan. vasppy: A Python suite for manipulating VASP input and output. <https://doi.org/10.5281/zenodo.1263753> (2018).
181. Ganose, A. M., Jackson, A. J. & Scanlon, D. O. sumo: Command-line tools for plotting and analysis of periodic ab initio calculations. *The Journal of Open Source Software* **3**.
182. Fornari, A. & Sutton, C. Effective Mass Calculator. <https://github.com/afonari/emc> (2012).
183. Ong, S. P. *et al.* Python Materials Genomics (pymatgen): A robust, open-source python library for materials analysis. *Computational Mater. Sci.* **68**, 314–319. <https://doi.org/10.1016/j.commatsci.2012.10.028> (2013).
184. L. R. Ingersoll O.J. Zobel, A. I. *Heat conduction with engineering, geological and other applications* (Thames and Hudson, 1948).